Dissertation

submitted to the
Combined Faculties of the Natural Sciences and Mathematics
of the Ruperto-Carola-University of Heidelberg, Germany
for the degree of
Doctor of Natural Sciences

Put forward by
Yonghao Mi
born in Tai'an, Shandong, China

Oral examination: June 28th**, 2017**

Strong-field ionization of atoms

and molecules with two-color laser pulses

Referees: **Prof. Dr. Thomas Pfeifer**
Prof. Dr. Andreas Wolf

Starkfeld-Ionisation von Atomen und Molekülen mit zweifarbigen Laserpulsen — In dieser Arbeit wird die laserinduzierte Ionisation von Atomen und einfachen Molekülen experimentell unter Verwendung eines Reaktionsmikroskops und geformten Laserpulsen untersucht. Das Reaktionsmikroskop erlaubt, verschiedene Ionisationskanäle mit der Ionen-Elektronen-Koinzidenz-Technik zu unterscheiden. Die geformten Laserfelder, die durch Überlagerung von zwei Laserpulsen mit unterschiedlichen Farben und einstellbarer relativer Phase realisiert werden, spielen eine Schlüsselrolle in der Steuerung des elektronischen Wellenpakets mit hoher zeitlicher Auflösung.

Mit diesen beiden Methoden wird eine phasenabhängige Starkfeld-Ionisation von Ar und N_2 untersucht. Elektronenspektren, die bei der Einfachionisation von Ar und N_2 entstehen, werden miteinander verglichen. Darüber hinaus wird die Ionisation von H_2-Molekülen, getrennt in zwei Ionisationskanäle, untersucht. Ein signifikanter Unterschied in der Ausbeute der Photoelektronen niedriger Energie zwischen gebundenem und dissoziativem Ionisationskanal wird beobachtet. Dies beweist, dass die bisher geläufige Annahme eines zweistufigen Prozesses, in der nach Born-Oppenheimer Elektronen und Kernbewegung voneinander getrennt ablaufen, nicht vollständig ist. Schließlich wird diese Beobachtung als Population und anschließender Zerfall autoionisierender Zustände durch weitere Untersuchungen mit den zweifarbigen Laserpulsen verstanden.

Strong-field ionization of atoms and molecules with two-color laser pulses — In this work the laser-induced ionization of atoms and simple molecules is experimentally investigated by using a Reaction Microscope and sculpted laser pulses. The Reaction Microscope allows to distinguish different ionization channels with the ion-electron coincidence technique. The sculpted laser pulses, which are realized by superposition of two laser pulses with different colors and adjustable relative phase, play a key role in controlling the electronic wavepacket with high temporal resolution.

With these two methods, phase-controllable strong-field ionization of Ar and N_2 is studied and electrons emitted from single ionization of Ar and N_2 are compared. Moreover, channel-selective electron emission is investigated for the fundamental molecular case of H_2. A significant difference in the low-energy photoelectron yield between bound and dissociative ionization channel is observed, proving the Born-Oppenheimer-based two-step process is not complete. Finally, this observation is understood as the population and subsequent decay of autoionizing states by further investigations with the two-color laser pulses.

List of Publications

Within the framework of this thesis, the following articles have been published or prepared in refereed journals:

Yonghao Mi, Andreas Kaldun, Kristina Meyer and Thomas Pfeifer.
Time-domain pulse compression by interfering time-delay operations.
Phys. Rev. A **88**, 053824 (2013).

Yonghao Mi, Nicolas Camus, Martin Laux, Lutz Fechner, Robert Moshammer and Thomas Pfeifer.
Ionization of atoms and molecules in a strong two-color field.
J. Phys. Conf. Ser. **635**, 092093 (2015).

Yonghao Mi, Nicolas Camus, Lutz Fechner, Martin Laux, Robert Moshammer and Thomas Pfeifer.
Electron-nuclear coupling through autoionizing states after strong-field excitation of H_2 *molecules.*
Phys. Rev. Lett. **118**, 183201 (2017).

Further publications with own contributions:

Zuoye Liu, Stefano M. Cavaletto, Christian Ott, Kristina Meyer, Yonghao Mi, Zoltán Harman, Christoph H. Keitel, and Thomas Pfeifer.
Phase reconstruction of strong-field excited systems by transient-absorption spectroscopy.
Phys. Rev. Lett. **115**, 033003 (2015).

Nicolas Camus, Enderalp Yakaboylu, Lutz Fechner, Michael Klaiber, Martin Laux, Yonghao Mi, Karen Hatsagortsyan, Thomas Pfeifer, Christoph Keitel, Robert Moshammer
Experimental evidence for Wigner's tunneling time.
submitted (2017).

Contents

Chapter 1

Introduction

In 1900 the famous physicist Lord Kelvin gave a speech entitled "Nineteenth-Century Clouds over the Dynamical Theory of Heat and Light" starting with "The beauty and clearness of the dynamical theory, which asserts heat and light to be modes of motion, is at present obscured by two clouds." The two "clouds" refer to the unsatisfactory explanations that physicists of that time could give to the Michelson-Morley experiment and the black-body radiation. As we know, the two "clouds" disappeared with the birth of the theory of relativity and quantum mechanics, which build up modern physics. The theory of relativity deals with large velocities comparable to the speed of light while quantum mechanics applies to systems on small scales, close to and less than the atomic size. The past century has witnessed not only the rapid development of the theories themselves but also numerous outstanding products as a result of modern physics and their corresponding technologies that benefit our daily life. The two "clouds" in turn changed the world.

Laser (an acronym for Light Amplification by Stimulated Emission of Radiation) is such a widely-used product building upon a quantum mechanical effect called stimulated emission, which was first discovered theoretically by Einstein in 1917 [Ein17]. According to the theory, light can be described not only as electromagnetic waves but also as particles (photons). When an incident photon interacts with an excited atom or a molecule, besides the absorption and spontaneous emission of photons, a new photon with the identical wavelength, phase and polarization state as the incident photon is emitted. The stimulated emission process gives rise spatial and temporal coherence properties of laser light. The first laser was realized by Maiman [Mai60] in 1960 based on the theory by Schawlow and Townes [ST58], in which they extended the maser (Microwave Amplification by Stimulated Emission of Radiation) techniques to the optical and infrared region.

Nowadays, lasers have become essential tools not only in scientific research but also in industry, medicine, electronics and various other fields. Among the large number of applications, two types of lasers can be classified: the continuous-wave (cw) laser and the pulsed laser. For instance, the cw laser can be used for laser cooling [CHB+85] and trapping atoms [CBAC86], as well as for high-resolution spectroscopic measurements thanks to its narrow bandwidth. It is worth pointing out that the recent observation of gravitational waves [AAA+16] is realized by using a laser interferometer in which high-power lasers at the wavelength of 1064 nm are applied with extremely stable frequency and

power. For the pulsed laser, the broadening of its spectrum leads to a decrease of pulse duration. With the development of the Q-switching and the Kerr lens mode-locking techniques [Rul05], the time scale of the laser pulse duration has decreased from nanoseconds (ns, 10^{-9} s) to femtoseconds (fs, 10^{-15} s), which is comparable to the time scale of intramolecular motion and bond breaking in a chemical reaction. In analogy to a camera, the femtosecond laser pulses thus allow for resolving the dynamics of molecular bonds and opened a new field known as femtochemistry [Zew88, Zew00]. In 1999, Ahmed Zewail was awarded the Nobel Prize in Chemistry for his pioneering studies of chemical reactions using femtosecond lasers.

In order to achieve better temporal resolution, shorter pulses are required. For the commercial Ti:Sapphire laser at the central wavelength of 800 nm, the pulse duration (full-width at half maximum) can be as short as 4 to 5 fs. To probe the electronic dynamics proceeding on the time scale of attoseconds (as, 10^{-18} s), we have to use the knowledge of attosecond physics [KI09]. One strategy is to generate pulses down to the time scale of attoseconds, which can be realized by using a light conversion mechanism called high-harmonic generation (HHG). In this process, coherent attosecond pulse trains in the range of soft x-ray are emitted. With an attosecond pump-probe experiment (also known as attosecond transient absorption spectroscopy), real-time observation of valence electron dynamics [GLW+10] and reconstruction of the electron wave packet [OKA+14] have become possible.

One goal of measuring and understanding ultrafast dynamics in atoms and molecules is to coherently control chemical reactions with ultrashort laser pulses. Note that coherent control (also called quantum control) differs from macroscopic, thermodynamic control in which the varying temperature or pressure changes the chemical equilibrium of reactions. By using coherent laser pulses the evolution of electronic and internuclear wave packets can be steered [FKP+10], leading to selective reactions. Theoretical work on the quantum control of molecular reactions was first put forward by Brumer and Shapiro in 1986 [BS86] and was demonstrated by follow-up experiments [CYE90, Zar98]. In these experiments, interferences between different pathways were observed. By changing more than one parameter (e.g. phase, amplitude or polarization) of the laser fields, the probability of possible reaction pathways can be controlled. It has been demonstrated that the shape of laser pulses plays an important role in determining chemical reactions [BKP+04]. More than a decade ago, the carrier-envelope-phase (CEP) stabilized laser was realized [PGW+01], giving rise to the laser pulse containing only a few optical cycles. For the few-cycle CEP-stabilized laser, the absolute phase (offset between the maximum of the electric field and the maximum of the pulse envelope) significantly changes the pulse shape. In 2006 Kling *et al.* reported that the localization of electrons can be achieved in the dissociation process of D_2 molecules by using such few-cycle laser pulses [KSV+06], which for the first time proved that direct control of a chemical reaction can be realized by steering the electronic motion. Since then CEP-stabilized laser pulses have been widely used for controlling the asymmetric emission of ions or electrons in ultrafast processes (ionization or dissociation) involving simple molecules [MFH+07, KFF+09, SKPT+10, FSC+13] and for controlling the fragmentation reactions of a series of polyatomic molecules [XDDR+12]. Besides CEP control, two-color pulses, which are synthesized by spatially and temporally overlapping

a fundamental-frequency femtosecond laser pulse with its second-harmonic, have become another efficient tool for the control of the electronic wave packet [XRK$^+$12]. Changing the relative phase between the two-color laser pulses allows to shape the electric field of the pulses on attosecond time scales. In the framework of this thesis, we investigate the ultrafast dynamics of atoms and molecules by using such a phase-controllable two-color (400 nm + 800 nm) laser field.

What will happen if an atom or a molecule is exposed to an ultrafast laser field? It is clear that the atom or the molecule will be ionized if the laser field is sufficiently strong. Two ionization mechanisms, multi-photon and tunnel ionization can be distinguished according to the theory by Keldysh published in 1965 [Kel65]. For multi-photon ionization, atoms and molecules can absorb integer number of photons and emit a free electron. Increasing wavelength and intensity of the laser field eventually leads to the tunnel ionization regime. As the duration of the laser pulses is in the time scale of femtoseconds, the peak intensity of the laser can be extremely high. For our Ti:Sapphire laser with the pulse energy of 1 mJ and the pulse duration of 25 fs, the intensity in a focal spot of a few microns in diameter is estimated to be 10^{14} W/cm^2 to 10^{15} W/cm^2. The electric field of the laser pulse is so strong that it can distort the Coulomb potential inside an atom or a molecule. The tunneling process occurs at the peaks of the laser field during the half cycle when the atomic or molecular potential barrier is lowered. To describe the motion of electrons in a strong laser field, Corkum in 1993 developed a semi-classical recollision model which is referred to as the three-step model [Cor93]. In this model, once the active electron is freed by tunnel ionization (the first step), this electron is considered as a classical particle accelerating in the laser field (the second step). When the electric field changes sign in the next half cycle, the electron can be pulled back to its parent core, leading to an elastic or inelastic scattering process (the third step). This model can explain a large number of strong-field phenomena such as the HHG process, non-sequential double ionization, recollision excitation etc.

Photons, electrons and ions are the most important particles in a reaction. As we know, photons can be detected by a spectrometer. The detection of electrons and ions can be realized by a time of flight (TOF) or velocity-map imaging (VMI) spectrometer which requires high voltage and high vacuum. A drawback for the two detection techniques is that only ions or electrons can be detected in one measurement. As a result, numerous studies concentrated on measurements of the ions emitted after a strong-field ionization process [Pos04] in order to investigate the wave packet dynamics for different ionization channels. However, the ion information alone is often not sufficient to determine the entire reaction pathway. One way to obtain the full kinematic information is to consider in addition the electron [dJFZ$^+$04]. The so-called ion-electron coincidence technique can be realized by the Reaction Microscope (REMI). In some cases REMI is also named cold target recoil-ion momentum spectroscopy (COLTRIMS) [UMD$^+$03]. It allows for the reconstruction of the momenta of electrons emitted from different ionization pathways in the ultrafast atomic and molecular processes.

By combining the ion-electron coincidence technique with the ultrafast two-color laser fields, we investigated the difference in asymmetric electron emission between atoms and molecules with similar ionization potentials (Ar and N_2), as well as signatures of different ionization pathways in a single molecule (H_2).

This thesis is structured as follows: In Chapter 2, the theories related to the main work of this thesis are introduced. Important theoretical models of strong-field ionization of atoms and H_2 molecule are explained. As the second-harmonic laser pulses are used in the subsequent measurements, the basics of nonlinear optics are presented as well. In Chapter 3, mathematical description, generation and characterization of ultrashort laser pulses are first discussed. Then a time-domain pulse compression method is put forward and demonstrated to be efficient by performing a simulation. In addition, the simulation on the phase-controllable two-color laser fields and the setup of a two-color interferometer are introduced. Chapter 4 deals with the hardware (setup) and the software (data analysis) of the Reaction Microscope which is used for the coincidence detection of electrons and ions. In Chapter 5, the experimental results on the single ionization of an Ar and N_2 gas mixture with two-color laser pulses are discussed. By changing the relative phase between the two colors, differences in the asymmetric electron emission between Ar and N_2 are observed. Furthermore, channel-selective electron emission from photo-ionization of H_2 molecule is investigated, results of which are present in Chapter 6. A clear difference in the low-energy photoelectron yield is observed between bound and dissociative ionization pathways. This difference is interpreted as the population of autoionizing states of H_2 in which vibrational energy is transferred to electronic energy. In Chapter 7, generation and detection of single-cycle terahertz (THz) pulses are discussed. An outlook towards a new two-color (IR-THz) experiment in the future is given. Finally, the results and conclusions are summarized in Chapter 8.

Chapter 2

Theoretical background

In this chapter some fundamental concepts of ionization of atoms and molecules and basic nonlinear optics are introduced as the theoretical background of this thesis. In the first section, mechanisms on laser-induced ionization of atoms are presented. Then we extend the ionization mechanism from atoms to the most fundamental H_2 molecules. Basic theoretical models on H_2 molecule in intense laser fields are introduced in the second section. Extensive knowledge on the strong-field ionization of atoms and molecules can be found in these standard textbooks [JKP12, LL77, Bra08, HS15]. In the last section of this chapter, a basic nonlinear process – second harmonic generation is discussed.

2.1 Strong-field ionization of atoms

2.1.1 Single-ionization mechanisms

Considering an atom exposed to an intense laser field, the most probable process is single ionization, in which an electron is ionized by the laser field and the atom ends up as a charged ion. Single ionization includes two ionization mechanisms, one is multi-photon ionization and the other is tunnel ionization. The two mechanisms can be distinguished by the Keldysh parameter γ [Kel65]:

$$\gamma = \sqrt{\frac{I_p}{2U_p}}, \tag{2.1}$$

where I_p is the ionization potential of the atom and U_p is called ponderomotive energy, representing the cycle-averaged kinetic energy of a quivering electron in a laser field [JKP12]. For a monochromatic laser field, it can be expressed as

$$U_p = \frac{e^2 E^2}{4m_e \omega^2}, \tag{2.2}$$

where e and m_e are the charge and the mass of the electron, E and ω are the electric field strength and the frequency of the laser, respectively. Note that the charge e and the mass
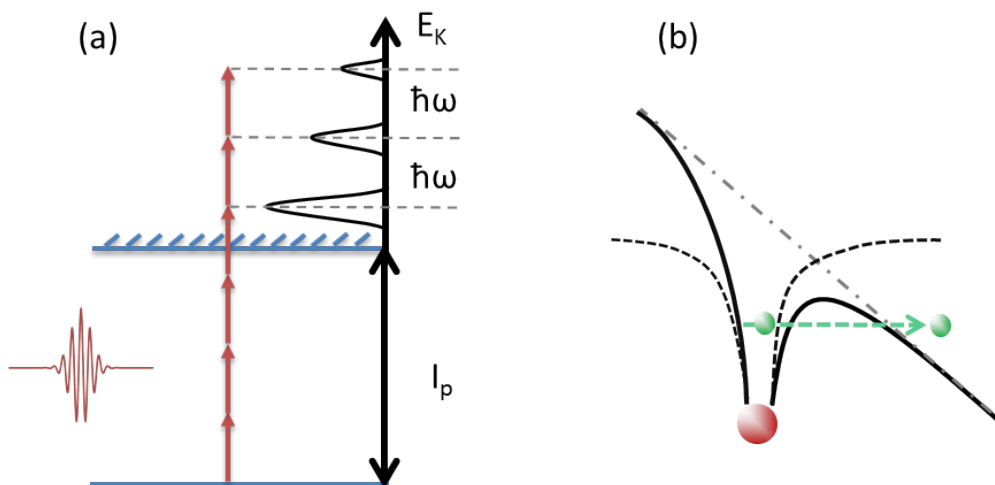
Figure 2.1: (a) Principle of multi-photon ionization: the electron is freed with the absorption of n photons with $n\hbar\omega \geq I_p$. For above-threshold ionization, the electron can also absorb additional photons than required for ionization. (b) Principle of tunnel ionization: the atomic potential is modified by the strong laser field and the electron can tunnel through the barrier.

of the electron m_e are unity in atomic units. Thus, the U_p in atomic units is given by

$$U_p = \frac{E^2}{4\omega^2}. \tag{2.3}$$

Inserting Equation 2.3 into Equation 2.1, the Keldysh parameter is given by

$$\gamma = \omega\sqrt{\frac{2I_p}{E^2}}. \tag{2.4}$$

If $\gamma \gg 1$, the dominant process is the electron being ionized by absorbing several photons, which is named multi-photon ionization. If $\gamma \ll 1$, the laser intensity is strong enough to bend the Coulomb potential of the atom such that an electron can tunnel out of the potential. This process is known as tunnel ionization. The principles of the two ionization mechanisms are shown in Fig. 2.1. When an atom is chosen, the ionization potential is fixed. The Keldysh parameter is only determined by the laser frequency ω and the intensity I. For instance, Fig. 2.2 presents the Keldysh parameter for argon (Ar) as a function of laser wavelength and intensity. We see that increasing of wavelength and intensity helps to decrease the Keldysh parameter, eventually leading to the deep tunnel-ionization regime. For the widely used Ti:Sapphire laser (see Section 3.1.3), the central wavelength is 800 nm and the intensity of the laser pulses is normally in the order of 10^{14} to 10^{15} W/cm^2. It means the Keldysh parameter for argon in such a laser field is close to 1, where both multi-photon and tunnel ionization can occur.

In fact, there is no sharp boundary between multi-photon ionization and tunnel ionization. For example, Rudenko et al. [RZS+04] observed the signature of multi-photon ionization in the tunneling region. The two ionization mechanisms will be discussed in the following sections.
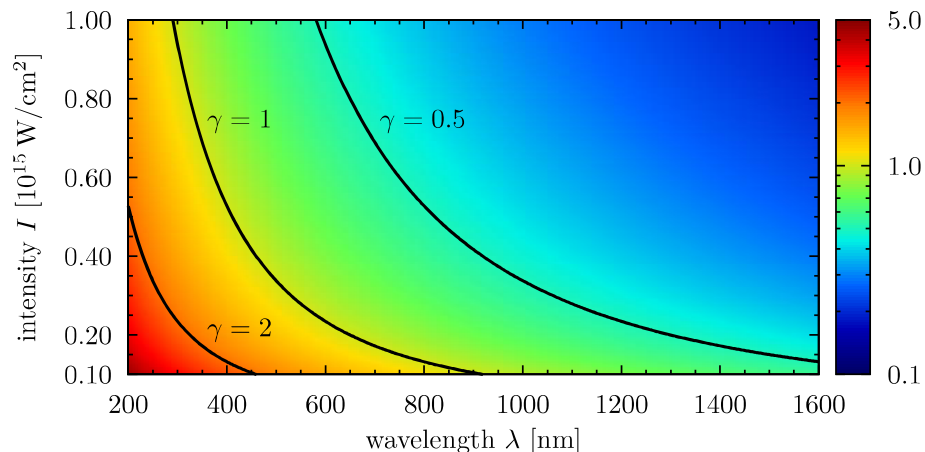
Figure 2.2: Keldysh parameter for Ar as a function of laser wavelength and intensity. Figure taken from [Fec14]

Multi-photon ionization

As shown in Fig. 2.1 (a), multi-photon ionization occurs with the absorption of n (integer number) photons such that the energy of the absorbed photons is larger or at least equal to the ionization potential ($n\hbar\omega \geq I_p$). This process was first observed by Damon and Tomlinson [DT63] in the ionization of gases (helium, argon and air mixture) by using a ruby laser. In the multi-photon ionization regime, the electric field of the laser is weak compared to the Coulomb potential of atoms. Thus, this mechanism can be well described by the lowest-order of perturbation theory (LOPT) [PKK97]. For the simplest case, the ionization rate of this process is given by [FPAC82]

$$\Gamma_n = \sigma_n I^n, \tag{2.5}$$

where σ_n is the generalized n-photon cross section and I is the intensity of the laser.

The freed electrons by absorption of n photons are still affected by the Coulomb potential and can absorb several additional photons, which is known as above-threshold ionization (ATI). As parts of our experimental results can be attributed to the ATI process, this phenomenon will be discussed in detail in Section 2.1.2.

Tunnel ionization

If the laser frequency is low and the intensity is strong enough ($\gamma \ll 1$) such that the electric field of the atom or molecule can be modified by the laser field and the electron can tunnel through the barrier [shown in Fig. 2.1 (b)], the ionization can be described by a quasi-static model in which the tunneling rate is given by [LL77]

$$W = \frac{4(2I_p)^{5/2}}{E}\exp\left(-\frac{2(2I_p)^{3/2}}{3E}\right), \tag{2.6}$$

where E is the static electric field strength. Due to the exponential factor in Equation 2.6, tunneling occurs primarily at the peaks of the laser field during the half cycle when the

potential barrier is lowered. In 1965 Keldysh developed the quasi-static theory [Kel65], in which the Keldysh parameter is defined to describe the multi-photon ionization in the low-frequency limit. In the theory by Keldysh, an electron after being ionized is assumed to interact only with the laser field and not with the Coulomb field of its parent core. This theory approach is known as strong field approximation (SFA) and has been widely used in modeling the electrons ionized in the strong laser field.

Based on the Keldysh theory, numerous theoretical work has been put forward to understand the tunnel ionization mechanism in the strong laser field (see e.g. [DK98,Pop04] for a review). Among these theories, the ADK theory [ADK86] is considered as the standard theory for describing the tunnel ionization. The ionization rate W_{ADK} for an electronic state with angular and magnetic quantum number l and m is given by

$$
\begin{aligned}
W_{ADK} = \sqrt{\frac{3En^{*3}}{\pi Z^3}} \frac{Z^2}{4\pi n^{*3}} \left(\frac{2e}{n^*}\right)^{2n^*} \frac{(2l+1)(l+|m|)!}{2^{|m|}(|m|)!(l-|m|)!} \\
\times \left(\frac{2Z^3}{En^{*3}}\right)^{2n^*-|m|-1} \exp\left(-\frac{2Z^3}{3En^{*3}}\right),
\end{aligned}
\tag{2.7}
$$

where the effective principle quantum number $n^* = Z/\sqrt{2I_p}$, Z is the charge of the atomic residue and E is the strength of the laser field.

When the laser intensity further increases, the potential barrier becomes lower and narrower. Finally, at a critical intensity I_c the barrier is completely suppressed such that the electron can classically flow over the top of the barrier, which is called over-the-barrier ionization (OBI). In other words, the maximum of the effective potential is lowered to a value equal to the I_p of the bound electron at the critical intensity. For atomic hydrogen, this critical intensity is 1.4×10^{14} W/cm^2.

2.1.2 Above-threshold ionization

With the energy spectra of photoelectron being measured, Agostini *et al.* [AFM$^+$79] discovered that the freed electron can absorb additional photons more than the minimum number required for multi-photon ionization at high laser intensities ($I > 10^{11}$ W/cm^2). The energy spectra exhibited several distinct peaks separated by the photon energy $\hbar\omega$. The energy of the ejected photoelectron is

$$
E_s = (n_0 + s)\hbar\omega - I_p,
\tag{2.8}
$$

where n_0 is the minimum number of photons required to reach the ionization potential of the atom and s is the number of excess photons absorbed by the atom. According to the LOPT prediction, the ionization rate of the above-threshold ionization (ATI) at low laser intensities is given by

$$
\Gamma_{n+s} = \sigma_n I^{n+s}.
\tag{2.9}
$$

However, at high intensities, the above relationship is not valid any more. As the laser intensity increases, the low-energy ATI peaks are observed being suppressed [PAM88]. This is due to the intensity-dependent shift of the atomic levels (AC-Stark shift) in the
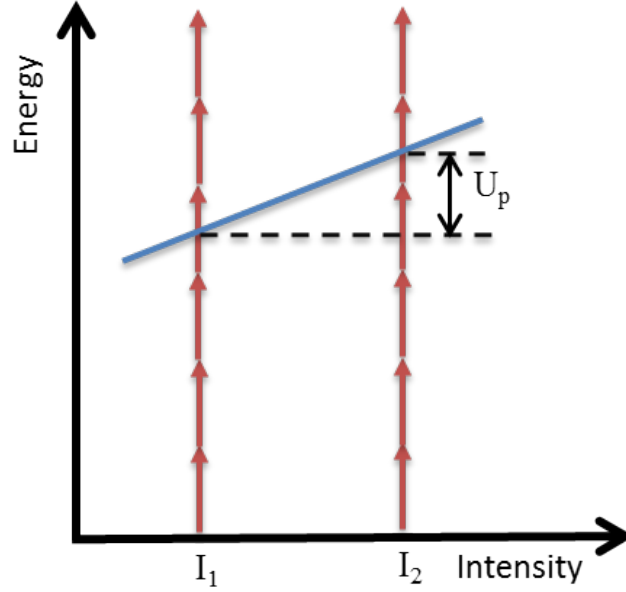
Figure 2.3: The intensity-dependent ionization potential of an atom. The equivalent potential is increased by U_p, which is linearly proportional to the laser intensity. At intensity I_1 the ionization by absorption of four photons is possible while it is forbidden at higher intensity I_2.

presence of the laser field: the AC Stark shifts of the lowest bound levels are small while the shifts of the Rydberg and continuum states are given by the ponderomotive energy of the electron U_p (see Equation 2.3). As the U_p is proportional to I/ω^2, this value can be even larger than a photon energy. For example, the Ti:Sapphire laser at the wavelength of 800 nm with the intensity of 2.6×10^{13} W/cm^2 gives rise to the U_p equal to its photon energy (1.55 eV). As shown in Fig. 2.3, the continuum states are shifted upwards by U_p compared to the ground states, which is equivalent to the increase in the intensity-dependent ionization potential:

$$I_p(I) = I_p + U_p. \tag{2.10}$$

At lower intensity I_1, the ionization is possible by absorption of four photons. However, when the laser intensity increases to I_2, the equivalent ionization potential is shifted upwards by U_p such that the ionization by absorbing four photons is energetically prohibited. At least five photons are required for the ionization.

Besides the laser intensity, the pulse duration also significantly affects the ATI spectrum. For long laser pulses (longer than a few picoseconds), the laser field is still present after the electron escapes from the focal volume. The electron quiver motion is converted into radial motion due to the spatial inhomogeneity of the laser intensity and it gains an energy of U_p from the laser field. This energy increase of the electron exactly compensates the energy loss due to the AC-Stark shift of the ionization potential. Therefore, the energy of the photoelectron is given by Equation 2.9. However, for a short laser pulse whose pulse duration is in the sub-picosecond region, the laser field vanishes before the electron escapes from the focal volume. The electron thus has no time to accelerate in the focal volume and the energy spectrum reflects the actual photoelectron energies at the time t,

which is given by

$$E_s = (n_0 + s)\hbar\omega - [I_p + U_p(t)].$$ (2.11)

In this case, some excited states can be shifted into resonance due to the intensity-dependent Stark shift. Thus, at higher intensities, the ionization from these excited states can be enhanced and the corresponding ATI spectra exhibit a substructure, as shown in Fig. 2.4. The fine substructure was first observed by Freeman *et al.* [FBM⁺87] by using sub-picosecond laser pulses and is known as Freeman resonance. As the energy shift U_p is proportional to the laser intensity I, Freeman resonances can also be used to identify the laser intensity according to the measured ATI photoelectron energy spectrum. In our experimental results which will be introduced in Chapter 5, the Freeman resonances are also reflected in the electron momentum spectrum.

2.1.3   The three-step model

In order to describe the full information of strong field ionization, we have to further consider the electron behavior after it tunnels out. For example, the ionized electron is driven in the laser field and has the possibility of returning to its parent ion. The widely-accepted semi-classical recollision model developed by Corkum [Cor93] and by Kulander *et al.* [KSK93] has gained great success in explaining a series of strong-field phenomena, e.g. a plateau in the ATI photoelectron energy spectra [PNX⁺94], double ionization and high-harmonic generation (HHG) etc. This semi-classical recollision model is also called the three-step model, in which the strong-field ionization is considered to occur by the following three steps, as shown in Fig. 2.5. In the first step, the active electron is freed by tunnel ionization. In the second step, this electron is mainly affected by the laser field, in which it is accelerated. The electron motion in the laser field can be approximated by using classical mechanics in this step. As the polarization of the laser field changes sign in the next half cycle (for a linearly polarized laser), the electron can be pulled back towards its parent ion. Of course, whether the electron comes back to the parent ion depends on the initial phase of the laser field when the electron is ionized. If the electron returns, a third step occurs in which the electron recollides with its parent ion, resulting in an elastic or inelastic (HHG, impact ionization or excitation) scattering process. Assuming that the laser field is linearly polarized and spatially homogeneous and the initial drift velocity of the electron at the t_0 is zero, the electron velocity in the laser polarization direction at a later time t in atomic unit is given by [JKP12]

$$v(t) = A(t) - A(t_0),$$ (2.12)

where $A(t)$ is the vector potential of the laser field $E(t)$ [$E(t) = -\partial A(t)/\partial t$]. The electric field of the laser is

$$E(t) = E_0\cos(\omega t).$$ (2.13)

As the electron trajectory after tunnel ionization is treated classically, the combination of Equation 2.12 and Equation 2.13 yields the velocity of the electron

$$v(t) = -\frac{E_0}{\omega}[\sin(\omega t) - \sin(\omega t_0)]$$ (2.14)
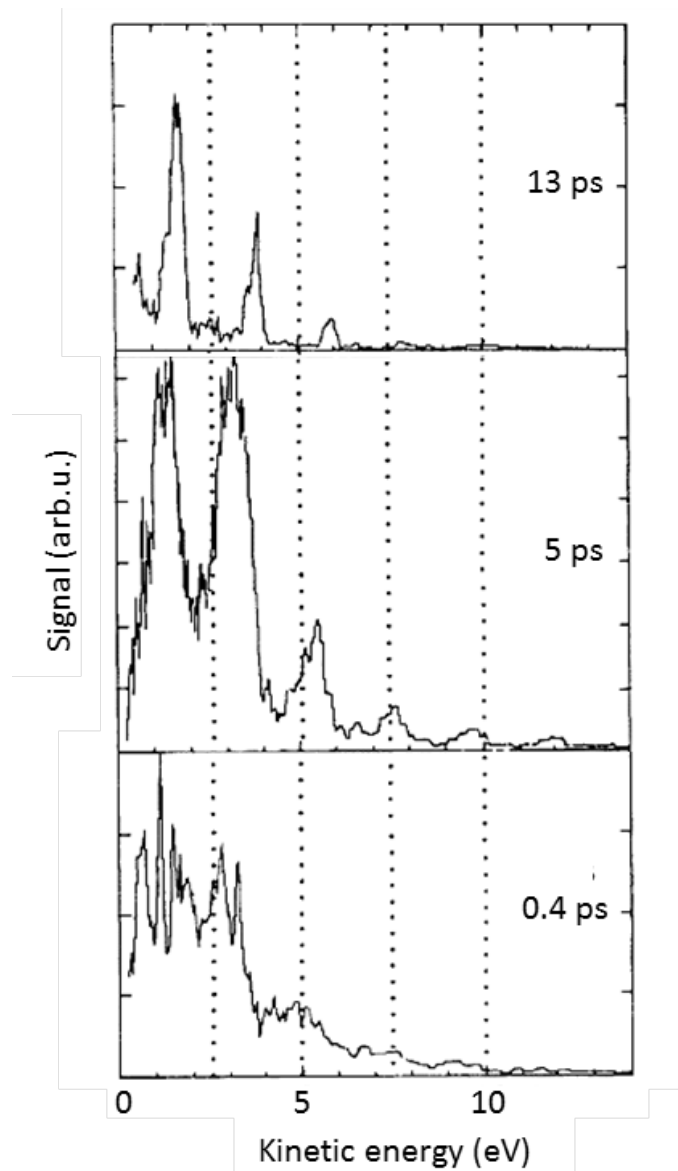
Figure 2.4:   Kinetic energy of photoelectrons emitted from xenon as a function of the laser pulse duration. The pulse energy is held roughly constant for all runs so the intensity increases from about 1.2×10^{13} W/cm^2 for 13 ps to about 3.9×10^{14} W/cm^2 for 0.4 ps. The individual ATI peaks break up into a narrow fine structure for the shortest pulse duration. Figure adapted from [FBM$^+$87].
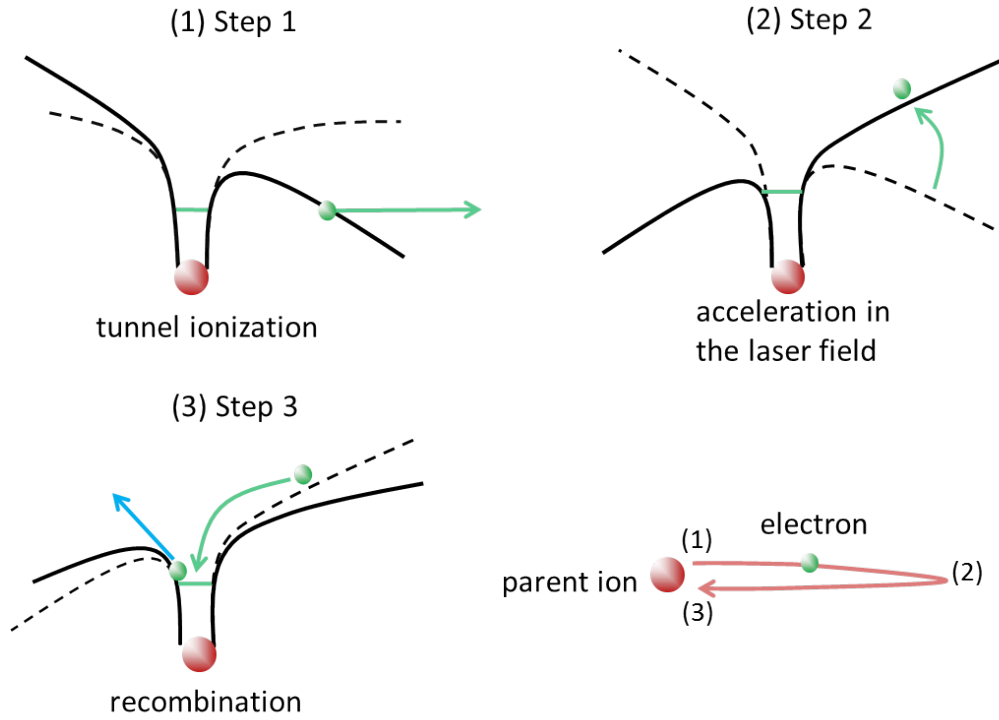
Figure 2.5: The principle of the three-step model. (1) The electron is freed by tunnel ionization. (2) The electron is driven in the laser field. As the polarization of the laser field changes sign, the electron can be accelerated back to its parent ion. (3) The returned electron recombines with the ion core resulting in an elastic or inelastic scattering process in which a second electron can be ionized or excited. The electrons after back-scattered from the ion and acceleration in the laser field can gain energy up to $10U_p$.

and the position of the electron in the laser field

$$x(t) = \frac{E_0}{\omega^2}[\cos(\omega t) - \cos(\omega t_0) + \omega(t - t_0)\sin(\omega t_0)]. \tag{2.15}$$

The electron energy E_{kin} is

$$E_{kin}(t,t_0) = \frac{1}{2}[A(t) - A(t_0)]^2 = 2U_p[\sin(\omega t) - \sin(\omega t_0)]^2. \tag{2.16}$$

By solving the Equation 2.15 numerically at $x(t) = 0$, we obtain the maximum of the Equation 2.16 to be approximately equal to $3.17U_p$ at the phase of the laser field $\omega t = 18°$. That means the maximum energy of the electrons returning to the parent ion is $3.17U_p$. As mentioned, high-harmonic photons are emitted when the electron recombines with the parent core. Thus, the expected cut-off harmonic energy is given by

$$\hbar\omega_c = 3.17U_p + I_p. \tag{2.17}$$

This prediction of the cut-off energy in the HHG spectrum agrees well with experimental results.

We now consider the condition in which the freed electrons are back scattered from the parent ion in the recollision process and further accelerated in the laser field. Paulus *et al.* [PBNW94] calculated the energies E_{kin} and angular distributions θ of the rescattered electrons as

$$E_{kin} = 2U_p \left[\cos^2 \omega t_0 + 2(1 - \cos\theta_0)\cos\omega t_1(\cos\omega t_1 - \cos\omega t_0) \right] \tag{2.18}$$

and

$$\cot\theta = \frac{p_x}{p_y} = \cot\theta_0 - \frac{\cos\omega t_1}{\cos\omega t_1 - \cos\omega t_0} \frac{1}{\sin\theta_0} \tag{2.19}$$

where t_0 is the initial time and t_1 is the first return time, θ_0 is the angle between the direction of the electron emission after rescattering with its parent ion and the direction of the laser polarization. According to these equations, the electrons after back-scattered from the ion and acceleration in the laser field can gain energy up to $10U_p$.

2.2 H$_2$ molecules in intense laser fields

In this section, we introduce some basic theoretical models on the most fundamental H$_2$ molecule in intense laser fields. Although atoms play a key role in determining the property of a molecule, the modeling on the molecule is much more challenging than simply adding the properties of atoms. In order to describe and to explain the molecules behavior in ultrafast laser fields, some approximations are required. In the following sections, important approximations and the corresponding theoretical models on the description of H$_2$ molecules will be summarized.

2.2.1 Born-Oppenheimer approximation

As the nuclei in a molecule have much larger mass compared to the electrons and they feel the same Coulomb force, the nuclei move much slower than electrons. That means the electrons can almost adjust their positions immediately to a new configuration when the nuclei move. In 1927, Born and Oppenheimer [BO27] proposed to consider the electronic and nuclear motion separately and neglect the interaction between the nuclei and electrons, which is known as Born-Oppenheimer (BO) approximation. This approximation is the basis of all molecular theories.

For diatomic molecules, the kinetic energy of the two nuclei and N electrons is

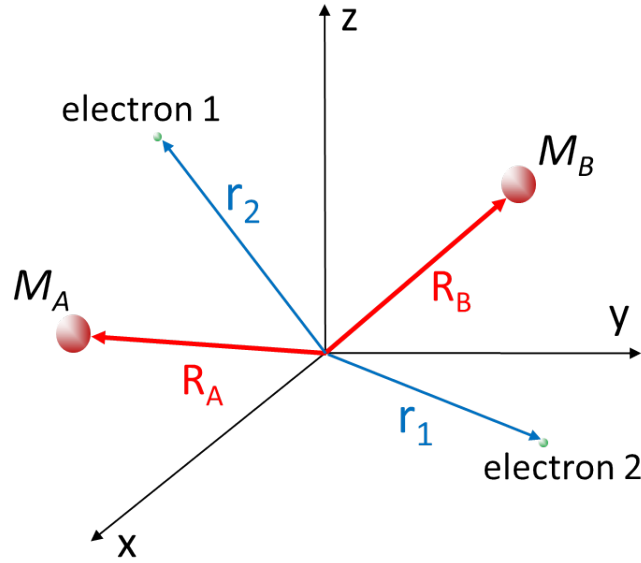$$\hat{T}_n = -\frac{\hbar^2}{2M}\nabla_R^2 \tag{2.20}$$

and

$$\hat{T}_e = \sum_{i=1}^{N}\left(-\frac{\hbar^2}{2m_e}\nabla_{r_i}^2\right), \tag{2.21}$$

where $\mathbf{r_i}$ represents the electron coordinates (shown in Fig. 2.6), $\mathbf{R} = \mathbf{R}_A - \mathbf{R}_B$ is the internuclear distance and M is the reduced mass of the two nuclei

$$M = \frac{M_A M_B}{M_A + M_B}. \tag{2.22}$$

Figure 2.6:   Schematic drawing of coordinates for a diatomic molecule. $\mathbf{R}_A$ and $\mathbf{R}_B$ refer to the nuclear coordinates and M_A and M_B denote the mass of the two nuclei. $\mathbf{r}_1$ and $\mathbf{r}_2$ are the coordinates for electrons.

The potential energy V including the sum of the Coulomb interactions between all particles is written as

$$V(\mathbf{R};\mathbf{r}_1,\mathbf{r}_2,...\mathbf{r}_N) = -\sum_{i=1}^{N} \frac{Z_A e^2}{(4\pi\varepsilon_0)|\mathbf{r}_i - \mathbf{R}_A|} - \sum_{i=1}^{N} \frac{Z_B e^2}{(4\pi\varepsilon_0)|\mathbf{r}_i - \mathbf{R}_B|}$$
$$+ \sum_{\substack{i,j=1\\i>j}}^{N} \frac{e^2}{(4\pi\varepsilon_0)|\mathbf{r}_i - \mathbf{r}_j|} + \frac{Z_A Z_B e^2}{(4\pi\varepsilon_0)R} \tag{2.23}$$

with the charges of the two nuclei $Z_A e$ and $Z_B e$. Thus, the time-independent Schrödinger equation for the system is

$$[\hat{T}_n + \hat{T}_e + V]\Psi(\mathbf{r}_1,\mathbf{r}_2,...\mathbf{r}_N;\mathbf{R}) = E\Psi(\mathbf{r}_1,\mathbf{r}_2,...\mathbf{r}_N;\mathbf{R}). \tag{2.24}$$

According to the BO approximation, $\Psi(\mathbf{r}_1,\mathbf{r}_2,...\mathbf{r}_N;\mathbf{R})$ can be written as a product composed by the wave function of electrons $\phi(\mathbf{r}_1,\mathbf{r}_2,...\mathbf{r}_N)$ and the wave function of nuclei $\psi(\mathbf{R})$:

$$\Psi(\mathbf{r}_1,\mathbf{r}_2,...\mathbf{r}_N;\mathbf{R}) = \phi(\mathbf{r}_1,\mathbf{r}_2,...\mathbf{r}_N)\psi(\mathbf{R}) \equiv \phi(\mathbf{r})\psi(\mathbf{R}) \tag{2.25}$$

with $\mathbf{r}$ and $\mathbf{R}$ the entirety of electronic and nuclear coordinates.

The Schrödinger equation for the electrons moving in the field of nuclei fixed at the positions $\mathbf{R}_A$ and $\mathbf{R}_B$ is

$$[\hat{T}_e + V(\mathbf{r};\mathbf{R})]\phi_\gamma(\mathbf{r};\mathbf{R}) = V_\gamma(\mathbf{R})\phi_\gamma(\mathbf{r};\mathbf{R}), \tag{2.26}$$

where $\phi_\gamma(\mathbf{r};\mathbf{R})$ is the so-called electronic wave function. The BO approximation considers $\mathbf{R}$ as a parameter and Equation 2.26 is solved for each fixed value of $\mathbf{R}$ independently,

which gives rise to a set of electronic quantum number γ. The eigenvalue $V_\gamma(\mathbf{R})$ for each set of γ is a continuous function of $\mathbf{R}$, known as molecular potential.

The BO approximation is valid for the electronic ground states of most molecules. However, for higher electronic states, the vibration of the nuclei can lead to a coupling between different electronic states, which means a breakdown of the BO approximation. In our experiments introduced in Chapter 6, we will discuss a vibrational autoionization mechanism which is a clear example of the breakdown of the BO approximation.

2.2.2 Franck-Condon principle

In the last section, we derived the molecular potential energy from the BO approximation. For single ionization of H$_2$ by laser pulses, the molecule is excited to the ground state ($1s\sigma_g$) of H$_2^+$. Assuming that the ionization occurs so fast that the internuclear distance R is not changed during this process, the transition between the potential energy curve of H$_2$ ground state and the $1s\sigma_g$ state of H$_2^+$ is vertical, as shown in Fig. 2.7. This vertical-transition approximation refers to Franck-Condon (FC) principle [Con26]. The corresponding transition region is called Franck-Condon (FC) Region. The center of the FC region refers to the position where the probability of the allowed transition is maximal.

The single ionization of H$_2$ can be considered as a projection of the initial wave function of H$_2$ Ψ_{H_2} via the dipole transition operator μ onto the wave function of H$_2^+$ $\Psi_{H_2^+}$. Here, the dipole transition operator μ is given by

$$\mu = \mu_e + \mu_N = -e\sum_i \mathbf{r}_i + e\sum_j Z_j \mathbf{R}_j. \tag{2.27}$$

As introduced in the previous section, the total wave function of H$_2$ and H$_2^+$ in the BO approximation can be written as a product of the wave functions of electronic and nuclear vibronic parts:

$$\Psi_{H_2} = \phi_{e,H_2}(\mathbf{r}_1, \mathbf{r}_2)\psi_{v,H_2}(\mathbf{R}) \tag{2.28}$$

$$\Psi_{H_2^+} = \phi_{e,H_2^+}(\mathbf{r}_1)\psi_{v,H_2^+}(\mathbf{R}). \tag{2.29}$$

The combination of the equations 2.27, 2.28 and 2.29 yields the transition amplitude

$$\left\langle \Psi_{H_2} \left| \mu \right| \Psi_{H_2^+} \right\rangle = \left\langle \phi_{e,H_2} \left| \mu_e \right| \phi_{e,H_2^+} \right\rangle \left\langle \psi_{v,H_2} \middle| \psi_{v,H_2^+} \right\rangle \\ + \left\langle \psi_{v,H_2} \left| \mu_N \right| \psi_{v,H_2^+} \right\rangle \left\langle \phi_{e,H_2} \middle| \phi_{e,H_2^+} \right\rangle. \tag{2.30}$$

Note that in Equation 2.30 the term $\left\langle \phi_{e,H_2} \middle| \phi_{e,H_2^+} \right\rangle = 0$ because these two electronic states are orthonormal. Therefore, the transition amplitude is then given by

$$\left\langle \Psi_{H_2} \left| \mu \right| \Psi_{H_2^+} \right\rangle = \left\langle \phi_{e,H_2} \left| \mu_e \right| \phi_{e,H_2^+} \right\rangle \left\langle \psi_{v,H_2} \middle| \psi_{v,H_2^+} \right\rangle. \tag{2.31}$$

In this equation, the term $\left\langle \phi_{e,H_2} \left| \mu_e \right| \phi_{e,H_2^+} \right\rangle$ denotes the intensity of the transition from the electronic state of H$_2$ to that of H$_2^+$, in which the transition is determined by the dipole
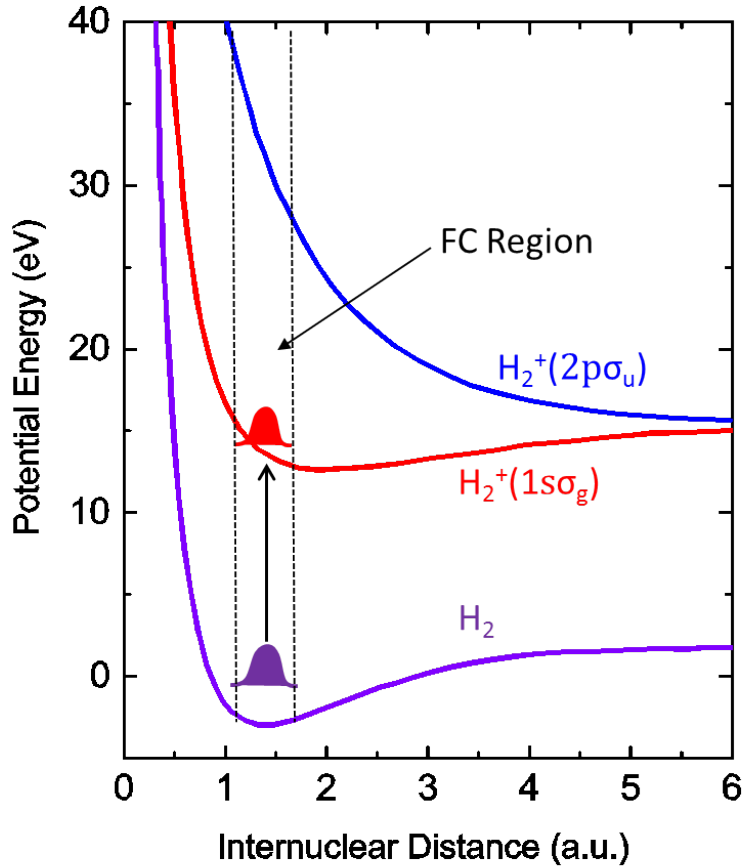
Figure 2.7: Schematic illustration of the Franck-Condon (FC) principle in the transition between the ground state of H_2 and the $1s\sigma_g$ state of H_2^+. The transition between the two potential energy curves is assumed to be vertical. The corresponding transition region is called Franck-Condon (FC) Region.

selection rules. The second term $\left\langle \psi_{v,H_2} | \psi_{v,H_2^+} \right\rangle$ is called Franck-Condon factor, which corresponds to the overlap between the two vibrational states of H_2 and H_2^+. The Franck-Condon factor determines the occupation of the vibrational states in H_2^+.

The BO approximation-based Franck-Condon principle agrees well with the experimental results in the occupation of the vibrational states of H_2^+ by e.g. electron collisions. However, some measurements with ultrashort laser pulses exhibited discrepancy in the vibrational distributions with the Franck-Condon principle [UFSC$^+$04]. This is due to the R-dependent ionization probability. R denotes the internuclear distance. For the potential energy curve of H_2^+, the equilibrium distance is larger than that for H_2 , the ionization potential is thus dependent on the internuclear distance. This leads to the population of the vibrational states of H_2^+ being different from the one derived from the Franck-Condon principle. For laser-induced strong field ionization of H_2 molecules, the ionization rate in the tunneling regime can be calculated by using the molecular ADK theory [TZL02].

2.2.3 Floquet theory

Numerous theoretical models have been developed to describe the molecules in intense laser fields (e.g. see [Ban95, PPT$^+$98, Pos04]). Among these theories, the Floquet theory [Shi65, Chu81] is considered as one of the most successful and intuitive approaches for the description of the molecule and the laser field. Within the Floquet picture, the laser-induced potential curves are calculated. These curves could explain a few new phenomena on the molecule dissociation in the laser field, e.g. bond-softening (BS), bond-hardening (BH) and above-threshold dissociation (ATD), which will be discussed in this section. The following summarized Floquet theory mainly refers to [Shi65, Chu81, Pav04, Fis10, Fec14].

The time-dependent Schrödinger equation for the H$_2$ molecular system in the laser field is given by

$$\hat{H}(\mathbf{r},R,t)\Psi(\mathbf{r},R,t) = i\hbar\frac{\partial}{\partial t}\Psi(\mathbf{r},R,t). \qquad (2.32)$$

Again, $\mathbf{r}$ and R represent the electronic coordinate and internuclear distance, respectively. The total Hamiltonian contains the time-independent (field-free) Hamiltonian $\hat{H}_0(\mathbf{r},R)$ and the interaction Hamiltonian $\hat{V}(\mathbf{r},t)$. According to the BO approximation, the field-free Hamiltonian can also be separated into a nuclear kinetic energy operator $\hat{T}_n$ and electronic Hamiltonian $\hat{H}_e$. Therefore, the total Hamiltonian can be written as

$$\hat{H}(\mathbf{r},R,t) = \hat{T}_n + \hat{H}_e(\mathbf{r},R) + \hat{V}(\mathbf{r},t). \qquad (2.33)$$

Assuming the laser has a linearly polarized, monochromatic and periodic electric field which is expressed as Equation 2.13, the Hamiltonian which represents the interaction with the laser field in the dipole approximation is

$$\hat{V}(\mathbf{r},t) = -e\mathbf{r}\cdot E(t) = -\frac{eE_0 z}{2}\left(e^{i\omega t}+e^{-i\omega t}\right) = V_- e^{i\omega t} + V_+ e^{-i\omega t}. \qquad (2.34)$$

Note that the time dependence of the total Hamiltonian (Equation 2.33) is only determined by the interaction Hamiltonian $\hat{V}(\mathbf{r},t)$. As $\hat{V}(\mathbf{r},t)$ is periodic in time with the period $T = 2\pi/\omega$, the total Hamiltonian is periodic:

$$\hat{H}(\mathbf{r},R,t) = \hat{H}(\mathbf{r},R,t+T). \qquad (2.35)$$

Therefore, the time-dependent Schrödinger equation becomes a first-order partial differential equation in the time variable with periodic coefficients. The general form of solutions of these equations are given by Floquet [Flo83]. According to the Floquet theory described in [Shi65, Chu81], the solution of the time-dependent Schrödinger equation can be expressed as

$$\Psi(\mathbf{r},R,t) = e^{iEt/\hbar}\Phi(\mathbf{r},R,t), \qquad (2.36)$$

where E is called quasi energy and $\Phi(\mathbf{r},R,t)$ is a periodic function with the period T. This periodic function can be expanded by a Fourier series. The wave function is then given by

$$\Psi(\mathbf{r},R,t) = e^{iEt/\hbar}\sum_{n=-\infty}^{\infty} e^{-in\omega t}\Phi_n(\mathbf{r},R) \qquad (2.37)$$

Inserting the above wave function into the Schrödinger equation 2.32 together with the Equation 2.33 and 2.34, the time-dependent Schrödinger equation is then transformed into a set of time-independent differential equations:

$$[E + n\hbar\omega - \hat{T}_n - \hat{H}_e(\mathbf{r}, R)]\Phi_n(\mathbf{r}, R) = V_+ \Phi_{n-1}(\mathbf{r}, R) + V_- \Phi_{n+1}(\mathbf{r}, R). \tag{2.38}$$

The wave functions $\Phi_n(\mathbf{r}, R)$ are the solutions of the field-free Hamiltonian $\hat{H}_0$ dressed with the phase $e^{-in\omega t}$, which is referred to as dressed states [Lau77]. For H_2^+, $\Phi_n(\mathbf{r}, R)$ refers to the wave functions $\Phi_g(\mathbf{r}, R)$ and $\Phi_u(\mathbf{r}, R)$ of the attractive and repulsive $1s\sigma_g$ and $2p\sigma_u$ states respectively. Their corresponding eigenvalue functions are expressed as follows:

$$\hat{H}_e(\mathbf{r}, R) \left|\Phi_{g,n}(\mathbf{r}, R)\right\rangle = V_g(R) \left|\Phi_{g,n}(\mathbf{r}, R)\right\rangle$$
$$\hat{H}_e(\mathbf{r}, R) \left|\Phi_{u,n}(\mathbf{r}, R)\right\rangle = V_u(R) \left|\Phi_{u,n}(\mathbf{r}, R)\right\rangle. \tag{2.39}$$

The eigenvalues $V_g(R)$ and $V_u(R)$ denote the potential energy curves of the $1s\sigma_g$ and $2p\sigma_u$ states. $\left|\Phi_{g,n}(\mathbf{r}, R)\right\rangle$ and $\left|\Phi_{u,n}(\mathbf{r}, R)\right\rangle$ refer to the states dressed with n photons. The operators V_+ and V_- in Equation 2.34 can be interpreted as absorption and emission of one photon. As only the states with different symmetries can be coupled due to the selection rules, $\Phi_n(\mathbf{r}, R)$ and $\Phi_{n\pm1}(\mathbf{r}, R)$ must correspond to different electronic ($1s\sigma_g$ and $2p\sigma_u$) states. Equation 2.38 is then changed to be

$$[E + n\hbar\omega - V_g(R)] \left|\Phi_{g,n}(\mathbf{r}, R)\right\rangle = V_+ \left|\Phi_{u,n-1}(\mathbf{r}, R)\right\rangle + V_- \left|\Phi_{u,n+1}(\mathbf{r}, R)\right\rangle$$
$$[E + (n+1)\hbar\omega - V_u(R)] \left|\Phi_{u,n+1}(\mathbf{r}, R)\right\rangle = V_+ \left|\Phi_{g,n}(\mathbf{r}, R)\right\rangle + V_- \left|\Phi_{g,n+2}(\mathbf{r}, R)\right\rangle. \tag{2.40}$$

Equation 2.40 represents an infinite set of differential equations and can be written as a matrix [Pav04] with infinite dimensions. The matrix of the Hamiltonian contains three diagonals. The elements along the center diagonal are $V_g(R)$ or $V_u(R)$ shifted by n, $n \pm 1$, ... photons, denoting diabatic potential curves. The elements along the other two diagonals which mean the coupling between neighboring states by the dipole transition are given by

$$V_{gu}(R) = V_{ug}(R) \equiv \left\langle 1s\sigma_g \left|V_\pm\right| 2p\sigma_u \right\rangle = \frac{\hbar\omega_R}{2}, \tag{2.41}$$

where ω_R is known as Rabi frequency. To calculate the matrix, we have to choose the number of the Floquet blocks. For example, the eigenvalues for a 2×2 matrix (for $n = 0$) are given by

$$E_\pm(R) = \frac{V_g(R) + V_u(R) - \hbar\omega}{2} \pm \frac{1}{2}\sqrt{[V_g(R) - V_u(R) + \hbar\omega]^2 + (\hbar\omega_R)^2}, \tag{2.42}$$

representing the adiabatic potential curves.

When there is no laser field, the coupling between neighboring states $V_{gu}(R)$ vanishes. Thus, the eigenvalues of the matrix, diabatic potential curves are acquired, corresponding to the potential curves of the $1s\sigma_g$ and $2p\sigma_u$ states shifted by n, $n \pm 1$, ... photons. As shown in Fig. 2.8 (b), crossing between diabatic states occur at an internuclear distance $R = X_1$, where the energy difference between V_g and V_u is equal to the photon energy. The crossing is called 1ω crossing. If the intensity of the laser field is not zero, the corresponding eigenvalues are called adiabatic potential curves (e.g. see Equation 2.42). In that case, a phenomenon called avoided crossing happens, which means there exists an energy gap between two adiabatic curves. The width of the gap is proportional to the square root of the laser intensity (Rabi frequency).
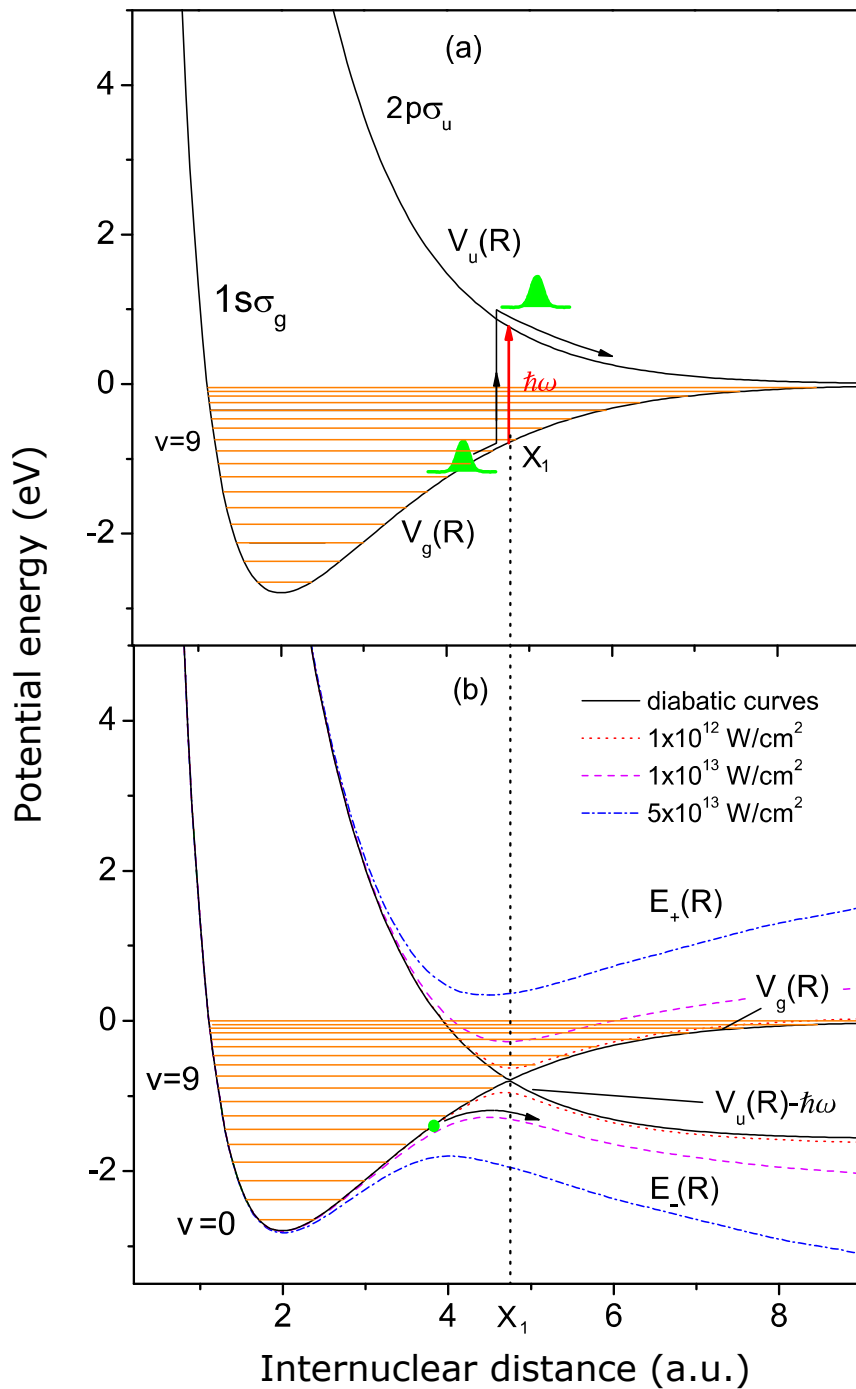
Figure 2.8: (a) Field-free potential curves for $1s\sigma_g$ and $2p\sigma_u$ states. At the internuclear distance $R = X_1$, the energy difference between the two states corresponds to a photon energy. (b) Field-dressed diabatic and adiabatic potential curves for different laser intensities calculated by using the Floquet theory. For diabatic curves, the crossing between $V_g(R)$ and $V_u(R) - \hbar\omega$ occurs at $R = X_1$. With the increase of the laser intensity, the avoided crossing opens at X_1 and the energy gap becomes larger and larger. Figure adapted from [Pav04].

Bond softening

According to the Floquet theory, the electrons and the field are considered as one system. Now we consider the dissociation process of a molecule. In the case of weak fields, the molecule can be excited to the repulsive state $V_u(R)$ by absorption of one photon, as shown in Fig. 2.8 (a). In the presence of intense laser fields, the adiabatic curves appear and the electron-field system moves along the lower adiabatic curve $E_-(R)$ from $R < X_1$ (attractive potential) to $R > X_1$ (repulsive potential). Thus, the molecular dissociation occurs, in which the field loses one photon (absorbed by the molecule). The potential barrier is lowered by the laser field such that the vibrational states lying below the 1ω crossing can already dissociate by "flying over the barrier" or by tunneling through the barrier, which is in analogy to the tunnel ionization picture in atoms (see Section 2.1). This process is known as bond softening (BS) [ZBMS90, BZMS90].

Bond hardening and above threshold dissociation

As the potential curve $E_+(R)$ has a minimum [shown in Fig. 2.8 (b)], the vibrational states lying above the 1ω crossing can be trapped in the laser-induced potential well. The molecule is then stabilized by the laser field. Dissociation via the transitions to the $1s\sigma$ state happens only when the intensity of the laser drops. This phenomenon is referred to as bond hardening or molecular stabilization [AS91, YC92, FPP$^+$99].

When the laser intensity is more than 10^{14} W/cm^2, a so-called 3ω avoided crossing appears due to the coupling between the $V_{g,n}$ and $V_{u,n-3}$ states. Passing the 3ω energy gap requires the absorption of three photons. The vibrational states below the 3ω crossing can dissociate along the lower curve of $V_{u,n-3}$. At a larger internuclear distance, the molecule encounters the crossing which is due to the coupling between $V_{u,n-3}$ and $V_{g,n-2}$ and emits a photon, ending up in the $V_{g,n-2}$ state. In total, the molecule dissociates by absorption of two photons. As there are more photons being absorbed in the dissociation of the molecule, this process is called above-threshold dissociation (ATD) [ZBMS90, GSHAM90]. The dissociation processes can be experimentally distinguished by the energy spectrum of the nuclei. The details will be introduced in Chapter 6.

2.3   Nonlinear optics: second-harmonic generation

As the experiments introduced in Chapter 5 and 6 deal with the two-color (800 nm + 400 nm) laser fields, we introduce the second-harmonic generation (SHG) process in nonlinear crystals in this section. This effect of nonlinear optics mainly refers to [Boy03, ST07, Mey14].

When the electric field of light is sufficiently weak, the interaction of light with matter can be described with a linear approximation. In other words, the light-induced polarization of the medium $\widetilde{P}(t)$ is proportional to the electric field $\widetilde{E}(t)$

$$\widetilde{P}(t) = \varepsilon_0 \chi \widetilde{E}(t) \tag{2.43}$$

with the permittivity of free space ε_0 and the linear susceptibility χ. However, when the electric field of the light reaches to a value which is comparable to the Coulomb field inside the atoms, this linear relation between $\widetilde{P}(t)$ and $\widetilde{E}(t)$ breaks down because the high order susceptibility contributes significantly. In this case, we need to use nonlinear optics to describe e.g. harmonic generation, difference-frequency mixing and so on. In nonlinear optics, the polarization is written as follows:

$$
\begin{aligned}
\widetilde{P}(t) &= \varepsilon_0 \left(\chi^{(1)} \widetilde{E}(t) + \chi^{(2)} \widetilde{E}(t)^2 + \chi^{(3)} \widetilde{E}(t)^3 + \ldots \right) \\
&\equiv \widetilde{P}^{(1)}(t) + \widetilde{P}^{(2)}(t) + \widetilde{P}^{(3)}(t) + \ldots
\end{aligned}
\tag{2.44}
$$

where $\chi^{(2)}$ and $\chi^{(3)}$ denote the second-order and the third-order nonlinear optical susceptibilities, respectively.

According to the Maxwell equations, the wave equation in nonlinear media (homogenous and isotropic) can be derived as

$$
\nabla^2 \widetilde{E} - \frac{n^2}{c^2} \frac{\partial^2 \widetilde{E}}{\partial t^2} = \frac{1}{\varepsilon_0 c^2} \frac{\partial^2 \widetilde{P}_{\mathrm{NL}}}{\partial t^2},
\tag{2.45}
$$

where n is the normal linear refractive index of the medium and c is the speed of light in vacuum. $\widetilde{P}_{\mathrm{NL}}$ is the polarization related to the nonlinear response of the driven electric field. $\partial^2 \widetilde{P}_{\mathrm{NL}}/\partial t^2$ represents the acceleration of the charges, corresponding to the emission of electromagnetic radiation.

As shown in Fig. 2.9 (a), the second-harmonic generation is a process in which a second-order nonlinear interaction occurs between a light field and a crystal with $\chi^{(2)} \neq 0$. As the electric field of a laser pulse is given by

$$
\widetilde{E}(t) = \frac{1}{2} \left(E_0 e^{i\omega t} + E_0^* e^{-i\omega t} \right),
\tag{2.46}
$$

the second-order polarization $\widetilde{P}_{\mathrm{nl}}^{(2)}(t)$ can be written as

$$
\widetilde{P}_{\mathrm{nl}}^{(2)}(t) \propto \chi^{(2)} \widetilde{E}(t)^2 = \frac{1}{2} \chi^{(2)} E_0 E_0^* + \frac{1}{4} \chi^{(2)} E_0^2 e^{i2\omega t} + \frac{1}{4} \chi^{(2)} E_0^{*2} e^{-i2\omega t}.
\tag{2.47}
$$

It can be seen that the polarization contains two contributions at zero frequency (the first term) and at the double frequency 2ω. Recalling the wave equation 2.45, the zero frequency term does not contribute to the emission of electromagnetic radiation as its second derivative of time vanishes. This contribution gives rise to a so-called optical rectification process, in which a static electric field is generated. The double frequency 2ω-component contribute the generation of electromagnetic radiation at the second harmonic frequency.

Now we consider the frequency spectrum of the second harmonic laser field. As will be introduced in Chapter 3, the representation of an electric field in the frequency domain can be obtained by Fourier transform from its time domain. The time-domain second harmonic electric field is given by the squared carrier field

$$
\widetilde{E}(t)^2 \propto \exp(i2\omega t),
\tag{2.48}
$$
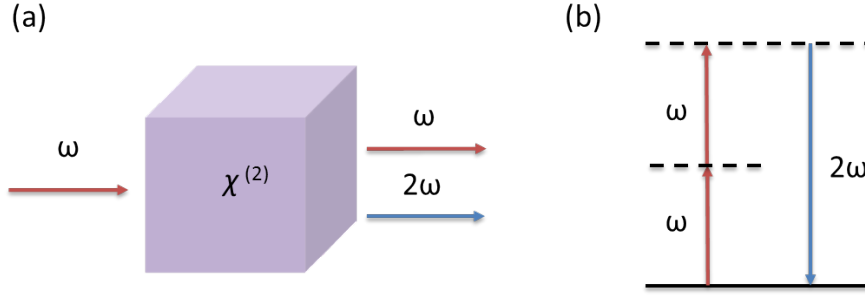
Figure 2.9: Schematic drawing of the second-harmonic generation process. (a) The second harmonic photons are generated by passing a photon of fundamental frequency through a nonlinear crystal with $\chi^{(2)} \neq 0$. (b) Two photons of the fundamental frequency ω are converted into a 2ω photon. Figure adapted from [Boy03].

the electric field in the frequency domain is

$$E_{\mathrm{s}}(2\omega) = \mathscr{F}\left\{\widetilde{E}(t)^2\right\} = \mathscr{F}\left\{\widetilde{E}(t) \cdot \widetilde{E}(t)\right\} \tag{2.49}$$

with the fundamental frequency ω. Note that the result of the Fourier transform

$$\mathscr{F}\left\{\widetilde{E}(t)\right\} = E_{\mathrm{s}}(\omega). \tag{2.50}$$

According to the convolution theorem

$$\mathscr{F}\left\{\widetilde{E}(t) \cdot \widetilde{E}(t)\right\} \propto \mathscr{F}\left\{\widetilde{E}(t)\right\} * \mathscr{F}\left\{\widetilde{E}(t)\right\}, \tag{2.51}$$

the electric field of the second harmonic in the frequency can be written as

$$E_{\mathrm{s}}(2\omega) \propto \int d\Omega \, E_{\mathrm{s}}(\omega + \Omega) \, E_{\mathrm{s}}(\omega - \Omega). \tag{2.52}$$

The intensity of the second harmonic is given by absolute square of $E_{\mathrm{s}}(2\omega)$:

$$I(2\omega) \propto \left| \int d\Omega \left| \widetilde{E}(\omega + \Omega) \right| \left| \widetilde{E}(\omega - \Omega) \right| e^{i\,[\varphi(\omega+\Omega)+\varphi(\omega-\Omega)]} \right|^2. \tag{2.53}$$

According to Equation 2.52 and Equation 2.53, the second-harmonic generation process is understood as the exchange of photons between frequency ω and 2ω. A 2ω-photon is simultaneously generated when two ω-photons are destroyed in a quantum-level system, as shown in Fig. 2.9 (b). The solid line denotes the atomic ground state while the dashed lines represent the virtual levels, the value of which equals to the combined energy of an eigenvalue atomic state and one or more photons.

Experimentally, the beta barium borate (BBO) crystal is often used for the second harmonic generation. For high conversion efficiency, a phase matching condition

$$\overrightarrow{k}_{2\omega} = \overrightarrow{k}_{\omega} + \overrightarrow{k}_{\omega} \tag{2.54}$$

needs to be fulfilled, where $\overrightarrow{k}$ is the wave vector. Experimental details on the second harmonic generation will be discussed in Section 3.4.2.

Chapter 3

Ultrashort laser pulses

In order to record an object's fast motion, we need a camera with the exposure time less or at least comparable to the motion. Similarly, to probe the electronic dynamics of atoms and molecules which have the timescale of femtoseconds or even attoseconds, light pulses with the duration of the same timescales (known as ultrashort laser pulses) are in high demand. Nowadays the Ti:Sapphire laser has been widely used in strong-field physics thanks to its advantage of providing high time-resolution and intensity. The laser pulse can be compressed to a few optical cycles, corresponding to few femtoseconds for the central wavelength of 800 nm. How do we generate such short laser pulses? Is it possible to further compress the pulses? Can we change the shape of the laser fields?

In this chapter we will answer these questions by introducing the theory of ultrashort laser pulses and experimental setups of the laser system which are used in the framework of this thesis. Furthermore, we present an intuitive and accessible time-domain pulse compression method in the second section. Followed by the pulse compression method, a pulse shaping method which is based on the superposition of the fundamental laser pulse and its second harmonic is introduced. The design and build-up of a two-color interferometer is then described in the last section of this chapter.

3.1 Generation of ultrashort laser pulses

3.1.1 Mathematics of ultrashort laser pulses

For linearly polarized ultrashort laser pulses, the time-dependent electric field at a fixed position is described as follows:

$$\widetilde{E}(t) = \widetilde{E}_0(t)e^{i\phi(t)}, \tag{3.1}$$

where $\widetilde{E}_0(t)$ and $\phi(t)$ are the complex envelope and the temporal phase of the laser pulse respectively [Mey14]. The real part of $\widetilde{E}(t)$ is the measurable electric field of the pulse. The intensity of the laser $I(t)$ is given by

$$I(t) = \left|\widetilde{E}(t)\right|^2. \tag{3.2}$$

With the help of the Fourier transformation, we are able to calculate the representation of the laser pulse in the frequency domain

$$E(\omega) = \frac{1}{\sqrt{2\pi}} \int_{-\infty}^{\infty} \widetilde{E}(t)\, e^{-i\omega t} dt. \tag{3.3}$$

The electric field in the time domain can be obtained by the inverse Fourier transformation

$$\widetilde{E}(t) = \frac{1}{\sqrt{2\pi}} \int_{-\infty}^{\infty} E(\omega)\, e^{i\omega t} d\omega. \tag{3.4}$$

The complex function $E(\omega)$ in Equation 3.3, which can be written as

$$E(\omega) = A(\omega)\, e^{i\phi(\omega)}, \tag{3.5}$$

is not measurable. However, in experiment, the intensity distribution in the frequency domain

$$I(\omega) = |E(\omega)|^2 = |A(\omega)|^2 \tag{3.6}$$

can be directly measured by a spectrometer. Combining the Equation 3.4 and Equation 3.5, we can write the time-dependent electric field in the following form:

$$\widetilde{E}(t) = \frac{1}{\sqrt{2\pi}} \int_{-\infty}^{\infty} A(\omega)\, e^{i(\omega t + \phi(\omega))} d\omega. \tag{3.7}$$

According to this equation (Equation 3.7), the electric field of ultrashort laser pulses can be interpreted as a superposition of a series of spectral components having the spectral amplitude $A(\omega)$ and the spectral phase $\phi(\omega)$. Thus, the temporal shape of the pulse is determined by its spectrum. In general, pulse duration τ and bandwidth $\Delta\omega$ refer to the full width at half maximum (FWHM) of the pulse profile in time and frequency domain, respectively. Due to the uncertainty principle, they have the following relation

$$\tau \cdot \Delta\omega \geq 2\pi c_{\mathrm{B}}. \tag{3.8}$$

c_{B} is determined by the pulse shape. For a Gaussian-shape pulse, $c_{\mathrm{B}} = 0.441$ [DR06].

Equation 3.8 tells us that the broader the spectrum of a laser pulse is, the shorter pulse duration can be obtained. For a given bandwidth in the frequency domain, we can achieve a pulse with a minimum pulse duration in the time domain. This pulse is named as Fourier-limited pulse. The minimum pulse duration is called Fourier limit or bandwidth limit, which is an important reference for comparing pulse compression methods (see details in Section 3.3).

The temporal phase function $\phi(t)$ in Equation 3.1 plays a key role in determining the shape of laser pulses. We now investigate the influence on the pulse property by performing a Taylor series expansion on this phase function

$$\phi(t) = \phi_0 + \frac{\partial \phi}{\partial t} t + \frac{1}{2} \frac{\partial^2 \phi}{\partial t^2} t^2 + ... \tag{3.9}$$

The constant ϕ_0 is called carrier envelope phase (CEP), which is defined as the phase offset between the maximum of the electric field and the maximum of the envelope. The
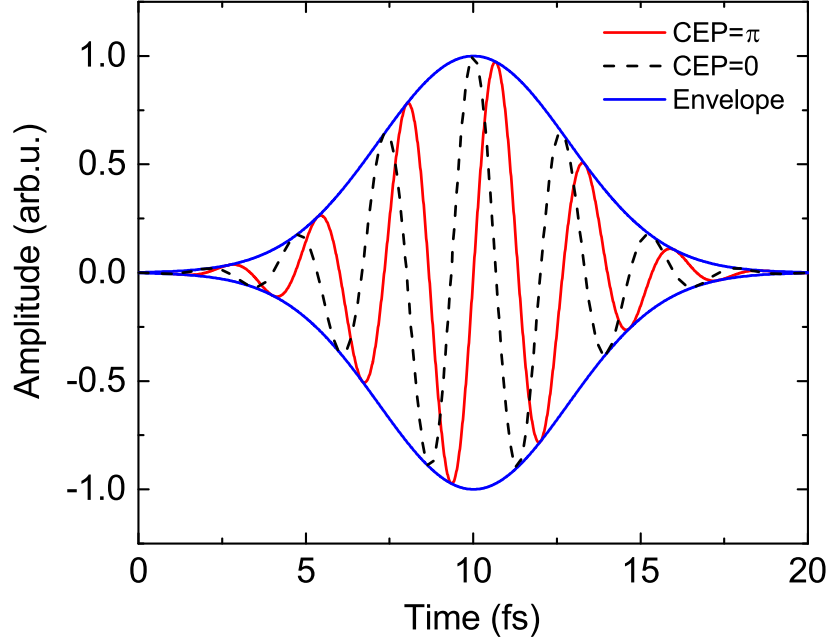
Figure 3.1: The time-dependent electric field for a carrier envelope phase $\phi_0 = 0$ (black dashed line) and $\phi_0 = \pi$ (red solid line) and the pulse envelope (blue solid line).

temporal electric field of ultrashort laser pulses for two different CEPs (0 and π) is shown in Fig. 3.1. For the pulse whose duration is larger than tens of optical cycles, the CEP effect plays a less important role. However, for pulses containing only a few cycles, this CEP significantly changes the pulse shape, thus highly affecting the ionization process [Fis10]. Note that the first order derivative of the temporal phase corresponds to shifts in frequency. We can rewrite the Equation 3.9 in the following form

$$\phi(t) = \phi_0 + \omega_0 t + \varphi(t) \tag{3.10}$$

where ω_0 is the central frequency and $\varphi(t)$ contains the n-th order of t ($n \geq 2$). The instantaneous frequency is defined as

$$\omega(t) = \frac{d\phi(t)}{dt} = \omega_0 + \frac{d\varphi(t)}{dt}. \tag{3.11}$$

If $d\varphi/dt = 0$, the instantaneous frequency is time independent and this corresponds to the Fourier-limited pulse. However, for most cases, the instantaneous frequency changes with time ($d\varphi/dt \neq 0$) due to dispersion (see Section 3.1.2), giving rise to a longer pulse in the time domain than the Fourier-limited pulse. If the time-dependent instantaneous frequency increases with time, the pulses are known as up-chirped pulses [shown in Fig. 3.2 (a)]. Analogously, if $\omega(t)$ decreases with time, they are called down-chirped pulses [shown in Fig. 3.2 (b)].
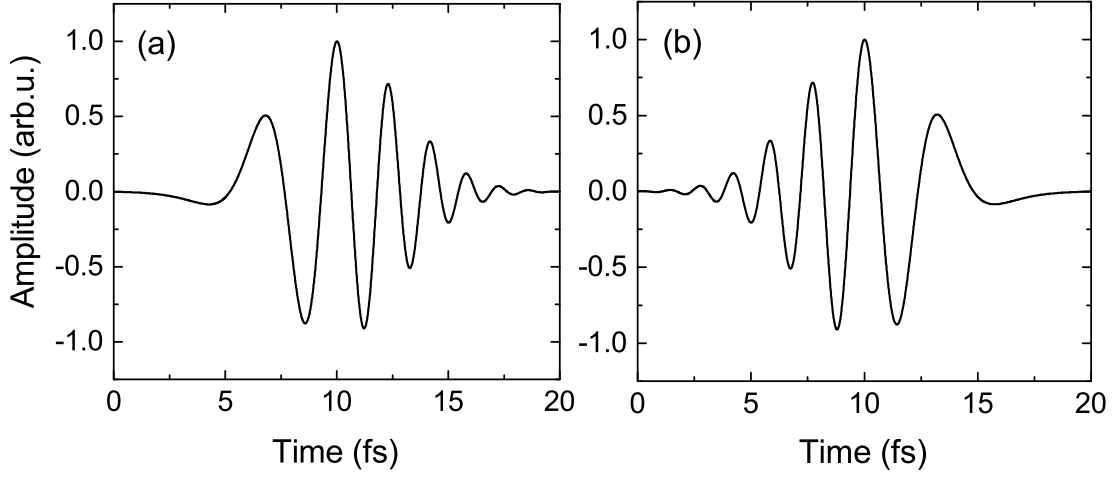
Figure 3.2: Electric field of an up-chirped pulse (a) and a down-chirped pulse (b).

3.1.2 Laser pulse dispersion

Now we consider the propagation effect of a laser pulse in a dispersive medium. As the refractive index of the medium is dependent on the frequency of the laser pulse, the different frequency components have different phase velocity when propagating through the medium. This phenomenon is known as dispersion, which become more pronounced for few-cycle ultrashort laser pulses due to its broad spectrum. The electric field of a pulse propagating along the z-axis can be written as

$$\widetilde{E}(z,\omega) = \widetilde{A}(z,\omega)e^{i\phi(\omega)}e^{-ik(\omega)z}. \tag{3.12}$$

The frequency-dependent wave vector $k(\omega)$ is given by

$$k(\omega) = \frac{\omega n(\omega)}{c}, \tag{3.13}$$

where c is the speed of light in vacuum. Inserting the above equation into Equation 3.12,

$$\widetilde{E}(z,\omega) = \widetilde{A}(z,\omega)e^{i(\phi(\omega)-\omega n(\omega)z/c)}, \tag{3.14}$$

we know that a laser pulse gains a spectral phase when propagating along the z-axis

$$\varphi(\omega) = \frac{\omega n(\omega)}{c}z. \tag{3.15}$$

In order to analyze the contributions of different frequency components, we again use Taylor series expansion on the $\varphi(\omega)$ at the central frequency ω_0

$$\varphi(\omega) = \varphi(\omega_0) + \left.\frac{\partial\varphi}{\partial\omega}\right|_{\omega_0}(\omega-\omega_0) + \frac{1}{2}\left.\frac{\partial^2\varphi}{\partial\omega^2}\right|_{\omega_0}(\omega-\omega_0)^2 + \mathcal{O}(\omega^3) \tag{3.16}$$

$$= a_0|_{\omega_0} + a_1|_{\omega_0}(\omega-\omega_0) + \frac{1}{2}a_2|_{\omega_0}(\omega-\omega_0)^2 + \mathcal{O}(\omega^3), \tag{3.17}$$

where

$$a_0 = \frac{z}{c}\omega n(\omega) \tag{3.18}$$

$$a_1 = \frac{z}{c}\left(n(\omega) + \omega\frac{\partial n(\omega)}{\partial \omega}\right) \tag{3.19}$$

$$a_2 = \frac{z}{c}\left(2\frac{\partial n(\omega)}{\partial \omega} + \frac{\partial^2 n(\omega)}{\partial \omega^2}\right) \tag{3.20}$$

The zero-order coefficient a_0 refers to as the absolute phase offset. Note that the group velocity v_g is defined as

$$v_g = \left(\left.\frac{\partial k}{\partial \omega}\right|_{\omega_0}\right)^{-1}. \tag{3.21}$$

By inserting Equation 3.13 into Equation 3.21, we resolve the first-order coefficient a_1 as follows

$$a_1 = \frac{z}{v_g} = \Delta t, \tag{3.22}$$

which denotes the time delay Δt the pulse spent when traveling the distance z in the dispersive medium. This is also known as the group delay (GD). The second-order coefficient is called group delay dispersion (GDD). In analogy, the higher order coefficients are named third-order dispersion (TOD), fourth-order dispersion (FOD) and so on. The GD does not change the temporal shape of the pulse. However, the GDD affects the profile of the laser pulses, as different frequency components have different phase velocities and they separate from each other in the time domain. For a non-zero GDD, if the coefficient $a_2 > 0$, the GDD is called normal dispersion. That means the laser pulses with longer wavelength travel faster than the pulses with shorter wavelength. Otherwise the GDD is called anomalous dispersion. The TOD brings more complicated effects on the pulse shape, e.g. it can split the pulse into several sub-pulses [Mey14]. In order to retrieve the shortest pulse from the dispersed pulse, dispersion has to be compensated such that the pulse is compressed to its Fourier limit.

For chirped pulses, on one hand, they can be gained experimentally from their corresponding Fourier-limited pulses by inserting a glass (or other dispersive materials) in their optical paths. On the other hand, the chirped pulses can be compressed to the shortest pulse or even shaped in the temporal profile by manipulating their spectral components in a controllable way. For example, chirped mirrors and prisms [FCBS87, BWPW97, APPM01, YZO$^+$03, PAF$^+$09] are widely used in the femtosecond laser system (Section 3.1.3) to compensate the dispersion by flattening the spectral phase.

3.1.3 Laser system

Since the invention of the first laser [Mai60] in 1960, more and more types (gas, dye or solid) of lasers with the wavelength ranging from ultraviolet to far-infrared are widely used not only in scientific research but also in daily life (e.g. distance/time measurement,
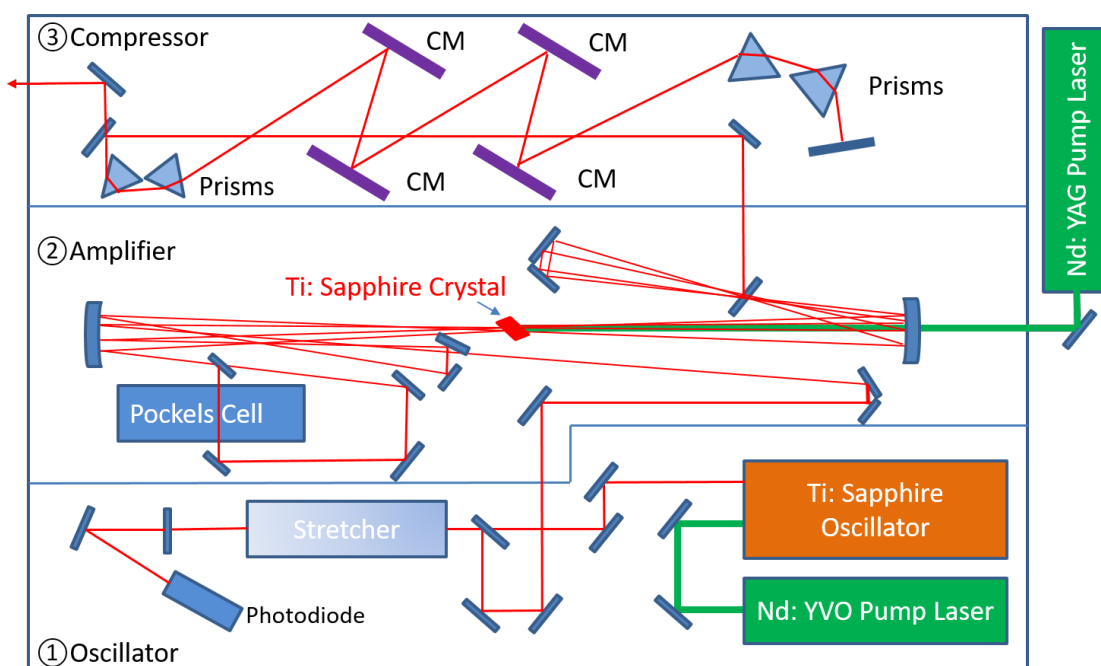
Figure 3.3: Schematic setup of the Ti:Sapphire laser system. A pulse train is generated from the mode-locked oscillator which is pumped by a continuous laser. The pulses are stretched in time domain and then amplified in the amplifier by chirped pulse amplification (CPA). The amplified chirped pulses are further compressed by chirped mirrors (CM) and prism compressors.

eye surgery, laser pointer and so on). Thanks to the Kerr lens mode-locking (KLM) technology [Rul05], we are nowadays able to create ultrashort laser pulses with the time scale of femtoseconds. When focused, the intensity of the pulses can reach 10^{14} to 10^{15} W/cm^2, making the electric field comparable to the Coulomb field inside the atoms or molecules.

The laser system used in the framework of this thesis is a commercial amplified titanium doped sapphire (Ti:Sapphire) laser, in which linearly polarized 25 fs laser pulses are generated at the central wavelength of 800 nm. The laser system (depicted in Fig. 3.3) consists of three parts: the oscillator, the amplifier and the compressor.

The Ti:Sapphire oscillator, which is pumped by a continuous-wave (cw) Nd:YVO laser at a wavelength of 532 nm with the pump power of 3 W, delivers a pulse train with the pulse duration of less than 10 fs and the pulse energy of a few nanojoules. The repetition rate of the oscillator is 80 MHz. Due to the Kerr effect [Rul05], the refractive index of a material increases with the intensity of the laser, which gives rise to the focusing of the laser beam (Kerr-lens). The oscillator takes advantage of this principle, in which high-intensity beams are better focused than the low-intensity ones and have a higher gain from the Ti:Sapphire crystal. The center of the pulses are thus enhanced more than the edge in the time domain, leading to a short pulse duration. With the help of the Kerr lens, the phase of different frequency components can be locked in the time domain. This effect is called mode locking and can be triggered by introducing a perturbation of the cw laser in a very short time duration. The measured spectrum with the mode locking after the oscillator is thus broadened, shown in Fig. 3.4.
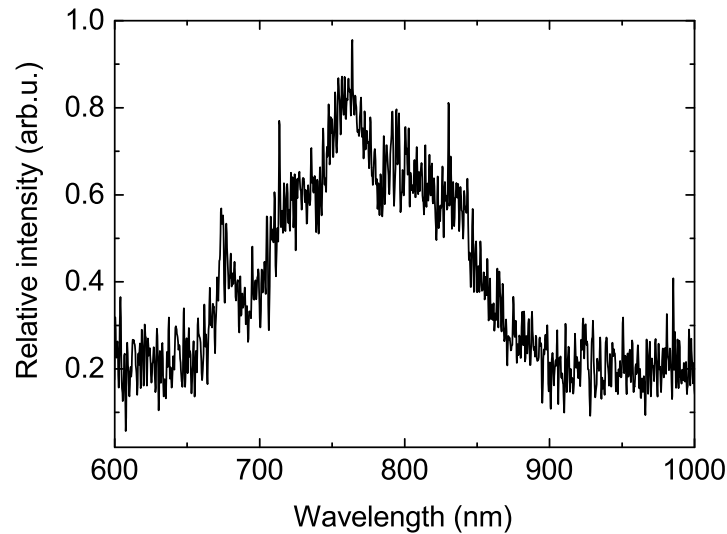
Figure 3.4: Measured mode locked spectrum after the oscillator.

Short-pulse-duration (10 fs) and high-repetition-rate (80 MHz) laser pulses are generated from the oscillator, however, the pulse energy is still not sufficient for most experiments as the intensity of the focused beam is much lower than the ionization limit of most noble gases. In order to amplify the pulse energies from the scale of nanojoules to millijoules, the chirped pulse amplification technique [SM85] is used. As shown in Fig. 3.3, before the pulses enter the amplifier region, they are passed through a stretcher, in which a large temporal chirp is introduced by using a dispersive material (e.g. a thick glass) and the pulses are stretched in the time domain to the duration of picoseconds. After the stretcher, the pulses are sent to the amplifier in which the pulses pass through a Ti:Sapphire crystal back and forth for nine times. The idea of the chirped pulse amplification is that the long pulses can be easily amplified in the amplifier without damaging any optical materials and the gain medium. The Ti:Sapphire crystal is pumped by a pulsed Nd:YAG laser at a repetition rate of 3 kHz. The Q-Switched pump laser has a high power up to 40 W with the wavelength of 532 nm. A Pockels cell is set after the fourth pass and used for picking up only one pulse from the pulse train for further amplification. After the amplifier, more than 1 mJ pulses at a repetition rate of 3 kHz are obtained and then sent to the compressor.

The compressor is made up of a series of chirped mirrors and prism pairs, which are designed for compensating the third-order dispersion and thus compressing the pulse in the time domain. The duration of the pulses in the final output of the laser system is around 25 fs. In this thesis, the 25-fs pulse is sufficient for the measurements with two-color laser fields, which will be presented in Chapter 5 and Chapter 6. However, for some other measurements with the CEP-stabilized pulses which normally have the pulse duration as short as 4-5 fs, we need to use a hollow-core fiber and chirped mirrors for further compression. This compression is based on the self-phase modulation (SPM) effect. The fiber broadens the spectrum and thus reduces the Fourier limit of the pulses. More details of the generation of few-cycle laser pulses can be found in [Fis10, Cam13].
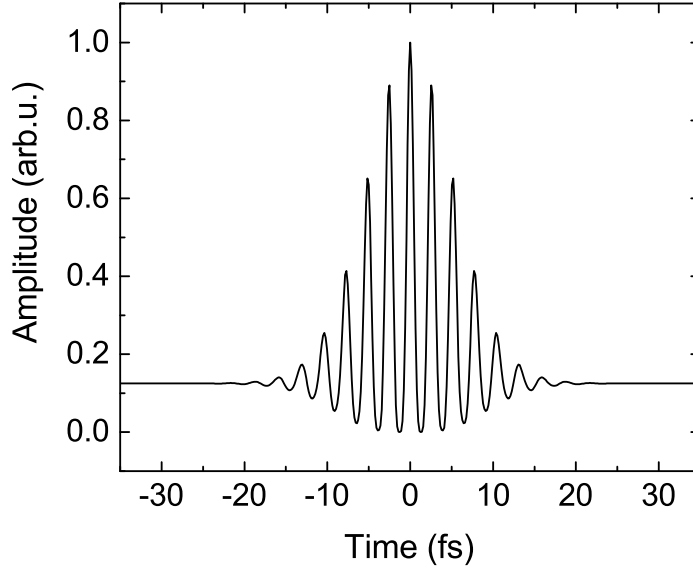
Figure 3.5: Second-order interferometric autocorrelation signals. Figure adapted from [Mey14].

3.2   Pulse characterization

In order to measure the temporal shape (waveform) of the ultrashort laser pulses, resolution in the femtosecond time scale is required. Even the fastest electronic devices cannot respond for such a short time. One way to characterize the ultrashort laser pulses is using interferences, i.e. measuring the pulse with the copy of pulse itself.

The most straightforward pulse characterization method is called autocorrelation, which can be experimentally realized with the use of a Mach-Zender (see Section 3.4.2) or Michelson interferometer. In such interferometers, a laser pulse is splitted into two identical pulses by a beamsplitter. A time delay τ is introduced for one pulse and can be tuned with respect to the other pulse. Given that the electric field of the pulse is $E(t)$, the recombined electric field $E_{\text{total}}(t)$ is expressed as

$$E_{\text{total}}(t) = E(t) + E(t - \tau). \tag{3.23}$$

The interferometric autocorrelation signal is given by [Rul05, DR06]

$$I_n(\tau) = \int_{-\infty}^{\infty} dt \, \left| [E(t) + E(t - \tau)]^2 \right|^n. \tag{3.24}$$

Here, n denotes the order of autocorrelation, which can be realized by an n-photon process. In particular, the second-order interferometric autocorrelation signal can be detected by an autocorrelator based on the second harmonic generation in a nonlinear crystal. Fig. 3.5 shows an example of a second-order autocorrelation signal, which is measured by the contrast ratio of 8:1 between the peak (amplitude at $\tau = 0$) and the background signal (amplitude at $\tau \to \infty$).

Though the autocorrelation method could provide the pulse duration if we know the temporal shape of the pulse, the retrieval of the complex electric field in the time or frequency domain is not possible. In order to obtain the complete information on the laser pulses, the spectral amplitude and phase have to be known. With the development of the ultrashort laser system in the 1990s, two advanced methods, frequency-resolved optical gating (FROG) [KT93, TK93] and spectral phase interferometry for direct electric-field reconstruction (SPIDER) [IW98] were invented for the full pulse characterization.

The FROG is improved from the autocorrelation method. It measures the spectrum of the generated second harmonic laser pulses as a function of the time delay τ between the two pulse replicas, which is known as FROG trace:

$$I_{\text{FROG}}(\tau, \omega) \propto \left| \int_{-\infty}^{\infty} E_{sig}(t, \tau) \, exp(-i\omega t) dt \right|^2, \tag{3.25}$$

where the signal-pulsed field

$$E_{\text{sig}}(t, \tau) \propto E(t) \left| E(t - \tau) \right|^2. \tag{3.26}$$

An iterative search procedure is performed for the assumed electric field and thus the FROG trace can be calculated from Equation 3.25. By comparing the calculated and the experimental FROG trace, the electric field of the laser pulse is possibly reconstructed.

SPIDER is another self-referencing technique [GSM+00] which has been widely used in the measurement of ultrashort femtosecond laser pulses. Briefly speaking, this method acquires the spectral phase information by an interferometric technique. Compared with the FROG, the phase retrieval process is faster and more importantly non-iterative [IW98]. The amplitude of the spectrum can be easily measured with a spectrometer. With both amplitude and phase information in the frequency domain, the time-dependent electric field $E(t)$ can be obtained by the Fourier transformation (see Section 3.1.1). Details of the SPIDER technique can be found in [Pfe04].

3.3   Pulse compression in the time domain

As described in Section 3.1.2, GDD has to be considered when laser pulses are transmitted through dispersive media or even air because it increases the pulse duration of an initially Fourier-limited pulse. Thus, pulse compression is essential for the generation of ultrashort laser pulses. For instance, chirped mirrors and prisms are widely used to compensate the dispersion and further compress the pulses in the femtosecond laser system (see Section 3.1.3). These compressors are designed to compensate a slowly varying spectral phase by adding smooth dispersion such that the phases of all frequency components are flattened in the frequency domain [FCBS87, BWPW97, APPM01, YZO+03, PAF+09]. Time-domain pulse compression method was firstly used for radio frequency pulses [FM72]. For optical pulses, there are numerous methods used for compressing pulses to their Fourier-limited duration such as chirped fiber Bragg gratings (CFBGs) [GVT+11, LLWY11, BSV09], time-domain optimized chirped multilayer mirrors [DYO+05, BBdRW+12], Gires-Tournois interferometers [HSS03], programmable acoustic optic dispersive filters [OMB+12, VLC+00, SHS+03] and some

other pulse shaping methods based on feedback-loop schemes (e.g. evolutionary algorithm) [YMS97, BBS$^+$97, Ser13]. However, for most of these pulse-compression methods, the laser pulses have to be transmitted through dispersive materials which are only adaptable to light with limited photon energy or bandwidth.

In this section we introduce an intuitive pulse compression method in which laser pulses can be directly manipulated in the time domain [MKMP13]. By coherent superposition of the electric fields of the laser pulses with individual delays in the time domain, chirped and complex pulses are efficiently compressed close to their corresponding Fourier-limited pulses. Compared with traditional compression methods, this method has no photon energy nor bandwidth limitation and can be applied to the compression of random laser pulses.

3.3.1   Basic principle

The electric field of an arbitrary pulse can be written as

$$E(t) = E_0 f(t) \left[\cos(\omega(t)t + \Delta\varphi\right], \tag{3.27}$$

where E_0 is the amplitude of the laser field, $f(t)$, $\omega(t)$ and $\Delta\varphi$ denote an envelope function, the time-dependent frequency and the CEP respectively. The key idea of the first method is shown in Fig. 3.6 (a). We assume that t_0 is the instant when the amplitude of the E-field of the laser pulse reaches the global maximum and $t_{-m}, t_{-m+1}, ... t_{-1}, t_1, ... t_n$ are the times when the amplitudes of the pulse reach the local maxima. Here, m and n are integers. The first step of the method is to generate $n + m + 1$ pulse replicas. Afterwards, these local maxima of the replicas are shifted to t_0 by a time-delay operation in the time domain. At the time t_0, constructive interferences occur such that the maximum of the amplitude of the pulse increases significantly. In the wings of the pulse, destructive or at least partially destructive interferences occur and thus reduce the total pulse duration. The electric field of the compressed pulse by using the method is

$$E_{\text{out},1}(t) = \sum_{i=-m}^{n} E(t + t_i - t_0). \tag{3.28}$$

For some cases, the amplitude of a local maximum is small compared to the global maximum while its location is far away from t_0. If we apply the above-mentioned method (Method 1) to these pulses, the pulse duration may increase after compression because the destructive interference condition in the wing might not well be fulfilled. Thus, Method 1 can be improved by introducing an amplitude-weighting function $A(t)$. The function is chosen as follows:

$$A(t) = E(t)/E(t_0). \tag{3.29}$$

Multiplying the electric field of pulse replicas by their corresponding amplitude-weighting function $A(t)$ and then shifting them from t_i to t_0 [shown in Fig. 3.6 (b)], we obtain the final field of the laser pulse

$$E_{\text{out},2}(t) = \sum_{i=-m}^{n} A(t_i) E(t + t_i - t_0). \tag{3.30}$$
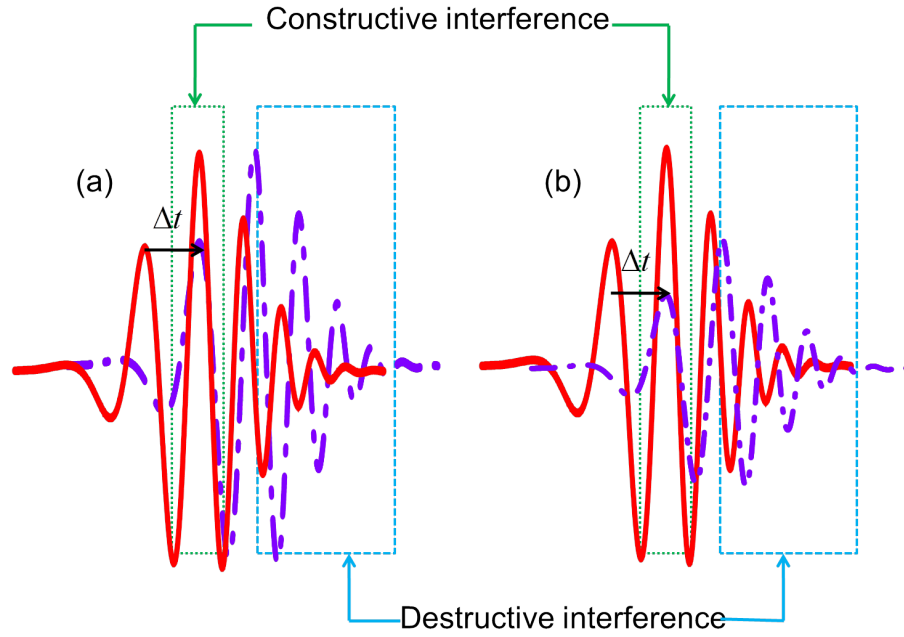
Figure 3.6: Principles of two time-domain pulse compression methods: (a) All pulse replicas are shifted in the time domain such that constructive interference occurs at a specific time (Method 1). (b) In addition to the time-delay operations as Method 1, an amplitude-weighting function is applied to decrease the contribution of replicas at large delay times (Method 2). Figure adapted from [MKMP13]

3.3.2 Simulation results

Numerical simulations for a chirped pulse and statistical pulses are carried out in order to test the validity of the two pulse compression methods. With the help of a peak-search algorithm, the global and local maxima of the electric field can be sorted out. According to Equation 3.28 and Equation 3.30, time-delay operations are applied directly on the electric field of the pulse replicas in the time domain.

Particularly, we choose a linearly chirped pulse whose electric field is expressed as

$$E(t) = \exp(\frac{-t^2}{16})\cos(\omega t + 0.15t^2), \tag{3.31}$$

where ω is the frequency corresponding to a wavelength of 800 nm and the time t is in units of femtoseconds. The initial pulse shape (electric field) and the intensity distribution are shown in Fig. 3.7 (a) and (b). From the intensity distribution, the FWHM of this pulse can be calculated as 4.71 fs. By shifting 8 pulse replicas from their corresponding local maxima position to the global maximum t_0 in the time domain and superposing them according to the two methods, we obtain the electric field and the intensity of the compressed pulse, shown in Fig. 3.7 (c) and (d). For comparison, the Fourier-limited pulse of the initial chirped pulse is plotted in green dashed curve in Fig. 3.7. Normalizing the intensity distributions of the compressed pulses, we acquire the pulse durations (FWHM) of 2.02 fs and 2.59 fs for Method 1 and Method 2, respectively. Though the pulse duration using Method 2 is larger than the one using Method 1, the compressed pulse has less
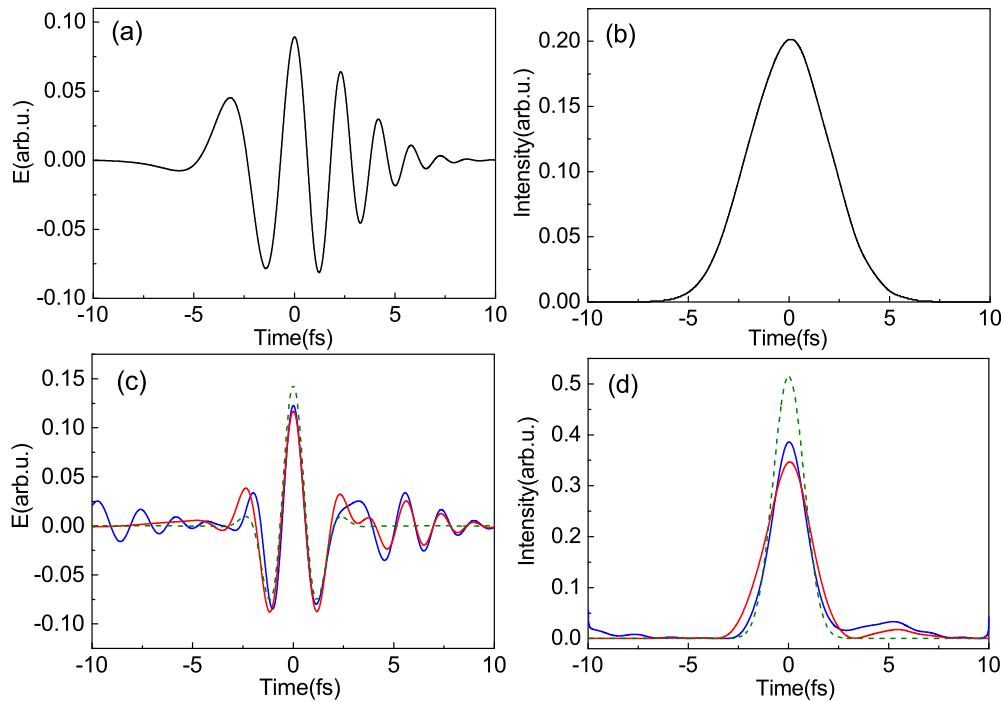
Figure 3.7: (a) The time-dependent electric field and (b) intensity distribution of a linearly chirped pulse (c) The electric field and (d) intensity distribution of the compressed pulses using Method 1 (blue solid curve) and Method 2 (red solid curve). The corresponding Fourier-limited pulse of the initial pulse was shown in green dashed curve for comparison. Figure adapted from [MKMP13]

satellite peaks. Compared with the Fourier-limited pulse (FWHM 1.83 fs), both methods generate a pulse duration close to the shortest one.

Now we consider a more general pulse with a complex statistical pulse shape. For example, the free electron laser (FEL) pulse exhibits the noisy and statistically varying shape [PJD+10] due to the so called self-amplified spontaneous emission (SASE) process. These noisy pulses have been demonstrated to enhance the temporal resolution of spectroscopy for some pump-probe measurements [MOR+12]. As an example of these pulses, the electric field and intensity of a statistical pulse are shown in Fig. 3.8 (a) and (b). Before applying Method 1 and Method 2 on the pulse, we need to determine the number of pulse replicas. In principle, the number is the same as the number of the peaks of the electric field. However, in the simulation, we have to set a threshold below which all the peaks are not considered. This means there exists an optimal number of replicas which bring the shortest pulse. Applying the optimal number of delay operations, the above pulse was compressed such that a fully constructive interference occurs at t_0 while the destructive interference occurs in the wings [shown in Fig. 3.8 (c) and (d)]. For both methods, after the compression, the amplitude of the main peak becomes sharp while the satellite peaks are depressed effectively. For this case, the pulse using Method 2 [red curve in Fig. 3.8 (c) and (d) and the inset] not only gains a shorter pulse duration than the pulse using Method 1 [blue curve in Fig. 3.8 (c) and (d) and the inset] but also reduces contributions of the residual satellite peaks, leading to a sharper pulse shape which is significantly close to the corresponding Fourier-limited pulse [green curve in Fig. 3.8 (c) and
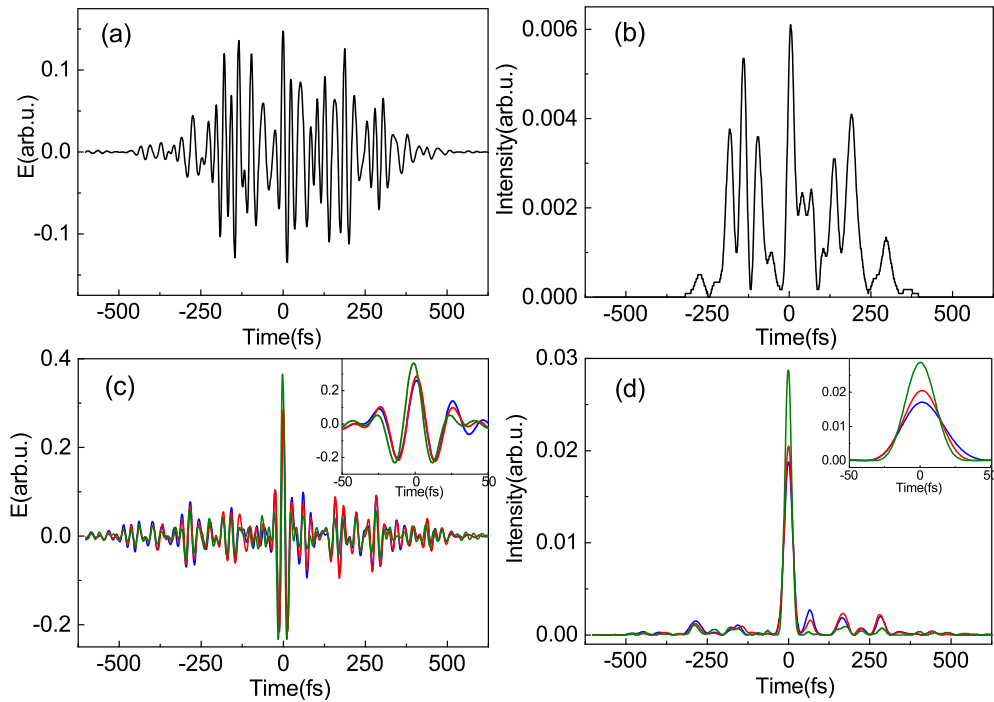
Figure 3.8:   The temporal electric field and intensity distribution of the initial statistical pulse [(a) and (b)] and the compressed pulse [(c) and (d)]. The inset of (c) and (d) shows the zoomed area in the time domain from -50 fs to 50 fs. Blue curve: pulse compressed using Method 1. Red curve: pulse compressed using Method 2. Green curve: the Fourier-limited pulse. Figure adapted from [MKMP13]

(d) and the inset].

In order to prove the general applicability of the compression method, a large set of statistical pulses are required. In the simulation, 10000 random noisy pulses are generated with the same envelope. That ensures all the statistical pulses have the same average pulse duration (0.5 ps). These pulses are then compressed by using Method 1 and Method 2. The original, compressed and the Fourier-limited pulse durations for the linearly chirped pulse [in Fig. 3.7], average of 10000 random pulses including four individual statistical pulses are listed in Table 3.1. The standard deviation of the 10000 random pulses for Method 1, Method 2 and the Fourier-limited pulse is 5.33 fs, 5.37 fs and 1.52 fs, respectively. From Table 3.1, we see the Method 2 with an amplitude-weighting function is more efficient than Method 1 in the compression of the complex statistical pulses.

In conclusion, we describe a straightforward and general time-domain pulse compression method based on the coherent superposition of pulse replicas with specific time delay operations. Due to the constructive interference at the peak and destructive interferences in the wings, the pulse can be efficiently compressed close to the shape of its Fourier-limit pulse. Though this method requires the knowledge of the initial pulse and thus has limitation in the compression of FEL pulse, it provides an option to compress the pulse in the time domain if measurable and stable laser pulses become possible in the future. Details of the method (e.g. spectral modification of compressed pulses and scaling the number of pulse replicas) can be found in [MKMP13].

Table 3.1: Comparison for the compression methods [MKMP13]

Pulse duration	Original pulse	Method 1	Method 2	Fourier-limited
Chirped pulse with linear phase	4.74 fs	2.02 fs	2.59 fs	1.83 fs
Statistical pulse (in Fig.3.8)	0.5 ps	34.20 fs	29.91 fs	24.71 fs
Statistical pulse 1	0.5 ps	39.54 fs	36.21 fs	25.71 fs
Statistical pulse 2	0.5 ps	33.66 fs	30.86 fs	25.01 fs
Statistical pulse 3	0.5 ps	36.69 fs	36.21 fs	23.68 fs
Average of 10000 random pulses	0.5 ps	38.15 fs	36.96 fs	25.62 fs

3.4   Sculpted laser fields

Slight changes of field shape of a laser pulse can remarkably change the ionization dynamics induced by the laser field. As we know from Section 3.1.1, CEP determines the shape of few-cycle infrared laser pulses generated from the Ti:Sapphire laser system. Such CEP-stabilized laser pulses have been proved to be a favorable tool for controlling the localization of electrons [KSV+06], the non-sequential double ionization [CFK+12], fragmentation of polyatomic molecules [XDDR+12] and so on.

In analogy to the CEP-stabilized laser field, in this section, we introduce another field shaping method – sculpted laser fields, which play a vital role in controlling the electronic wave packets [XRK+12] during strong-field photoionization processes. As suggested by the name, this method is realized by combining different laser fields in the time domain such that the overall field has a controllable shape. The most common scheme is the overlap between a laser field and its second harmonic, which is known as two-color laser fields. By tuning the relative time delay between the two fields, the shape of the recombined laser field can be precisely controlled.
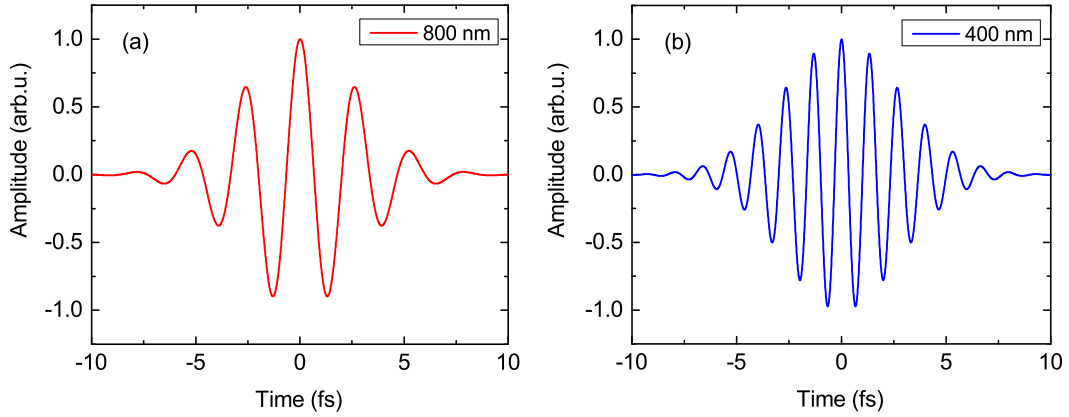
3.4.1   Simulation

What does the electric field look like if we coherently superimpose a fundamental-frequency laser pulse with its second-harmonic? To answer this question, a simulation on the superposition of 800 nm and 400 nm pulsed laser field is performed. In this simulation, the two pulses have the same envelope. The expressions of the electric fields of the 800 nm and 400 nm pulses are chosen as

$$E_{800\,nm}(t) = \exp(\frac{-t^2}{16})\cos(\omega t) \tag{3.32}$$

and

$$E_{400\,nm}(t) = \exp(\frac{-t^2}{16})\cos(2\omega t), \tag{3.33}$$

where ω corresponds to the wavelength of 800 nm. No linear or high-order chirps are implemented in these expressions, which means the chosen pulses are Fourier-limited

Figure 3.9: Temporal electric field of the initial 800 nm (a) and 400 nm (b) laser pulses in the simulation.

pulses. The time-dependent electric fields of the two pulses are shown in Fig. 3.9 (a) and (b), respectively. By means of the time-domain pulse compression method (See Section 3.3), one of the pulses is operated with a delay τ and superimposed with another pulse directly in the time domain. The electric field of the recombined pulse $E_{\text{two-color}}(t)$ is the sum of the two temporal electric fields given by

$$E_{\text{two-color}}(t) = E_{800\,\text{nm}}(t) + E_{400\,\text{nm}}(t - \tau).$$ (3.34)

The simulation results are shown in Fig. 3.10. When time delay τ varies from 0 to $T/4$ (T denotes the optical cycle of 400 nm laser pulse), the shape of the electric field changes from asymmetric in positive direction [Fig. 3.10 (a)] to symmetric [Fig. 3.10 (b)]. When the time delay between the two-color fields reaches half cycle of the optical period of 400 nm laser field, the total field is transformed back to an asymmetric shape but in negative direction [Fig. 3.10 (c)]. If we further increase the time delay by another $T/4$, the field returns to a symmetric shape again [Fig. 3.10 (d)].

Although the actual shape of laser pulses in experiment are not as ideal as Gaussian due to dispersion, this simulation proves that varying the relative time delay between the two-color pulses allows us to control the field shape, which can be further used for controlling electronic wave packets released in strong-field ionization processes.

3.4.2 Two-color interferometer

Experimentally, generation of sculpted two-color laser fields requires that two laser pulses should have equal optical paths. As an optical period of 800 nm and 400 nm pulses is only 2.67 fs and 1.33 fs respectively and the 800 nm pulse generated from the Ti:Sapphire laser contains approximately 10 cycles, having a precise control over the field shape requires a resolution of tens of nanometers for delay operations.

A two-color interferometer (shown in Fig. 3.11) is built with a beam splitter (BS), a high-precision piezo delay stage, a BBO crystal and a half waveplate. In order to have a high
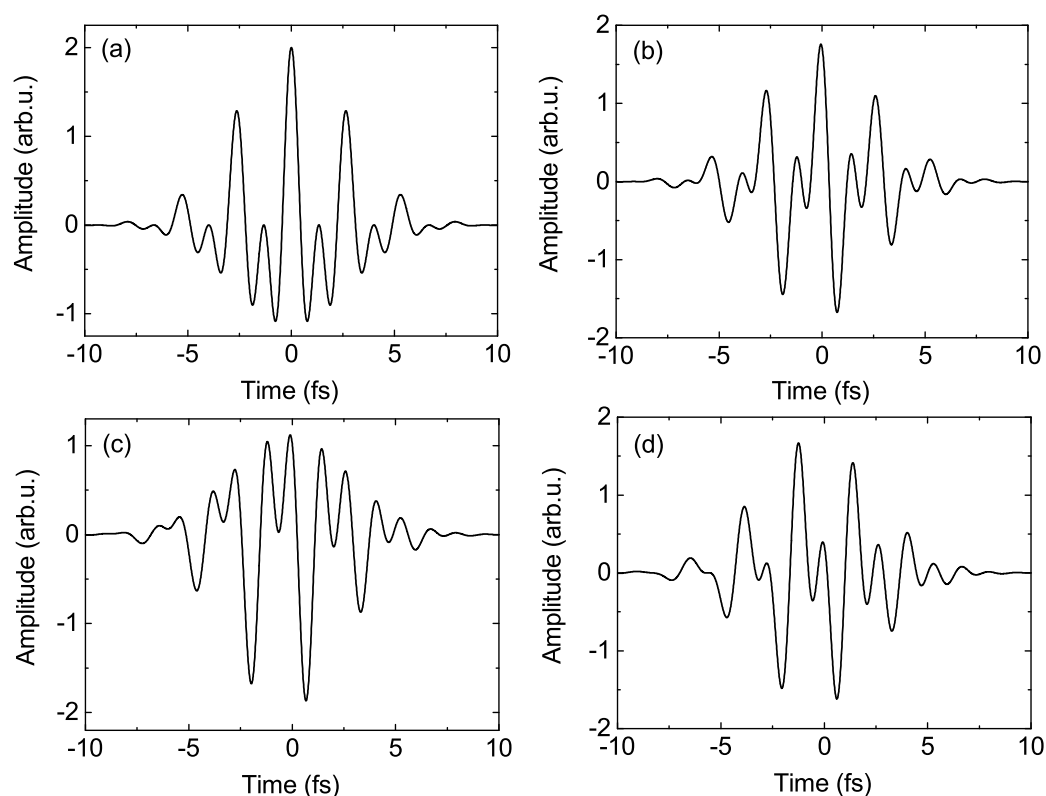
Figure 3.10: Temporal electric field of the recombined pulse between 800 nm and 400 nm laser pulses with different time delays: (a) $\tau = 0$ (b) $\tau = T/4$ (c) $\tau = T/2$ (d) $\tau = 3T/4$. T is the optical cycle of 400 nm pulses.

second harmonic generation (SHG) intensity, the laser beam should fit the size of the BBO crystal, which has a diameter of a few millimeters. However, the beam from the Ti:Sapphire laser normally has a diameter of 20 millimeters. That explains why we place a telescope composed of a focusing and a defocusing lens in front of the BS. 90% of the beam is transmitted through the BS and used for the second harmonic generation process. The BBO crystal has to be tilted and rotated such that the phase matching condition is fulfilled (see Section 2.3). After the BBO crystal, the polarization of the generated 400 nm pulse is rotated by 90 degree compared to the polarization of the 800 nm pulse. The half waveplate is used for changing the polarization such that after the interferometer the 400 nm laser pulse has the same polarization as the 800 nm pulse. For the other arm, the 800 nm pulse is delayed by a piezo delay stage with a precision of 80 attoseconds. Finally, the 800 nm and the 400 nm pulse are recombined by using a beam combiner and sent to a Reaction Microscope (REMI, see Chapter 4) for further measurements.

The two-color pulses need to overlap temporally and spatially in the REMI, which is placed few meters away from the interferometer. To make sure the two collimated beams after the beam combiner overlap in space, not only in the near field but also in the far field the blue (400 nm) and the red (800 nm) beam spots have to be spatially overlapped. For temporal overlap, a spectrometer is set where the two beams overlap spatially. Interference fringes in the frequency domain appear when the two pulses overlap in the
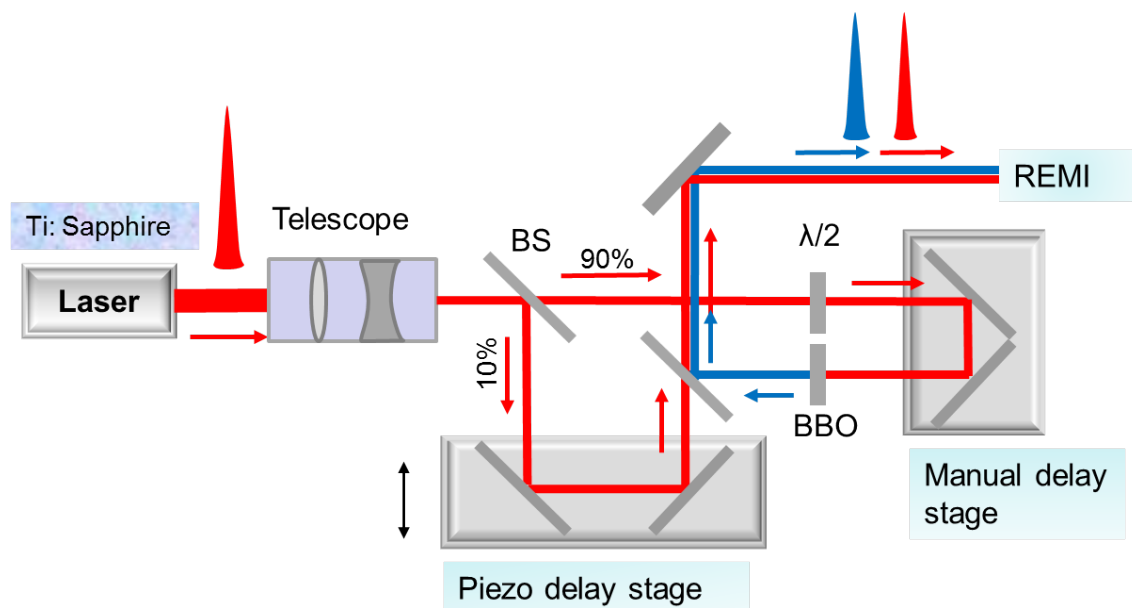
Figure 3.11:   Sketch of the two-color interferometer. The laser pulses generated from the Ti:Sapphire laser system are firstly reduced in the beam diameter by a telescope. The pulses are then splitted by a beamsplitter (BS) into two beams: one with 90% laser intensity is used for the second harmonic generation by passing through a BBO crystal and a half-waveplate (rotating the polarization of the laser by 90 degree), the other beam with 10% intensity is delayed by a piezo delay stage. The two beams are recombined by a beam combiner and sent to the Reaction Microscope (REMI) for measurement.

time domain. We can also verify the temporal overlap by monitoring the ionization yield (e.g. single ionization of Ar by the two-color fields) in the REMI as a function of the time delay between the two pulses. Once the two fields overlap in the time domain, the ionization count rate is significantly enhanced compared to the one with only red or blue laser field. For example, in the measurement of single ionization of Ar (see Chapter 5), the count rate when the two-color fields overlap is 1000 counts per second while this value decreases to 100 and 200 counts per second in the presence of only 400 nm and 800 nm laser pulse respectively.

Chapter 4

The Reaction Microscope

The Reaction Microscope (REMI) is a precise and high-resolution spectrometer used for measuring the momentum of electrons in coincidence with ions in the process of e.g. photon-induced ionization or ion-electron collision etc. In some cases REMI is also called cold target recoil-ion momentum spectroscopy (COLTRIMS). In this work we use REMI as a detector for measuring and reconstructing the momentum of electrons emitted from different species (see Chapter 5) or different ionization channels of molecules (see Chapter 6) in the process of laser-induced strong-field ionization. Details of development on techniques of the REMI can be found in [UMD$^+$03, DMJ$^+$00].

In the first section basic principles of the REMI including ion and electron detectors, spectrometer and gas jet are introduced. Following this section, reconstruction of the momenta of particles and details of data calibration are presented.

4.1   Basic principles

Fig. 4.1 shows the structure of the REMI used in our experiment. It mainly consists of a spectrometer in which a static electric field is applied to accelerate charged particles, two detectors for electrons and ions, a concave mirror for focusing the laser beam, a supersonic gas jet (target) and two Helmholtz coils. Focused laser beam and the gas jet intersect in the center of the REMI, where the ionization occurs and electrons and ions are released. With the help of the electric field and magnetic field, ions are guided to the ion detector while electrons fly to the electron detector with cyclotron motion due to their small masses compared to the ions. According to flight time of the particles and their positions on the detector, momenta of ions and electrons can be reconstructed with rather high resolution (see Section 4.2). A huge advantage of the REMI compared with a traditional time of flight (TOF) spectrometer or velocity-map imaging (VMI) apparatus is the coincident measurement on ions and electrons for a given event, which makes different ionization channels distinguishable and thus provides a complete kinematic information for the ionization process.
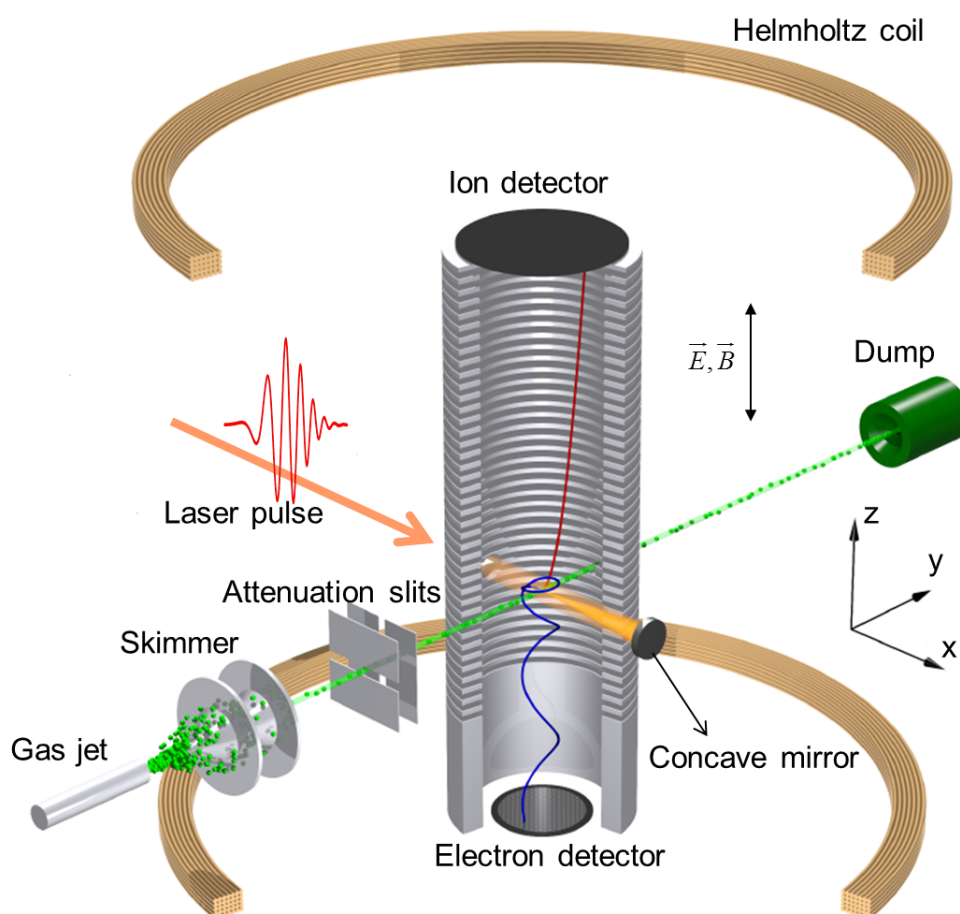
Figure 4.1:   Schematic graph of the Reaction Microscope. Along the *x*-axis a collimated laser beam is focused by a concave mirror into the center of the main chamber, where the laser intersects with the gas jet (*y*-axis). Ionized electrons and ions are guided to their detectors with the help of electric field and magnetic field along the spectrometer axis (*z*-axis). Figure adapted from [Fec14].

4.1.1   Spectrometer

As shown in Fig. 4.1, the main component of the REMI is the spectrometer, which is designed such that all interested ions and electrons are collected by their detectors. The spectrometer used in our experiments has an acceleration length of 30 cm and 10 cm for ions and electrons, respectively. For electrons, there exists a 10-cm-long field-free region (drift region) after the acceleration. A grid is placed to separate the acceleration and the drift regions. Two additional grids are set in front of the ion and electron detectors to improve the homogeneity of the field [Fec14]. The key factor to guide the particles is the electric field provided by a series of electrodes. An increasing strength of the electric field helps to collect high-energy particles, however, it decreases the momentum resolution because the increasing field strength leads to a shorter time of flight and a smaller spatial distribution. In our measurement, the acceleration field is adjusted to approximately 2 V/cm. This field is sufficient to extract the ions generated in the strong infrared laser field. However, this field alone is still not enough to collect all the electrons cre-

Channels   Incident particle

HV

Electron cloud
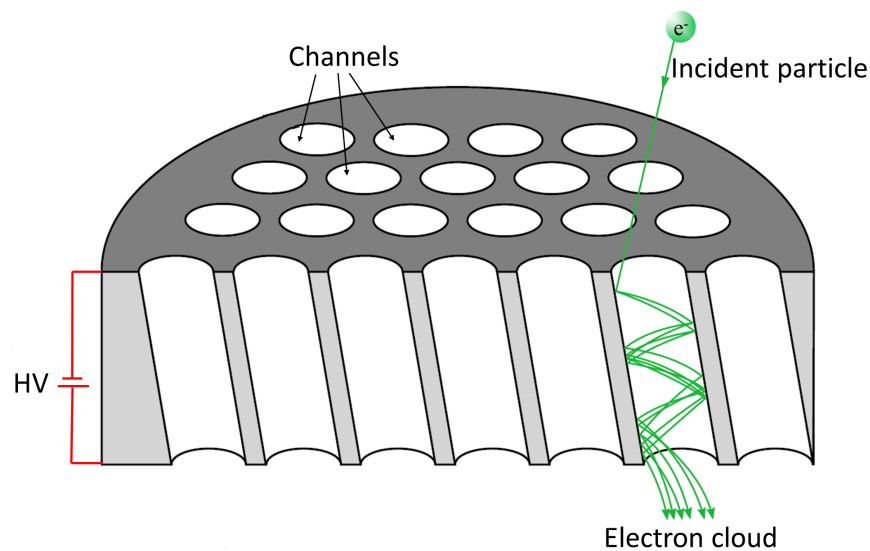
Figure 4.2: Working principle of a MCP. The incident particle (electron or ion) hits the channel and creates an electron avalanche. A high voltage (HV) is applied across the channel to accelerate the electrons. Figure adapted from [Pfl12].

ated in the same process. In order to extract the electrons properly and maintain a high momentum resolution, a magnetic field is applied to constrain the electrons close to the spectrometer axis (z-axis) within a cyclotron motion [MUU$^+$94].

The ion and electron detectors, each of which consists of two micro channel plates (MCPs) and a delay line anode, are set at the two ends of the spectrometer. Fig. 4.2 shows the working principle of a MCP. Normally, a MCP contains millions of separated channels which release secondary electrons when hit by the incident particle. The electron cloud is generated in an electron avalanche process and these created electrons are accelerated by a high voltage (1 - 2 kV) across the channel. In this way, the electron signal is amplified and measurable. With a delay line anode, the position where an incident particle hits the detector can be determined. The flight time of the particle can be measured by subtracting the time of laser trigger signal from the time when the particle hits the detector.

The detection efficiency of the MCPs is typically estimated to be 50%, as half of the incident particles can not generate the secondary electrons or even do not hit in the channel. This detection efficiency means not all the coincidence events can be detected. In order to avoid the wrong coincidences, we have to ensure that one laser pulse or even several laser pulses should only lead to one ionization event. For example, the repetition rate of our laser is 3 kHz and the ionization count rate in our measurement is 1000 counts per second. That means there is one ionization event every three laser pulses. One way to decrease the ionization count rate is to decrease the intensity of the laser pulse. However, the laser intensity may not be changed in some measurements as the varying intensity changes the ionization mechanism (e.g. the Keldysh parameter, see Section 2.1) as well. The other way is to reduce the density of the gas target, which will be discussed in the next section.
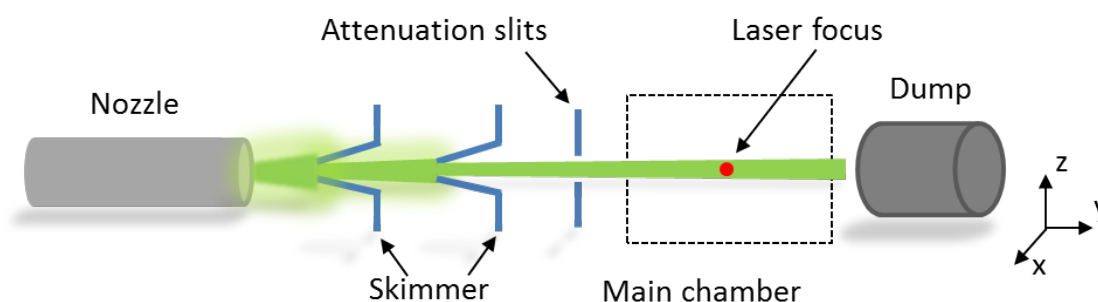
Figure 4.3: Schematic view of the gas jet. The gas is expanded through a nozzle with the diameter of 30 μm into the vacuum chamber. Two skimmers are used to further reduce the momentum spread of the gas targets.

4.1.2 The gas jet

The initial momentum spread of the gas target determines the momentum resolution. For instance, the momentum spread Δp for argon at the temperature $T = 300$ K is 19.6 a.u. This value is much larger than the ion momentum gained from the laser field, which is less than 1 a.u. for single ionization of Ar. In order to reduce the initial momentum as much as possible, a supersonic gas jet [Mil88] is designed such that the gas with a high pressure (a few bars) expands into a vacuum chamber through a 30-μm-diameter nozzle, as shown in Fig. 4.3. In this way, the temperature of the gas is efficiently cooled down to 1 K approximately and the momentum spread is thus decreased. Two skimmers are set at the entrance of two differentially pumped jet stage to block the gas targets with transverse momenta and further lower the gas pressure. In addition, the gas density can be adjusted by using two perpendicularly arranged attenuation slits. In the main chamber, the gas density can be decreased such that less than one gas atom or molecule appears in the laser focus. As mentioned in Section 4.1.1, reducing gas density gives rise the decrease of the ionization count rate, which benefits the coincidence measurement.

4.2 Data processing and analysis

All the delicate designs in the hardware of the REMI introduced in the last section ensure that the machine holds the high resolution for coincidence measurements. However, the raw data acquired by the detectors only contain the flight time and position information of the particles. Data processing and analysis including the momentum reconstruction and data calibration are thus necessary to interpret the data in an accurate way.

4.2.1 Momentum reconstruction

The momentum of a particle can be decomposed into two momentum components. One is along the direction of the laser polarization, called longitudinal momentum $p_\parallel$. The other is named transverse momentum $p_\perp$ which is perpendicular to the laser polarization. In
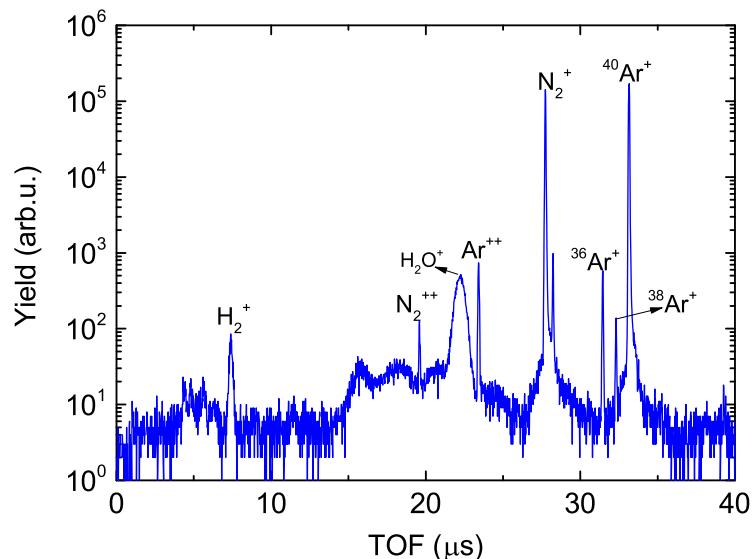
Figure 4.4: Time of flight (TOF) spectrum for ions generated by photo-ionization of Ar and N_2 by femtosecond laser pulses.

the experiment, we align the laser polarization along the spectrometer axis such that the longitudinal momentum is along the z-axis. The transverse momentum component can be further written as the composition of two orthogonal momenta p_x and p_y along the x and y axis respectively:

$$p_\perp = \sqrt{p_x^2 + p_y^2}.$$ (4.1)

The longitudinal momentum can be reconstructed by using the TOF information only. An example of the measured TOF spectrum (in logarithm scale) for the ionization of Ar and N_2 (see Section 5) by infrared laser pulses with the duration of 25 fs is shown in Fig. 4.4. Considering a charged particle with the initial longitudinal momentum $p_\parallel$, the TOF t is given by

$$t(p_\parallel) = m \left(\frac{2a}{\sqrt{p_\parallel^2 + 2qUm} + p_\parallel} + \frac{d}{\sqrt{p_\parallel^2 + 2qUm}} \right),$$ (4.2)

where m and q are the mass and charge of the particle, U is the acceleration voltage, a and d are the acceleration and drift length. From the above equation, the TOF is proportional to the square root of the mass-to-charge ration. Thus, different peaks of ions can be distinguished as marked in Fig. 4.4. In our measurement, there is no drift distance for ions ($d = 0$). The longitudinal momentum for ions can be solved by Equation 4.2

$$p_\parallel(t) = \frac{am}{t} - \frac{qU}{2a}t.$$ (4.3)

For electrons, the drift length is non-zero and the Equation 4.2 has no analytical solutions. The longitudinal momentum of an electron can be numerically calculated e.g. by Newton method [Sen09].

Reconstruction of the transverse momentum of electrons and ions requires the TOF as well as the position information. As mentioned in Section 4.1, a magnetic field is applied in the direction of the spectrometer axis to constrain and guide the electrons to the detector. This magnetic field does not change the TOF along the spectrometer axis and thus not affect the longitudinal momentum of the electrons. Now we consider an electron with the initial transverse momentum $p_\perp$ traveling in the magnetic field which has a field strength of B. One trajectory in the xy-plane is shown in Fig. 4.5. The radius R and the frequency ω of the electron cyclotron motion is given by

$$R = \frac{p_\perp}{qB}, \tag{4.4}$$

$$\omega = \frac{qB}{m}, \tag{4.5}$$

where q and m is the charge and mass of the electron. As described in Fig. 4.5, the angle ωt is a function of the TOF, which is measurable. The impact position (r, θ) of the electron is also known from the detector. With these parameters, the radius of the cyclotron trajectory can also be written as

$$R = \frac{r}{|2\sin(\omega t/2)|}. \tag{4.6}$$

Combining Equation 4.4, Equation 4.5 and Equation 4.6, the transverse momentum of the electron is expressed as

$$p_\perp = \frac{\omega m r}{|2\sin(\omega t/2)|}. \tag{4.7}$$

The angle of $p_\perp$ (emission angle) of the electron is given by

$$\phi = \theta - \frac{\omega t}{2} \mod(2\pi). \tag{4.8}$$

As the mass of ions is much larger than the one of electrons, the cyclotron frequency ω of ions is thus close to zero according to Equation 4.5. Therefore, the transverse momentum of ions $p_{\perp,ion}$ can be regarded as the limit of the electron momentum when $\omega \to 0$:

$$p_{\perp,ion} = \lim_{\omega \to 0} p_\perp = \frac{mr}{t}. \tag{4.9}$$

4.2.2   Data calibration

In this section we introduce the data calibration procedure by taking a measurement on the ionization of gas mixture Ar and N_2 as an example. From Equation 4.2 and Equation 4.7, we know that the momentum reconstruction requires the knowledge of experimental parameters e.g. the acceleration and the drift length, the extraction voltage, the magnetic field and so on. For different experiments, some of these parameters have to be adjusted to acquire the particles with interested energies. However, these parameters can be fluctuated during a single measurement and even small changes of these parameters may lead to a wrong momentum reconstruction. In order to retrieve the real momentum and ensure the accuracy of the data, data calibration is in high demand. Important calibration procedures are described as follows.
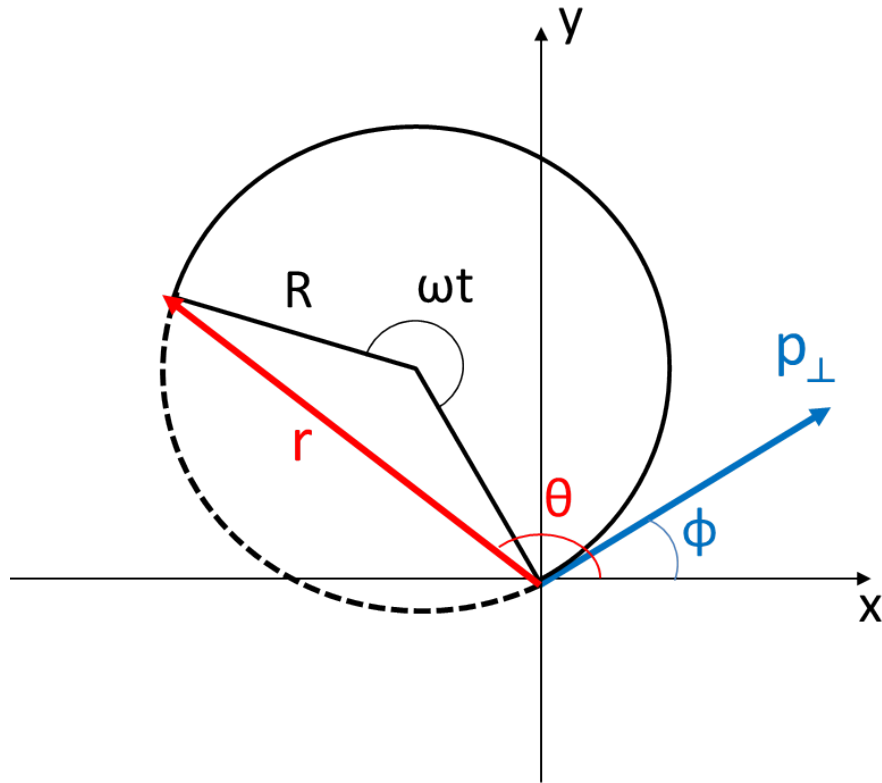
Figure 4.5:   Trajectory of an electron with the initial transverse momentum $p_\perp$ and emission angle ϕ in the *xy*-plane.
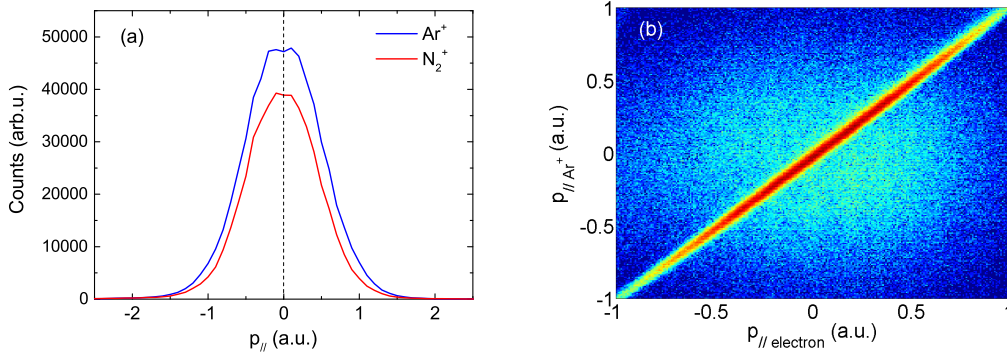
longitudinal momentum

Calibration of the longitudinal momentum of ions is the first step. As introduced in Section 4.2.1, the longitudinal momentum of ions can be calculated by using of the TOF (see the Fig. 4.4) only. According to Equation 4.3, the acceleration length, the voltage of the extraction field and the TOF can affect the longitudinal momentum. In the calibration process, the TOF is calibrated by introducing a time delay parameter because the initial laser trigger time may be shifted. Together with the time delay, the voltage should also be tuned such that the obtained momentum spectra for the interested ions are centered at zero. For instance, in the measurement of Ar and N_2, we compared the two single ionization channels:

$$\mathrm{Ar} \xrightarrow{IR} \mathrm{Ar}^+ + e^- \tag{4.10}$$

$$\mathrm{N_2} \xrightarrow{IR} \mathrm{N_2^+} + e^-. \tag{4.11}$$
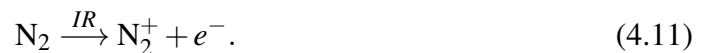
The calibrated longitudinal momentum spectra of Ar^+ and $\mathrm{N_2^+}$ are shown in Fig. 4.6 (a). Though the two species have different ionization yields, both longitudinal momentum $p_\parallel$ distributions are centered at zero momentum, indicating a good calibration.

Similar procedure happens on the electron longitudinal momentum calibration. Three variables, the acceleration voltage U, the drift length d and the electron's TOF t determine the longitudinal momentum of electrons. Since the drift length is fixed and the

Figure 4.6: (a) Calibrated longitudinal momenta of Ar^+ and N_2^+ distribution. (b) Coincidence spectrum as a function of the longitudinal momentum of Ar^+ and electrons.

acceleration voltage has been calibrated for ions, the electron TOF t is calibrated by introducing a time delay or even a linear calibration factor b (if needed). The calibrated TOF t' is given by

$$t' = bt + t_0 \, (b \approx 1) \tag{4.12}$$

Fig. 4.6 (b) shows the number of events as a function of the longitudinal momentum of Ar^+ and electrons. Note that the positive direction of the longitudinal momenta of ions and electrons are opposite in the calibration. Most events are distributed along the diagonal line in which the longitudinal momentum of Ar^+ and electrons have the same value, corresponding to the momentum conservation. That is due to that in the same event of single ionization, an Ar^+ ion and an free electron are generated with the same absolute value of momentum. The background points correspond to the events in which the ion and the electron are not released from the same Ar atom. The goal of the electron longitudinal momentum calibration is to shift or rotate the diagonal line by tuning the parameters (e.g. b and t_0) such that the coincidence events are symmetrically distributed along the line $p_{\parallel Ar^+} = p_{\parallel electron}$. The electrons in coincidence with the single ionization of N_2 can be extracted in the same way.

transverse momentum

The calibration on the transverse momentum requires the ion and electron impact positions on the detectors. Due to the gas jet, the ions on the detector are not focused at the centered. However, the ions from the background gas (e.g. water) can help us determine the center position. In this way, the velocity of the gas jet is calibrated. In order to calculate the transverse momentum correctly, the axis of the ion detector has to be rotated slightly to ensure that it is strictly along the y-axis.

In ideal cases, the cyclotron motion of an electron lead to the electron revisiting the spectrometer axis, i.e. $(0, 0)$ point on the detector plane every cyclotron period. However, in the measurement, the laser drift or the minor change of the magnetic field can affect the ideal trajectory. This deviation on the position can be compensated by using the following expression:

$$y(t) = at^2 + bt + c \tag{4.13}$$
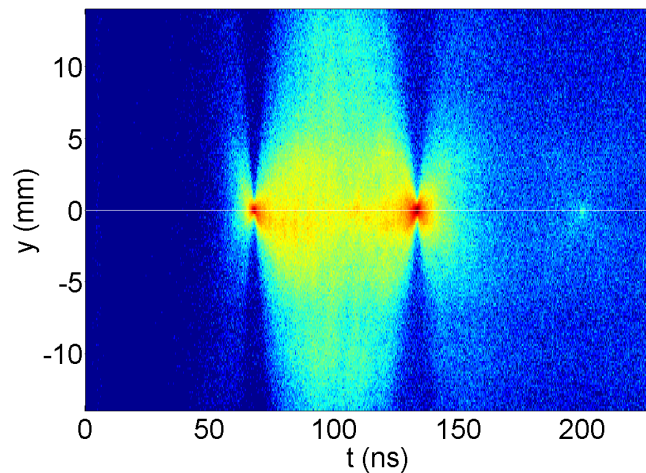
Figure 4.7: *y*-position of the electrons as a function of the TOF.

where $y(t)$ is the impact position of an electron in the *y*-axis as a function of the TOF of the electron. *a*, *b* and *c* are correction factors for the electron trajectory. Fig. 4.7 shows the cyclotron trajectory of electrons: the *y*-position of the electrons as a function of the TOF. The cyclotron period can be calibrated from the time nodes when electrons return to the spectrometer axis. For example, the electrons in Fig. 4.7 return at the TOF of 68 ns, 134 ns and 200 ns respectively. The cyclotron period is thus 66 ns. The correction factors are chosen such that all the nodes are set along the $y = 0$ axis, as shown in Fig. 4.7. Similarly, the *x*-position of electrons $x(t)$ has to be calibrated with the corresponding correction factors. After this calibration, the position distribution of electrons on the detector is symmetric around the point $(0,0)$, shown in Fig. 4.8. Thus, the well-calibrated transverse momentum distribution of electrons can be calculated from the calibrated TOF and position information.

As the longitudinal momenta of electrons in coincidence with Ar^+ or N_2^+ have already been derived from their TOF, the full momentum distribution of electrons can be finally reconstructed. For example, a momentum spectrum (logarithm scale) of electrons extracted from the single ionization of Ar by using 25 fs laser pulses with the central wavelength of 800 nm is shown in Fig. 4.9. At the longitudinal momenta -0.4 a.u. and 0.9 a.u. there are no resolutions for the transverse momentum. This is because these momenta correspond to the nodes of the TOF when the electrons return to the spectrometer axis. At these nodes, the transverse momentum cannot be reconstructed.

Further calibration

In the previous sections, the basic calibration procedures on the momentum reconstruction of interested particles have been described. With these calibrated momenta, further information e.g. energy spectra of ions or electrons can be retrieved for different ionization or dissociation channels. For some pump-probe experiments, the relative time delay between the two laser pulses has to be calibrated as well. These calibrated processes will be introduced in the measurements presented in Chapter 5 and Chapter 6.
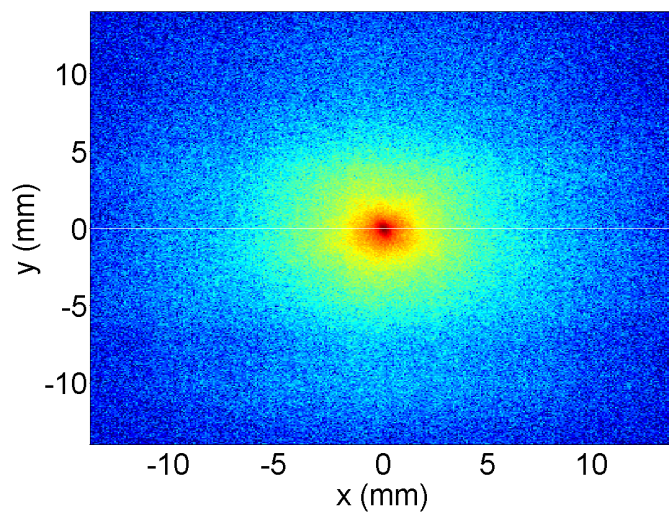
Figure 4.8: Position distribution of the electrons on the detector.
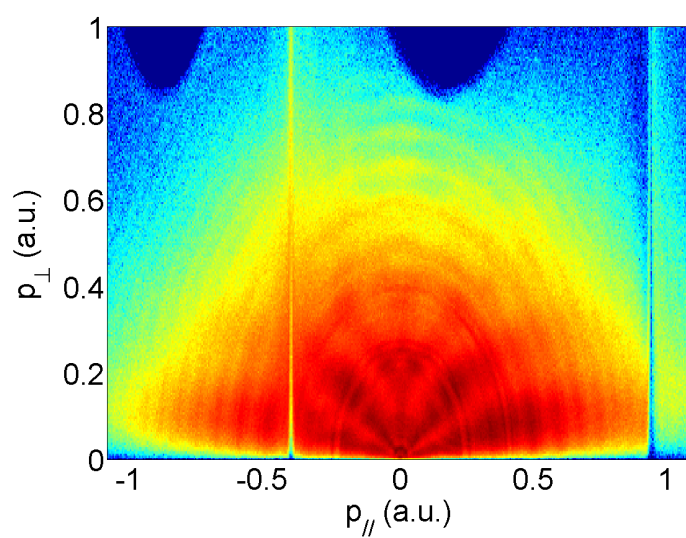
Figure 4.9: Full momentum distribution (logarithm scale) of electrons extracted from the single ionization of Ar.

Chapter 5

Phase-controllable ionization of Ar and N$_2$

Sculpted ultrashort laser pulses have been widely used in investigating the ultrafast dynamics in strong-field ionization of atoms and molecules. For instance, electronic wave packets can be controlled on attosecond time scales by using phase-tunable two-color laser pulses [XRK$^+$12]. The two-color laser pulses, which have been introduced in Section 3.4, provide an additional way in controlling the asymmetric electron or ion emission in the ionization process [ANT$^+$14, ALN$^+$15] in the absence of CEP-stabilized laser pulses.

In this chapter, we investigate strong-field ionization of Ar and N$_2$ by using two-color laser pulses and the Reaction Microscope. Using Ar and N$_2$ gas mixture in the same measurement, we are able to compare the results from Ar and N$_2$ under the same experimental condition. Moreover, the ionization potentials of Ar and N$_2$ (15.76 eV and 15.58 eV, respectively) are very close. As we know from Section 2.1, the ionization potential determines whether strong-field ionization occurs in the multi-photon ionization regime or the tunnel ionization regime in a given laser field and affects the ionization mechanism. This way, we ensure the atoms and molecules experience the same external conditions. If we observe any difference between the electrons emitted from Ar and N$_2$, these differences can be attributed to the different internal structures of atoms and molecules.

In the first section, the full momenta of photoelectrons and the energy spectra for single ionization of Ar and N$_2$ are presented. In the second section, we focus on the control of asymmetric electron emission for the two species. The asymmetry parameter, the phase calibration, the phase-dependent electron momentum, and the asymmetry analysis of the electrons are introduced in this section. In the end of this chapter, we quantitatively investigate the asymmetric emission of electrons from single ionization of Ar and N$_2$ by comparing their asymmetry parameters.
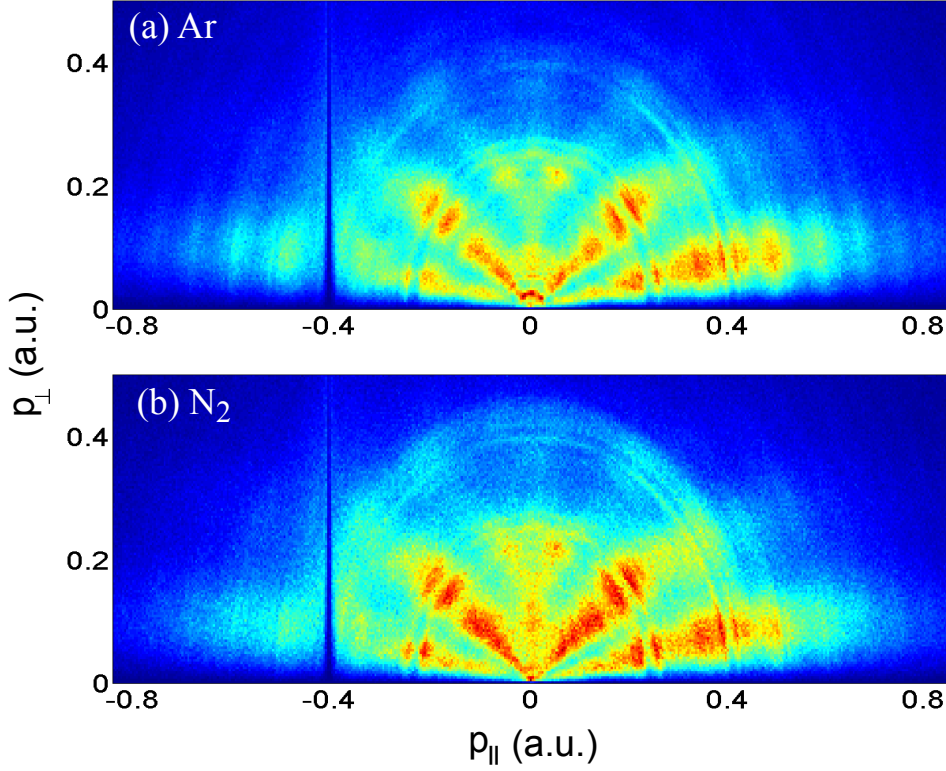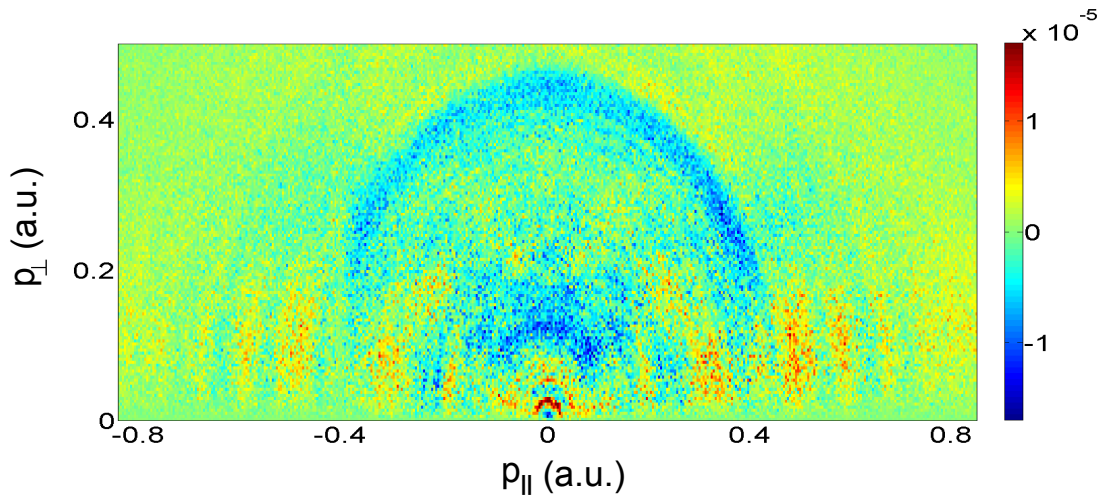
Figure 5.1: Electron momentum distribution measured in coincidence with (a) Ar$^+$ and (b) N$_2^+$. $p_\parallel$ is the momentum in the laser polarization direction and $p_\perp$ is the momentum in the transverse direction.

5.1 Photoelectron spectra

In this section, we show the experimental results measured by the REMI. With the help of the REMI, we are able to extract the electrons emitted in coincidence with their parent ions. The study of electrons gives us more information as the electron spectra have higher resolutions compared to the spectra of ions. Full three-dimensional (3D) momentum spectra and energy spectra of electrons from the two following single ionization channels are studied in this section:

$$Ar \xrightarrow{IR} Ar^+ + e^- \tag{5.1}$$

$$N_2 \xrightarrow{IR} N_2^+ + e^- \tag{5.2}$$

In the experiment, linearly polarized laser pulses with 25 fs duration at the central wavelength of 800 nm are generated by the Ti:Sapphire laser and used for second harmonic generation in the two-color interferometer (see Section 3.4.2 for details). The spatially and temporally overlapped fundamental-frequency laser pulse and its second harmonic are then focused into the REMI. The supersonic gas jet, a mixture of Ar and N$_2$, intersects with the laser beam in the center of the REMI. The intensity of the 800 nm and the 400 nm laser is estimated to be 10^{14} W/cm^2 and 5×10^{13} W/cm^2 respectively.

Figure 5.2: Difference in electron momentum distribution between Ar and N_2. Figure plotted by subtracting the normalized electron momentum of N_2 from the normalized electron momentum of Ar.

Calculated from the ionization potentials and the laser intensity, we know this experiment is at the border of multi-photon ionization and tunnel ionization as the corresponding Keldysh parameter is close to 1. However, even in the tunnel ionization region ($\gamma < 1$), the above threshold ionization (ATI) structures can be resolved [RZS$^+$04]. Fig. 5.1 shows the 3D momentum distribution of electrons emitted in coincidence with Ar$^+$ and N_2^+. Here, $p_\parallel$ is the momentum in the laser polarization direction and $p_\perp$ is the momentum in the transverse direction. For both spectra, there exist two distinct structures. One is the finger-like stripes starting from zero momentum, the other is the ring structure which is known as ATI rings. These patterns are the results of electron interferences in momentum space: The finger-like stripes are caused by the intracycle interferences from coherent superposition of electron trajectories emitted within a single laser cycle while the ATI rings are due to the interferences of electrons released in different cycles (intercycle interferences) [AIPB12, AIS$^+$10, XRK$^+$12]. The intercycle interferences are separated by the laser cycle in time, leading to the ATI rings separated by one photon energy $\hbar\omega$. Particularly, in the first ATI peak (around 0.3 a.u. in momentum spectrum), the ring structure splits into a few sharp rings. Similar fine structures appear also in the second ATI peak. These structures are attributed to Freeman resonances [FBM$^+$87, FB91], which has been introduced in Section 2.1.2. The excited states near the continuum of an atom or a molecule together with its ionization potential I_p are shifted in energy by approximately U_p (ponderomotive energy) in laser fields due to the AC Stark shift [FBM$^+$87]. Thus, these states can come into resonance with an integer number of photons, leading to enhanced ionizations from these states.

To study the difference in electron spectra between Ar and N_2 in detail, the momentum distribution (a) and (b) in Fig. 5.1 is firstly normalized to one. Then we subtract the normalized full electron momentum of N_2 from the normalized Ar electron momentum. In this way, we get the difference in electron momentum distribution between Ar and N_2, shown in Fig. 5.2. In this figure, red color means higher electron yield for Ar and blue color indicates more electrons detected for N_2. We can see that the difference mainly
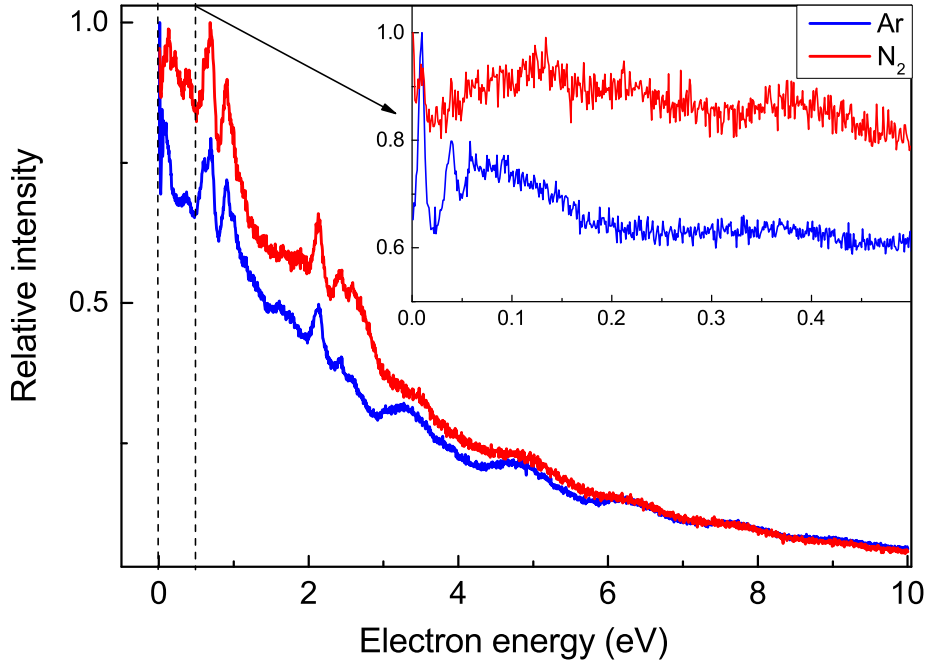
Figure 5.3: Photoelectron energy spectra for single ionization of Ar (blue curve) and N$_2$ (red curve). Each spectrum is normalized to its maximum value.

shows in the ring structures in momentum spectra. This can be explained by the above-mentioned Freeman resonances and the discrepancy in the excited states between Ar and N$_2$. For single ionization, the energy E of a photoelectron emitted from an excited state is given by

$$E = mh\nu - E_i \tag{5.3}$$

where E_i is the binding energy of the excited state in the laser field and m is the number of photon absorbed. It is known from Equation 5.3 that the position of the Freeman resonance is only dependent with the laser field (photon energy and laser intensity) and the excited states of atoms or molecules. In this experiment, Ar and N$_2$ experienced the same laser field. Therefore, it is the difference in the level of excited states between atoms and molecules that leads to the discrepancy in the 3D electron momentum spectra.

Furthermore, the energy spectra of the electrons emitted in coincidence with Ar$^+$ and N$_2^+$ are shown for comparison in Fig. 5.3. Both photoelectron energy spectra (PES) are normalized such that their maxima equal to one respectively. The Freeman resonances at around 1 eV and 2 eV are also reflected in the energy spectrum. A few ATI peaks appear as well in the high-energy region (more than 3 eV) for both Ar (in blue curve) and N$_2$ (in red curve). The two spectra have almost identical structures except for the region of first few hundreds meV. As shown in the enlarged region (0 to 0.5 eV) in the right upper panel in Fig. 5.3, the PES of Ar exhibits a striking peak at the near-zero energy region. At around 0.05 eV, the second sharp peak can be clearly resolved in the PES of Ar while the same structure is absent in the PES of N$_2$. These peaks, which correspond to the ring-like
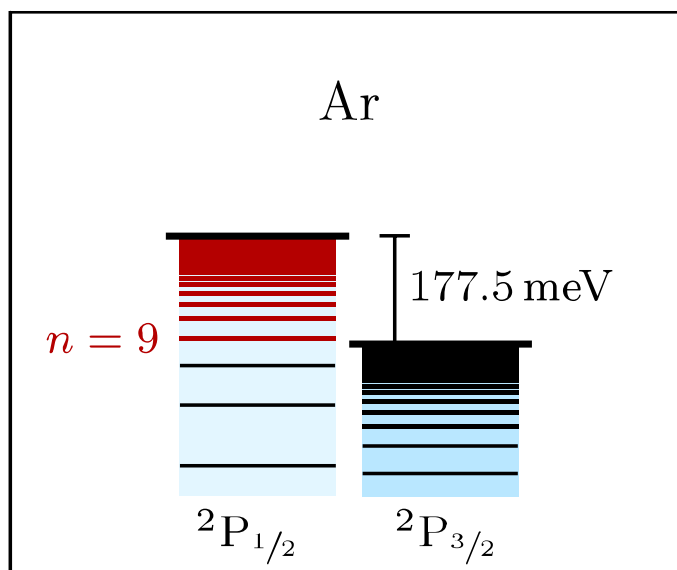
Figure 5.4: Doubly excited Rydberg states in argon. Figure taken from [Fec14].

structures in the full momentum distribution, can be seen in Fig. 5.1 (a). To understand these very-low energy structures in the PES of Ar, one needs to know the energy level and ionization mechanism of the Ar atom. As shown in Fig. 5.4, there exist two series of Rydberg states for Ar atoms: excited $^2P_{1/2}$ states and ground $^2P_{3/2}$ states, which have different ionization potentials. In the first step, the high-lying Rydberg states approaching the $^2P_{1/2}$ continuum, which are dubbed as doubly excited states (DES), can be populated with the excitation of the laser pulses. Note that the lifetime of these DES is much longer than the pulse duration, which means these states can survive in the laser field. Because some populated states lie above the $^2P_{3/2}$ continuum, an autoionization process can occur, leading to the generation of the low-energy electrons [FCK$^+$15]. Details on the population of the DES and the autoionization of noble gas atoms can be found in [Fec14].

In the PES of N$_2$, several small peaks in the range of 0 - 0.5 eV can also be resolved, though they are not as pronounced as for the case of Ar. Compared with the PES of Ar, one can see that there is an enhancement in the yield of photoelectrons in the low energy region. The interpretation of this enhancement will be discussed in Chapter 6.

5.2   Control of asymmetric electron emission

Controlling electronic dynamics is a premise of ultimately controlling a chemical reaction. The fast-developing intense ultrashort laser technique [BK00] is considered as a promising tool. For instance, the CEP-stabilized laser has been used for localization of electrons [KSV$^+$06] and controlling the electronic process on attosecond timescales [BUU$^+$03]. Recently, the sculpted laser fields (e.g. two-color laser fields) have made the control of electronic wave packet dynamics possible [XRK$^+$12]. Compared with the few-cycle laser pulses, the sculpted laser pulses do not require the use of hollow fiber to further compress the pulses.

As introduced in the previous section, with the REMI, we are able to realize ion-electron coincidence measurements which allow us to investigate electrons released from different ionization channels. Besides this advantage in our experiment, the use of two-color laser fields also provides a tool to control the electron emission in the strong-field ionization of atoms and molecules. The idea described in the following sections is that the superposition of the fundamental laser pulse and its second harmonic allows to shape the electric field from symmetric to asymmetric. This symmetry (or asymmetry) is then imprinted in the electron emission direction in the ionization process. We can thus use this principle to control the asymmetric electron or ion emission and study the ionization dynamics by changing the time delay between the two-color laser pulses.

5.2.1   Asymmetry parameter

In order to calibrate the phase and quantitatively describe the asymmetric emission of the photoelectrons, we define an asymmetry parameter as a function of the relative phase by the following equation:

$$A(\phi) = \frac{N_+(\phi) - N_-(\phi)}{N_+(\phi) + N_-(\phi)} \tag{5.4}$$

where $N_+(\phi)$ and $N_-(\phi)$ represent the number of electrons emitted in the direction of positive and negative longitudinal momentum respectively at the phase of ϕ. Fig. 5.5 shows the asymmetry parameter of the electrons from single ionization of Ar as a function of the relative phase between the two-color pulses. The blue dots with error bars denote the asymmetry value at each phase. These data points are fitted by a sinusoidal function

$$A(\phi) = A_0 \sin(\phi + \phi_0) \tag{5.5}$$

with A_0 the amplitude of the asymmetry and ϕ_0 the phase offset, shown in red curve in Fig. 5.5. We see the absolute value of the asymmetry parameter for the electrons emitted in coincidence with Ar$^+$ varies from 0 to 0.15 when the relative phase increases from 0 to 2π.

Note that the above-mentioned asymmetry parameter is considering the electrons with all kinetic energies. In fact, the electron with different energies originates from different mechanisms. For example, low-energy electrons are normally from the above threshold ionization while the high-energy electrons come from the rescattering process. To investigate the asymmetric electron emission from different processes, we define a two-dimensional asymmetry parameter as a function of the relative phase ϕ and the electron energy E_e as follows:

$$A(E_e, \phi) = \frac{N_+(E_e, \phi) - N_-(E_e, \phi)}{N_+(E_e, \phi) + N_-(E_e, \phi)}. \tag{5.6}$$

$N_+(E_e, \phi)$ and $N_-(E_e, \phi)$ represent the number of electrons at the energy E_e emitted with positive and negative longitudinal momentum at the phase of ϕ. Again, we use the electrons from single ionization of Ar as an example and plot the asymmetry pattern as a function of ϕ and E_e, shown in Fig. 5.6.

As can be seen in this figure, the electrons with energy larger than 2 eV have more asymmetries though these electrons have much less counts than the low-energy electrons. In
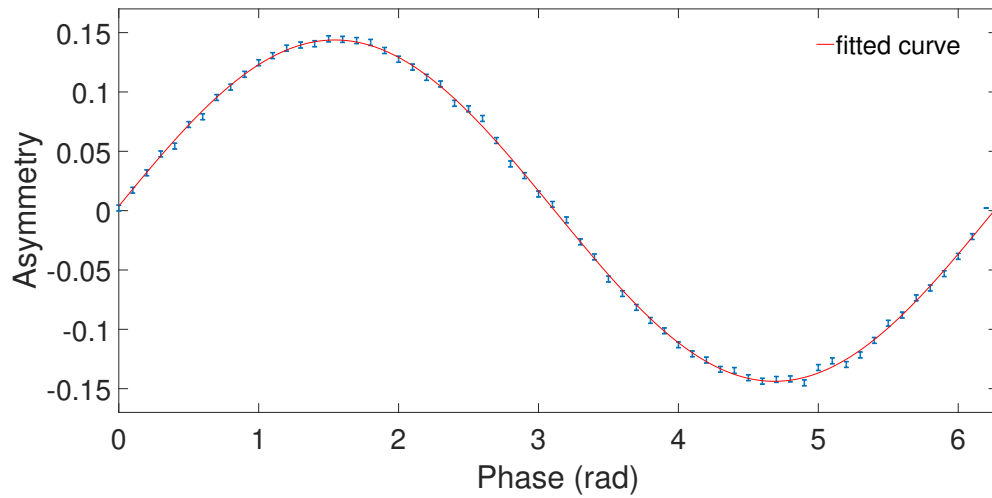
Figure 5.5: Asymmetry of the electrons from single ionization of Ar as a function of the relative phase between the two-color pulses.
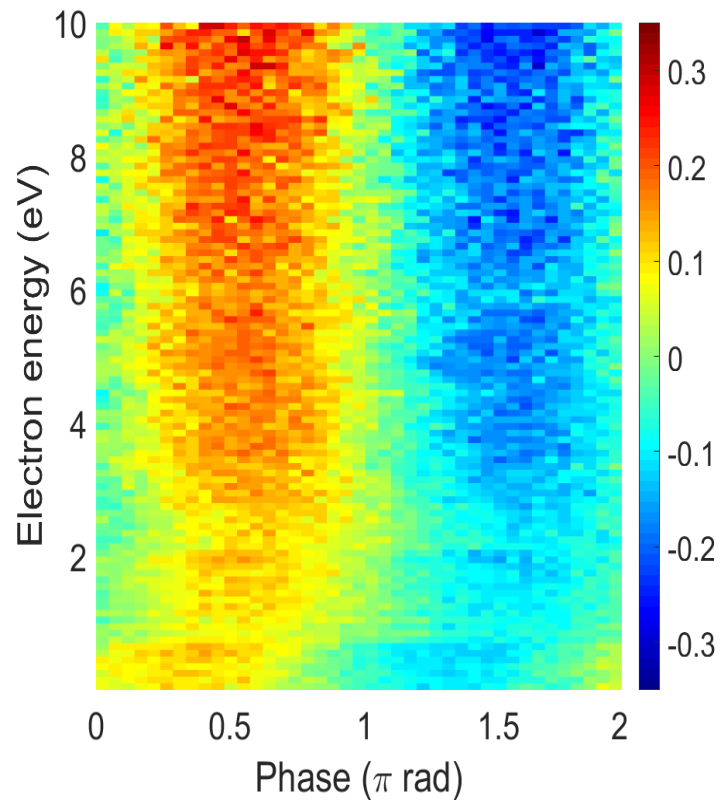
Figure 5.6: Asymmetry of the electrons from single ionization of Ar as a function of the electron energy and the relative phase between the two-color pulses.
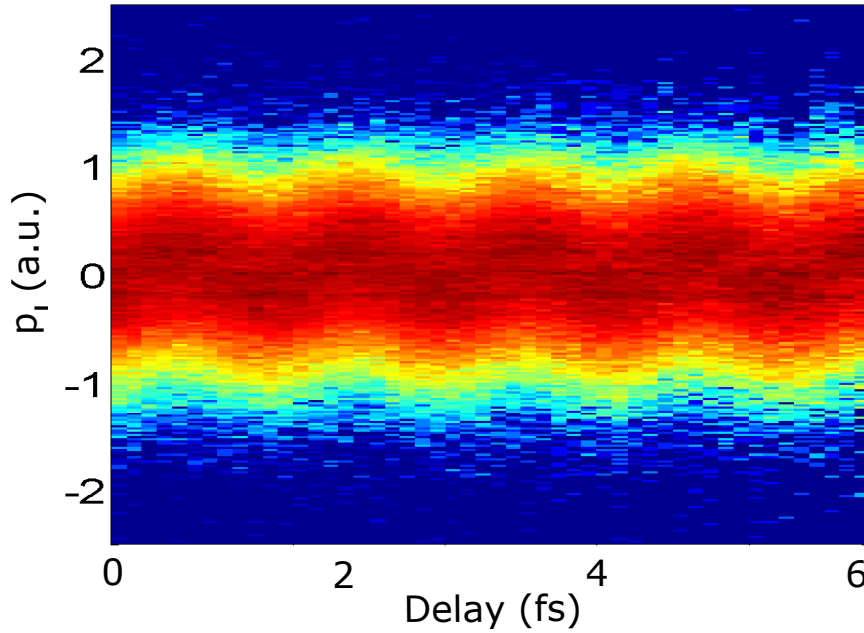
Figure 5.7: Longitudinal momentum of the electron in coincidence with Ar^+ as a function of the relative time delay between the two-color pulses.

the low-energy region, the asymmetry of electrons exhibits a tilted stripe. That means the asymmetry of the low-energy electrons is energy dependent. Detailed analysis on the energy-dependent asymmetry parameter will be discussed in Section 5.3.

5.2.2 Phase calibration

Good resolution of an experiment requires large statistics, which means longer time measurement in our case. This thus requires the stability of the laser system lasts for a long time (normally more than 24 hours). The laser is able to run several days with the oscillator being in the mode-lock status. However, the beam drift is inevitable. As the laser has to pass several meters before reaching a target, a small drift can lead to a significant change at the target. Also, the drift of the piezo stage in the Mach-Zehnder interferometer (see Section 3.4.2) gives rise to the errors in the relative time delay between the two-color pulses. In order to reduce the experimental errors as much as possible, we need to calibrate the phase for each data file. Afterwards we add up all the calibrated data files for analysis.

Phase calibration is performed after normal calibration of raw data acquired from the REMI (see Chapter 4). Each calibrated data file contains full information of e.g. the longitudinal momentum p_l, the transverse momenta p_x, p_y of electrons and and their coincident ions. In addition, the position of the delay stage in the Mach-Zehnder interferometer, with which we calculate the relative time delay between the two-color pulses, is recorded for every event.

The longitudinal momentum of electrons from single ionization of Ar is plotted with the time delay between the 800 nm and 400 nm laser pulses, shown in Fig. 5.7. In this figure,
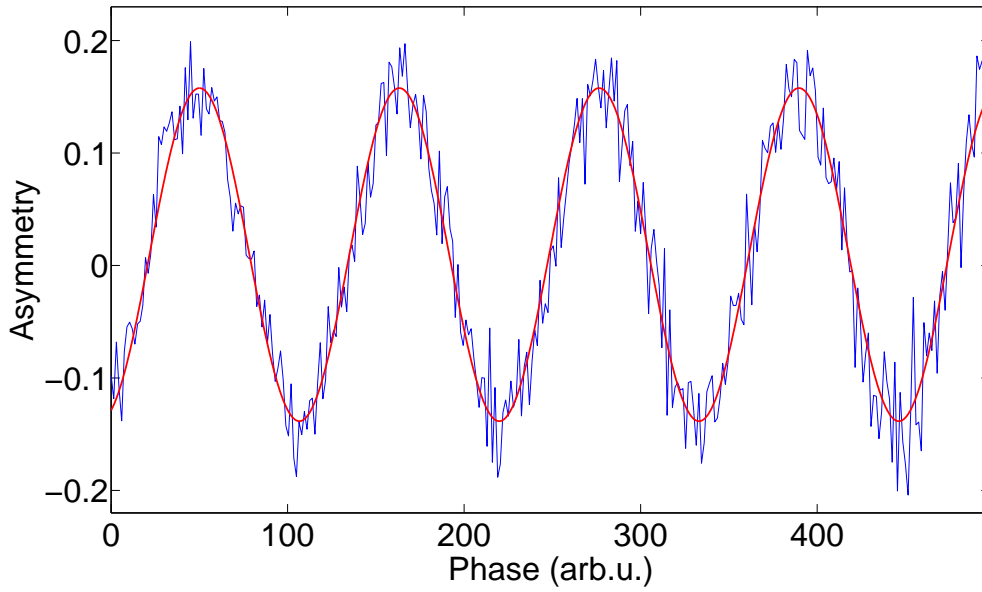
Figure 5.8:   Asymmetry parameter as a function of the relative phase between the two-color pulses.

the influence of the 400 nm laser pulse on the longitudinal momentum of the electrons is clearly imprinted on the oscillation pattern. Note that this figure shows only one data file, which takes approximately 45 minutes to be recorded with scanning the delay stage back and forth. This scan changes the time delay between the blue (400 nm) and red (800 nm) laser pulses up to 6 fs (corresponding to 4.5 optical cycles of the blue laser field) with the time resolution of 80 attoseconds. As mentioned before, the laser drift and the instability of the Mach-Zehnder interferometer bring errors on the measurement. These drifts also continuously make the oscillation shown in Fig. 5.7 different from file to file, weakening the phase-dependent asymmetry structure.

The main process of the phase calibration is converting the time delay to the relative phase between the two-color fields and then tagging every event from different optical cycles a specific phase from 0 to 2π according to the sin-like oscillation in the longitudinal momentum (shown in Fig. 5.7). In detail, we plot the asymmetry parameter A (see Section 5.2.1) as a function of the phase ϕ which is proportional to the delay between the two-color fields (Fig. 5.8). By fitting this asymmetry parameter with the following function:

$$A = a + b\sin(c\phi + d) \tag{5.7}$$

with a, b, c and d the fitting parameters, we map the phases from different cycles into one cycle from 0 to 2π. Afterwards we add up all the events from the calibrated data and obtain a total data file containing the full momentum information of particles and their corresponding relative phases. As an example of the phase calibration, the longitudinal momentum of electrons which are singly ionized from Ar as a function of the calibrated relative phase between red and blue laser pulses is shown in Fig. 5.9. In the whole data analysis, the relationship between time delay and phase, which is calibrated from single ionization of Ar, serves as a reference for all the other channels (e.g. single ionization of
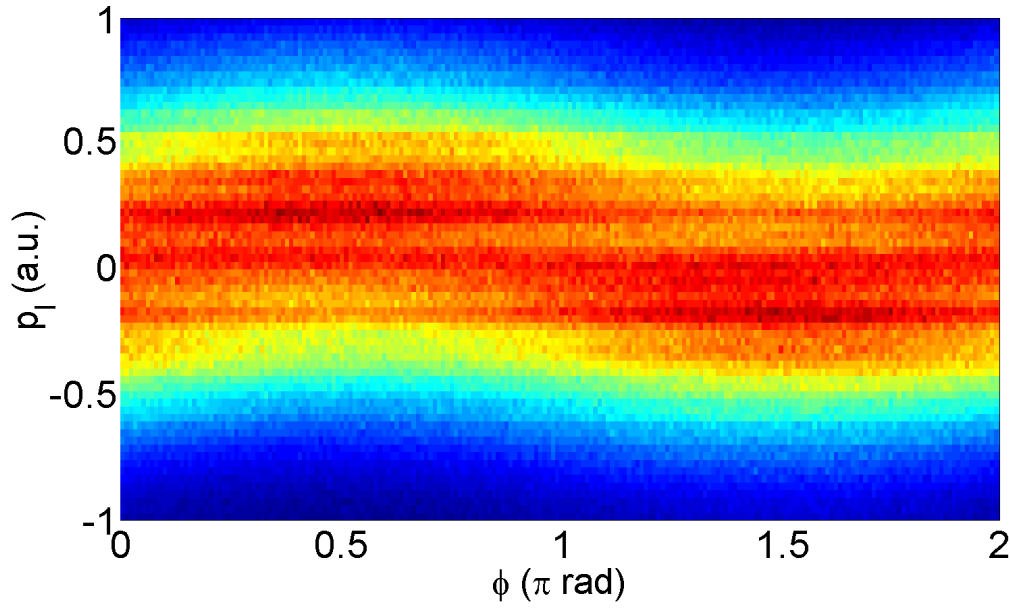
Figure 5.9: Longitudinal momentum of the electron in coincidence with Ar^+ as a function of the relative phase from 0 to 2π between the two-color fields.

N_2 or double ionization of Ar and N_2). This way, the ion/electron dynamics for different ionization channels can be compared under the unique relative phase between the two-color fields.

5.2.3 Phase-dependent electron momentum

As discussed in previous sections, the relative phase ϕ between the two-color fields plays a key role in controlling the shape of the electric field and the asymmetric emission of electrons or ions. The electron momentum distribution provides a detailed information on the strong-field ionization process. For example, the interference patterns of electrons and the signature of the Freeman resonance can be seen with high resolutions in the momentum distributions for Ar and N_2 (see Fig. 5.1). However, the dynamics of the electrons cannot be resolved due to the lack of phase information.

According to the phase calibration procedure, we know that every calibrated data files contains the full momentum information of the coincident particles together with the relative phase between the two-color fields. That means every data point in the momentum spectra is dependent with the phase. Therefore, we plot the phase-dependent 3D momentum distributions for the electrons from single ionizations of Ar and N_2 when the relative phases are 0.25π [(a) and (e)], 0.75π [(b) and (f)], 1.25π [(c) and (g)], 1.75π [(d) and (h)], shown in Fig. 5.10.

These phase-dependent electron momentum spectra prove that the electron distributions are strongly modulated with ϕ for both Ar and N_2. As the phase changes by π, the finger-like stripes are shifted from the negative longitudinal momentum region to the positive longitudinal region for both cases. As one optical cycle of 400 nm lsaer pulse is only 1.3 fs, the time-resolved asymmetry patterns confirm that the two-color laser pulses can be
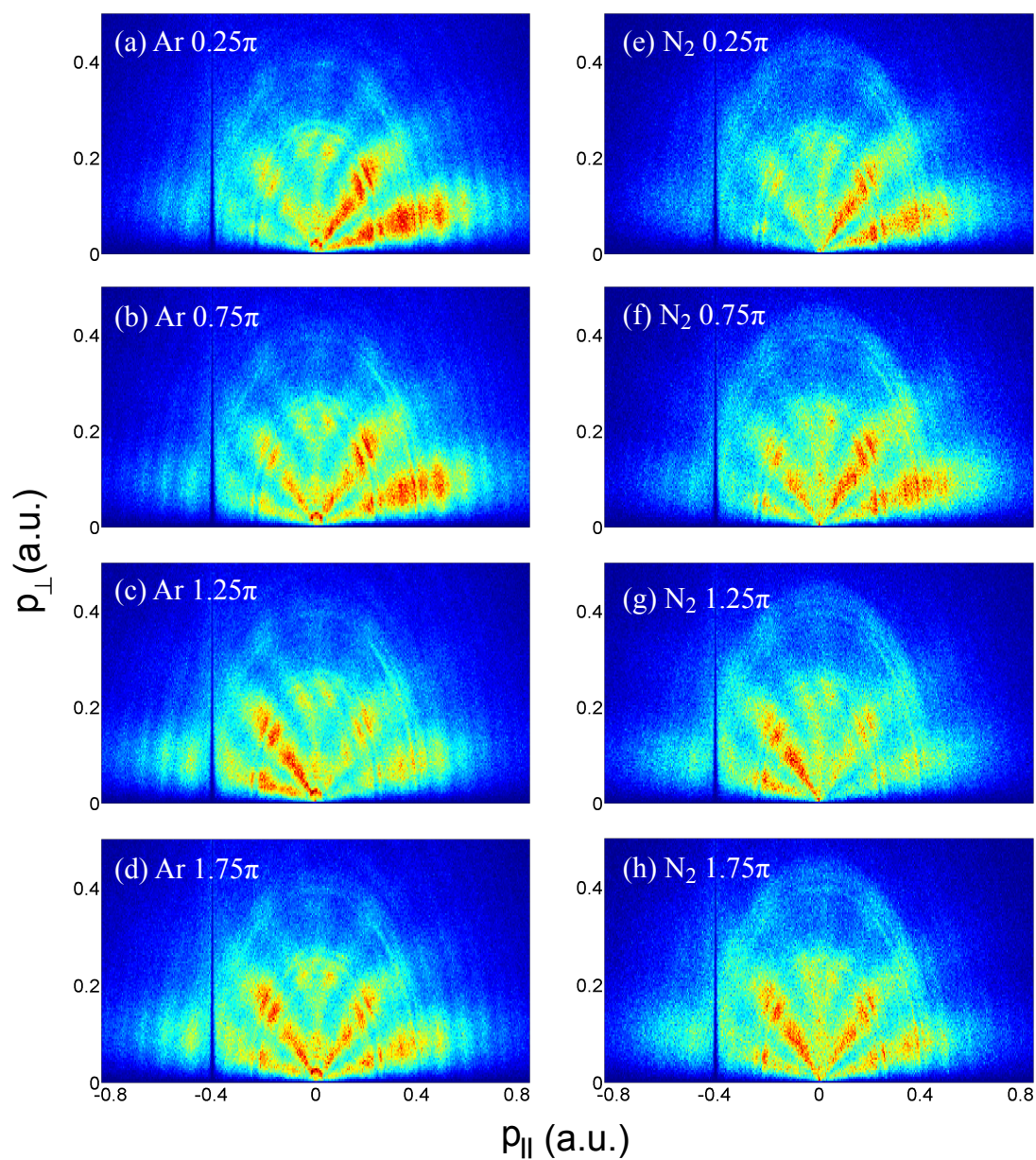
Figure 5.10:   Electron momentum distributions for ionization of Ar and N_2 at different relative phases between the two-color field: (a) and (e) 0.25π, (b) and (f) 0.75π, (c) and (g) 1.25π, (d) and (h) 1.75π.
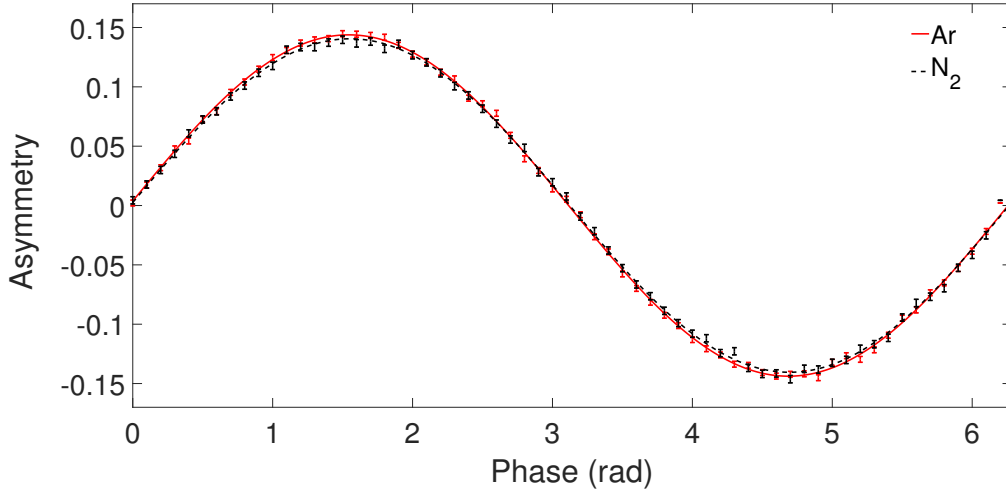
Figure 5.11: Asymmetries of the electrons from single ionization of Ar (red solid curve) and N$_2$ (black dashed curve) as a function of the relative phase between the two-color pulses.

served as a precise tool to control the ultrafast dynamics with attosecond time resolution in the absence of attosecond pulses.

5.3 Comparison

In this section we quantitatively investigate the asymmetric emission of electrons emitted from single ionization of Ar and N$_2$ by comparing their asymmetry parameters. Fig. 5.11 shows the value of the asymmetry parameter $A(\phi)$ at each phase for Ar-coincident (red dot) and N$_2$-coincident (black dot) electrons, together with their fitted curves (Ar in red and N$_2$ in black). We see the two asymmetry curves almost overlap with each other. That indicates the two electrons feel similar asymmetric force in the laser field. Then, we compare the energy-dependent asymmetry parameter $A(E_e, \phi)$ for the two electrons with energies up to 10 eV. As shown in Fig. 5.12, the electrons in coincidence with Ar and N$_2$ exhibit very similar asymmetry patterns in the low-energy region (0 - 2 eV). However, in the high-energy (2 - 10 eV) region, the asymmetry for Ar electrons shows no energy dependence (vertical stripes) while the asymmetry for N$_2$ electrons in this part is still dependent on the energy (tilted strips). That means there exists a phase shift in the asymmetric emission of high-energy electrons between Ar and N$_2$.

To further analyze the asymmetric electron emission at different energies, inspired by Equation 5.5, we fit the asymmetry parameter $A(E_e, \phi)$ with the following sinusoidal function:

$$A(\phi, E_e) = A_0(E_e)\sin(\phi + \phi_0(E_e)), \tag{5.8}$$

where $A_0(E_e)$ and $\phi_0(E_e)$ represent the amplitude and the phase of the asymmetry. $A_0(E_e)$ and $\phi_0(E_e)$ as a function of electron energy up to 10 eV are plotted in Fig. 5.13 (a) and (b) respectively. For both electrons in coincidence with Ar and N$_2$, the amplitude of the asymmetry increase with the electron energy. Meanwhile, both amplitude and phase os-
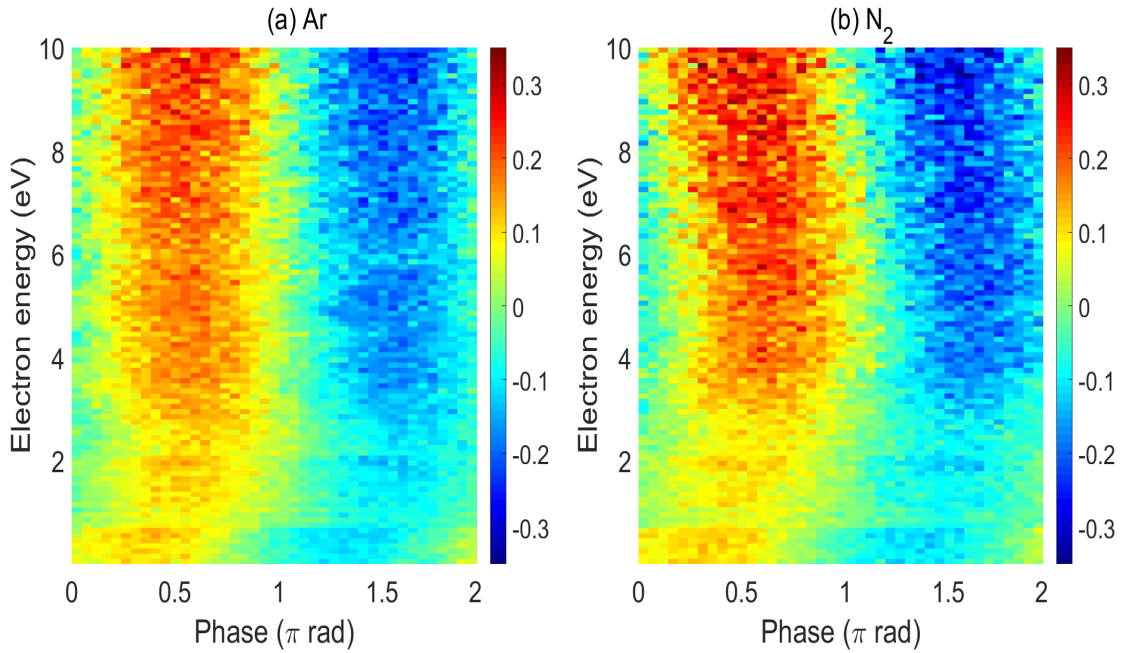
Figure 5.12: Electron asymmetry for single ionization of (a) Ar and (b) N_2 as a function of the electron energy and the relative phase between the two-color pulses.

cillate at some energies. The distance between these small peaks in Fig 5.13 (a) and (b) is approximately 1.55 eV, which is exactly the photon energy of 800 nm laser pulses. The results indicate the peaks are related to ATI (see Section 2.1.2). For comparison, the PES for Ar and N_2 are plotted in Fig. 5.13 (c). The black dashed lines in the figure denote the positions of a few ATI peaks from Ar. We see the oscillations in amplitude and phase spectra [Fig. 5.13 (a) and (b)] synchronize with ATI peaks for both Ar and N_2. This might be attributed to the quantum interferences between different multi-photon pathways which has been described in [APJ$^+$09]. For the electrons with energy less than 1 eV, neither the amplitude nor the phase of the asymmetry displays any significant differences between the two electrons (in coincidence with Ar and N_2). However, clear differences in both amplitude and phase spectra are observed in high-energy region. Although it is challenging to interpret the amplitude and phase shifts in asymmetric electron emission between single ionization of Ar and N_2, this measurement reveals the interference phenomenon that occurs differently for the atomic and the molecular case. The two-color method provides an additional way to distinguish and understand the dynamics of electrons emitted from different ionization pathways.
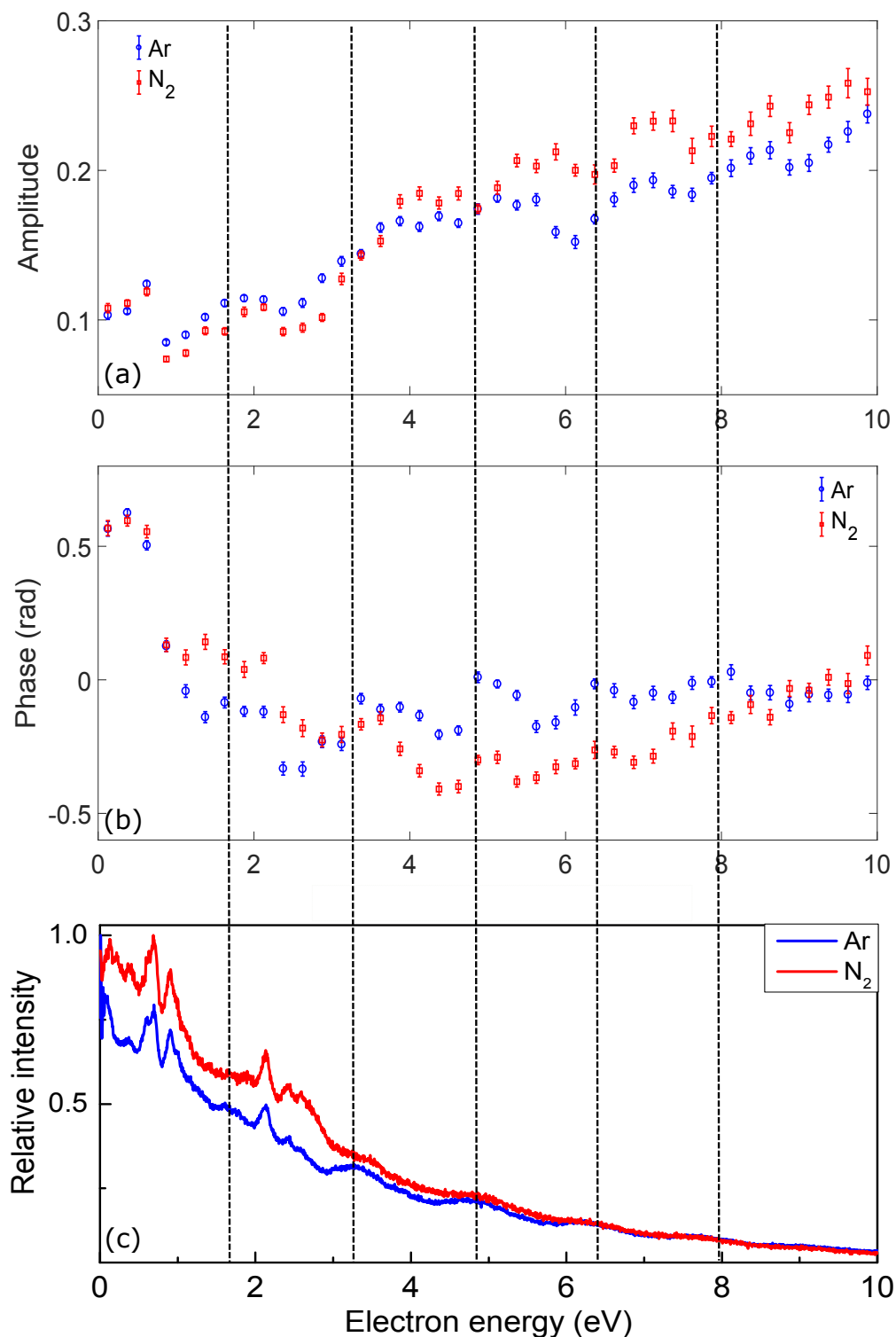
Figure 5.13:   (a) Amplitude and (b) phase offset of the electron asymmetry as a function of electron energy for single ionization of Ar (blue dot) and (b) N$_2$ (red square). (c) Photoelectron energy spectra (PES) for Ar and N$_2$ for comparison. The dashed lines denote the positions of the ATI peaks of the Ar PES.

Chapter 6

Electron-nuclear coupling of H_2 through autoionizing states

In the previous chapter, single ionization of Ar and N_2 gas mixture is investigated by using 25 fs two-color (800 nm + 400 nm) laser pulses. The photoelectron energy spectra (PES) exhibit different structures for Ar and N_2, especially in the low-energy region. Asymmetric electron emission was controlled by tuning the relative phase between the two-color fields. This phase-dependent asymmetry of electrons provides an additional tool for further comparison of electronic wavepacket dynamics between different ionization channels when the differences cannot be distinguished in the PES.

After the observation of the difference in electron emission between atoms and molecules (Ar and N_2) with similar ionization potentials, a similar question arises as to whether the electrons from different ionization pathways in a single molecule possess different properties in the same laser field. For instance, an electron is released from single ionization of a molecule no matter whether the molecule finally dissociate or not. In order to distinguish and compare the electrons from dissociative or non-dissociative pathways, the coincidence detection technique introduced in Chapter 4 is required.

H_2 molecules, as the most fundamental molecules, the ultrafast dynamics of which have been widely investigated with the development of the CEP-stabilized laser [PGW$^+$01, BUU$^+$03]. For example, the localization of electrons and control of asymmetric emission of ions has been realized in the laser-induced dissociation of H_2 or D_2 molecules [KSV$^+$06, KFF$^+$09, MFH$^+$07, SKPT$^+$10, FSC$^+$13]. To compare the wavepacket dynamics for different ionization channels, numbers of studies focused on the ions generated after strong field ionization of molecules [Pos04]. However, the ions only cannot provide sufficient information to characterize the pathway. One way to gain more information is to consider in addition the electron [dJFZ$^+$04, HIY$^+$09, BMG$^+$12, ZLL$^+$16], which also requires the ion-electron coincidence detection.

In this chapter we experimentally investigate the channel-selective electron emission from strong-field ionization of H_2 molecules [MCF$^+$17]. By using the ReMi, the electron momenta and PES in coincidence with bound and dissociative ionization channels are extracted and compared. Surprisingly, an enhancement of the photoelectron yield in the low-energy region is observed only for the bound ionization channel. This phenomenon

is interpreted as the population of the autoionizing states of H_2 molecules and the sequentially occurred vibrational autoionization process. Further investigation with two-color laser fields confirms that the low-energy electrons stem from different ionization pathways and the traditional two-step mechanism for describing the dissociation of H_2 molecules is not complete.

In Section 6.1, different ionization channels of H_2 molecules are introduced. These channels can be experimentally characterized by the ion TOF spectra. Section 6.2 presents the experimental results on the electron momenta and the PES for different channels. In Section 6.3, the experimental results are interpreted by a vibrational autoionization mechanism in which nuclei and electrons are coupled by transferring the vibrational energy of molecules to electronic energy. Finally, the measurement with two-color laser pulses is presented in Section 6.4 to confirm the conclusion.

6.1   Different ionization channels

When a H_2 molecule is exposed to a strong laser field, the following ionization pathways may occur:

$$H_2 \xrightarrow{IR} H_2^+ + e^- \tag{6.1}$$

$$H_2 \xrightarrow{IR} H^+ + H + e^- \tag{6.2}$$

$$H_2 \xrightarrow{IR} 2H^+ + 2e^- \tag{6.3}$$

The first channel is molecular bound ionization without fragmentation, where one electron is ionized by the laser field and the system ends up as a bound molecular H_2^+ ion together with a free electron. In the following this channel is named bound ionization. The second channel is called dissociative ionization, in which the molecule breaks up into a proton, a hydrogen atom and a free electron. In the third channel, double ionization occurs and two electrons are freed. The two protons thus repel each other with high energies giving rise to the molecule dissociation. This process is known as Coulomb explosion (CE). For our laser intensity (10^{14} W/cm^2), the predominant process is the bound ionization. The probability of the molecule dissociation can be raised with an increasing laser intensity.

In order to extract the electrons from different ionization channels, the coincident ions need to be distinguished. Fig. 6.1 shows the ion TOF spectrum obtained by ionization of H_2 molecules with 800 nm laser pulses. In the spectrum, the highest peak at the TOF of 8000 ns correspond to the H_2^+ produced in the bound ionization channel. This channel is liable to be extracted as the emitted molecular ion H_2^+ and the electron fulfill the momentum conservation. However, for the dissociative ionization channel, the emitted H atom cannot be detected by the MCP detector. The momentum conservation is not valid for the detected H^+ and the electron. In this case, we apply a condition that at the same event only one ion and one electron are detected. This way, we ensure the detected electrons are emitted in coincidence with the H^+ released from the dissociative ionization channel. As shown in Fig. 6.1, the zero momentum of H^+ corresponds to the TOF of 5700 ns (marked by a dashed line). Four inner peaks distributed symmetrically around the center correspond to the dissociative ionization while the two outer peaks are attributed to the CE
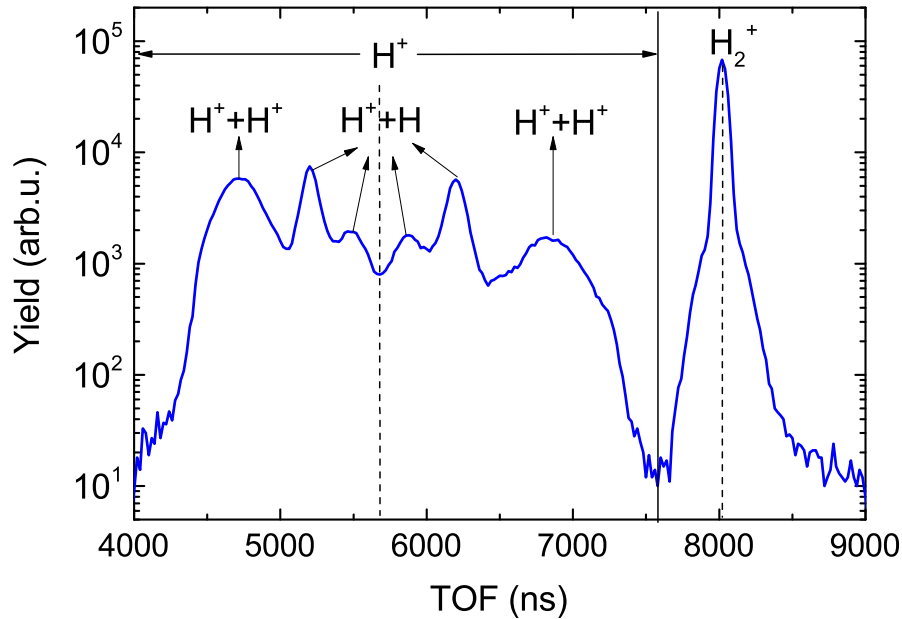
Figure 6.1: Measured ion TOF spectrum obtained by ionization of H_2 with 25 fs, 800 nm laser pulses. The TOF 5700 ns and 8000 ns correspond to the center of H^+ and H_2^+ peaks. The four peaks close to the dashed line originate from the dissociative ionization process while the two outer peaks correspond to the Coulomb explosion.

channel. To characterize the dissociative ionization channel in momentum space, the 2D momentum ($p_\parallel$ and p_x) of H^+ is obtained by using the calibration procedures introduced in Chapter 4, shown in Fig. 6.2. We see that the longitudinal momentum of the H^+ from the dissociative ionization is distributed between -10 a.u. and 10 a.u. The H^+ associated with the CE process exhibits a broad longitudinal momentum distribution up to ± 25 a.u. as the molecule gains more energies from the laser field and is excited to a higher potential energy curve. More counts are detected in the positive momentum region. This is due to the non-uniform detection efficiency for the particles emitted initially towards (positive momenta) or away from (negative momenta) the detectors.

The CE process involves two electrons and two protons and the mechanism is more complicated than the single ionization. In this thesis we compare the electrons generated from the single ionization and thus only focus on the bound and dissociative ionization channels. Details (e.g. momentum spectra) of electron momentum distribution extracted from the CE channel can be found in [Fec14].

As introduced in Section 2.2, the Born-Oppenheimer approximation in which electrons of a molecule are considered separated from its nuclei is widely used in theoretical modeling of molecules. For H_2 molecules, this approximation gives rise to a generally accepted two-step mechanism for dissociation of molecules by strong laser fields [KSV$^+$06]. As shown in Fig. 6.3, the molecule is singly ionized by the laser field with emission of a photoelectron. Then the molecule dissociates as the vibrational wavepacket is excited from the bound $1s\sigma_g$ state (red curve) to the repulsive $2p\sigma_u$ state (blue curve) in most
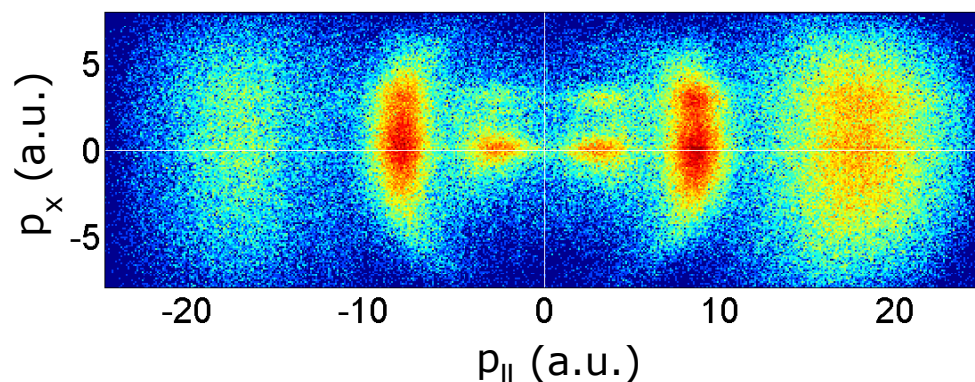
Figure 6.2: Measured 2D momentum ($p_\parallel$ and p_x) distribution for H$^+$. Dissociative ionization ($|p_\parallel| < 10\,a.u.$) and coulomb explosion ($15\,a.u. < |p_\parallel| < 25\,a.u.$) processes
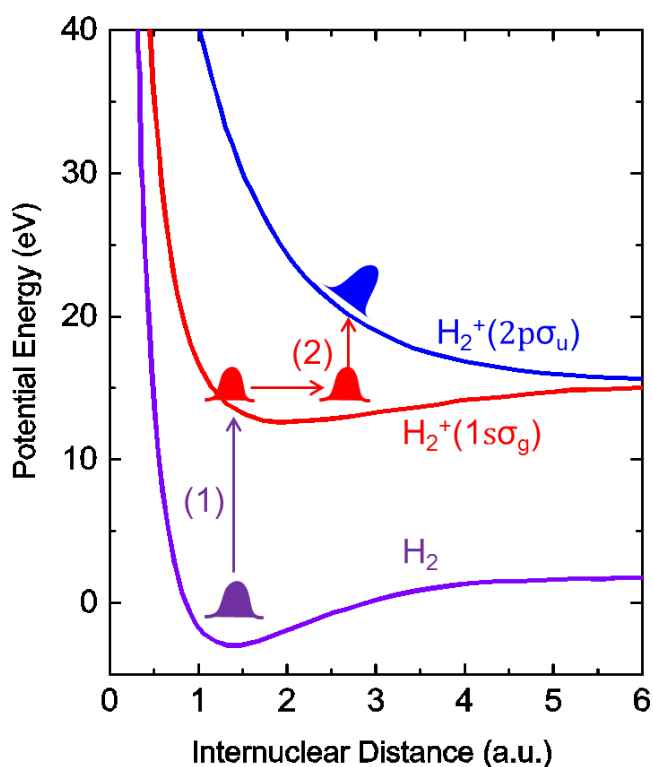
Figure 6.3: Potential energy curves for H$_2$ ground state (violet curve), H$_2^+$ bound state (red curve) and H$_2^+$ repulsive state (blue curve). The main dissociation process is described by a two-step mechanism [shown in (1) and (2)]: the molecule is firstly ionized by the laser field. A vibrational wavepacket is triggered in the $1s\sigma_g$ state and then excited to the repulsive $2p\sigma_u$ state.

cases. As the molecule dissociates after the electron emission, the second step is independent of the first step. Thus, on first approximation, the electrons in coincidence with the bound and dissociative ionization channels should be the same. However, in our measurement, a clear difference was observed in the electron momentum and energy spectra in the low-energy region. These results and interpretations are present in Section 6.2 and Section 6.3.

6.2 Channel-selective electron emission

As discussed in the previous section 6.1, electrons from different ionization channels can be extracted by the ion-electron coincidence technique. In this section, we present experimental results on channel-selective electron emission from strong field ionization of H_2 molecules, which are achieved by using ultrashort laser pulses and the ReMi. In detail, linearly polarized laser pulses are delivered by the commercial Ti:Sapphire laser (see Section 3.1.3) at the central wavelength of 800 nm. The pulse duration, pulse energy and the repetition rate of the laser are 25 fs, 1 mJ and 3 kHz respectively. The intensity of the laser field at the focus is estimated to be 10^{14} W/cm^2.

6.2.1 Bound and dissociative ionization

The full momentum distributions of electrons for bound and dissociation channels are shown in Fig. 6.4 (a) and (b) respectively. $p_{\parallel}$ and $p_{\perp}$ denote the longitudinal (along the laser polarization direction) and transverse momentum. As introduced in Chapter 5, the finger-like stripes and the ATI rings in the photoelectron spectra are caused by the so-called intracycle and intercycle interference. These featured structures of the electrons appear in the same positions for both channels, as expected from the two-step mechanism. However, the yield of electrons in low momentum is clearly enhanced for the bound ionization channel [Fig. 6.4 (a)] while the same low-momentum structure is much less pronounced in the spectrum for dissociative ionization channel [Fig. 6.4 (b)].

Note that we do not have the same ionization yield for the two channels because the bound ionization requires less energy from the laser field and thus is dominant among all the ionization channels. In order to compare the electrons released from the two channels, we normalized the photoelectron energy spectra, shown in Fig. 6.4 (c). In the high-energy (> 0.6 eV) region, the two spectra agree within our experimental resolution. For instance, the peaks at around 0.9 eV caused by the Freeman resonance (see Section 2.1.2) appear for both channels. However, in the low-energy region (0 - 0.6 eV), an enhancement is observed for the electrons from the bound ionization channel.

These results are surprising because they are not consistent with the two-step mechanism, in which the electrons from the two channels are deemed to be identical. The observation of the difference in low-energy electron emission between the bound and dissociative ionization of H_2 in strong laser fields differs from the results in [Fec14] and has not been published in a peer reviewed journal. This proves that the two-step mechanism, which considers the dissociative ionization independent of the bound ionization, is not complete.
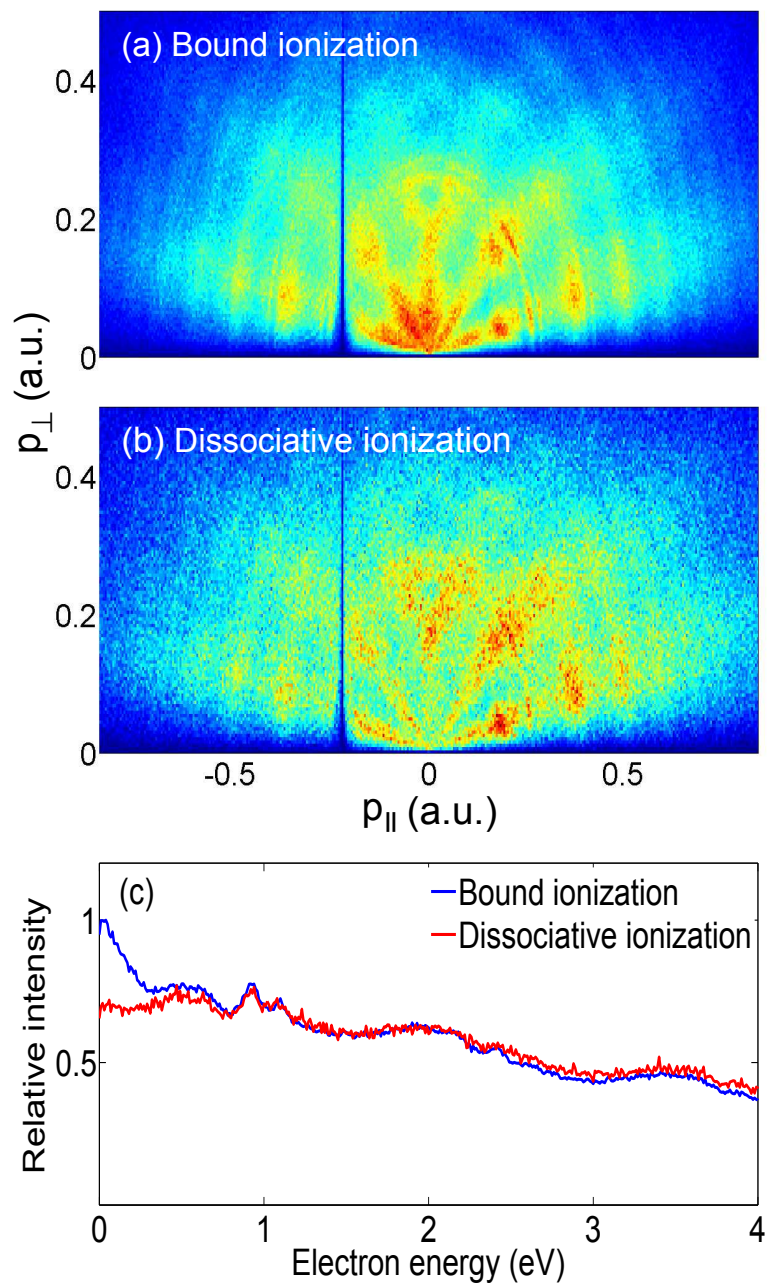
Figure 6.4: 3D electron momentum distribution for (a) the bound ionization channel and (b) dissociative ionization channel. (c) Photoelectron energy spectra for bound (blue curve) and dissociative (red curve) ionization. Figure taken from [MCF+17].

The interpretation of this observation will be introduced in Section 6.3.

6.2.2 Bond softening and above threshold dissociation

According to different nuclear energies or the so-called Kinetic Energy Release (KER), one can identify the dissociative ionization of H_2 molecules as bond softening (BS) and above threshold dissociation (ATD) [KSV$^+$06, RHD$^+$09]. As a clear difference was observed in the electron energy spectra between bound and dissociative ionization, a natural consideration is to resolve the electrons from the two dissociative ionization pathways.

Fig. 6.5 (a) shows the KER distribution up to 2.5 eV for the dissociative ionization channel. The BS pathway leads to low-energy protons as the binding potential is lowered by the laser field. Thus, region (1) (KER < 0.6 eV) corresponds to the BS while region (2) (KER > 0.6 eV) represents the ATD. In order to investigate the difference in electrons between the BS and the ATD, a two-dimensional photoelectron energy spectrum is plotted as a function of the KER, shown in Fig. 6.5 (b). We see most electrons emitted when the KER varies from 1 to 1.5 eV, corresponding to the ATD process. A minor part of electrons can be extracted from the BS channel. By integrating over the KER in region (1) and (2) in Fig. 6.5 (a), the energy spectra of electrons in coincidence with the BS (red curve) and the ATD (black curve) channels are obtained and shown in Fig. 6.5 (c). For comparison, the spectrum (blue curve) for bound ionization is also shown in Fig. 6.5 (c). The energy spectra between bound and the two dissociative ionizations are distinguishing in the low-energy (0 - 0.6 eV) region. However, for the two pathways (BS and ATD) of dissociative ionization, there is no significant difference in the spectra.

6.3 Vibrational autoionization

Why is there a clear difference in the low-energy electron spectra between bound and dissociative ionization channels of H_2 in the strong laser field? Why do the BS and the ATD pathways in the dissociation of H_2 have almost the identical electron spectra? These two remaining questions will be answered in this section. The enhancement in low-energy electron yield for bound ionization channel is interpreted as being due to the population and subsequent decay of autoionizing states.

6.3.1 Autoionizing states of H_2

Different from the doubly excited states of H_2, the above-mentioned autoionizing states are singly excited states representing a series of high-lying Rydberg states, which are characterized by a simultaneous electronic and vibrational excitation. In the 1960s, the Rydberg states and the ionization potential of H_2 molecules have been experimentally investigated by Chupka, Takezawa, Herzberg *et al.* (e.g. [CB69, HJ72, Tak70]) by using high-resolution absorption spectroscopy at low temperature. For H_2 molecules near the ionization threshold, there exist two series of Rydberg states $np\sigma$ ($^1\Sigma_u^+$) and $np\pi$ ($^1\Pi_u$). These Rydberg states with vibrational quantum number v converge to the state of H_2^+
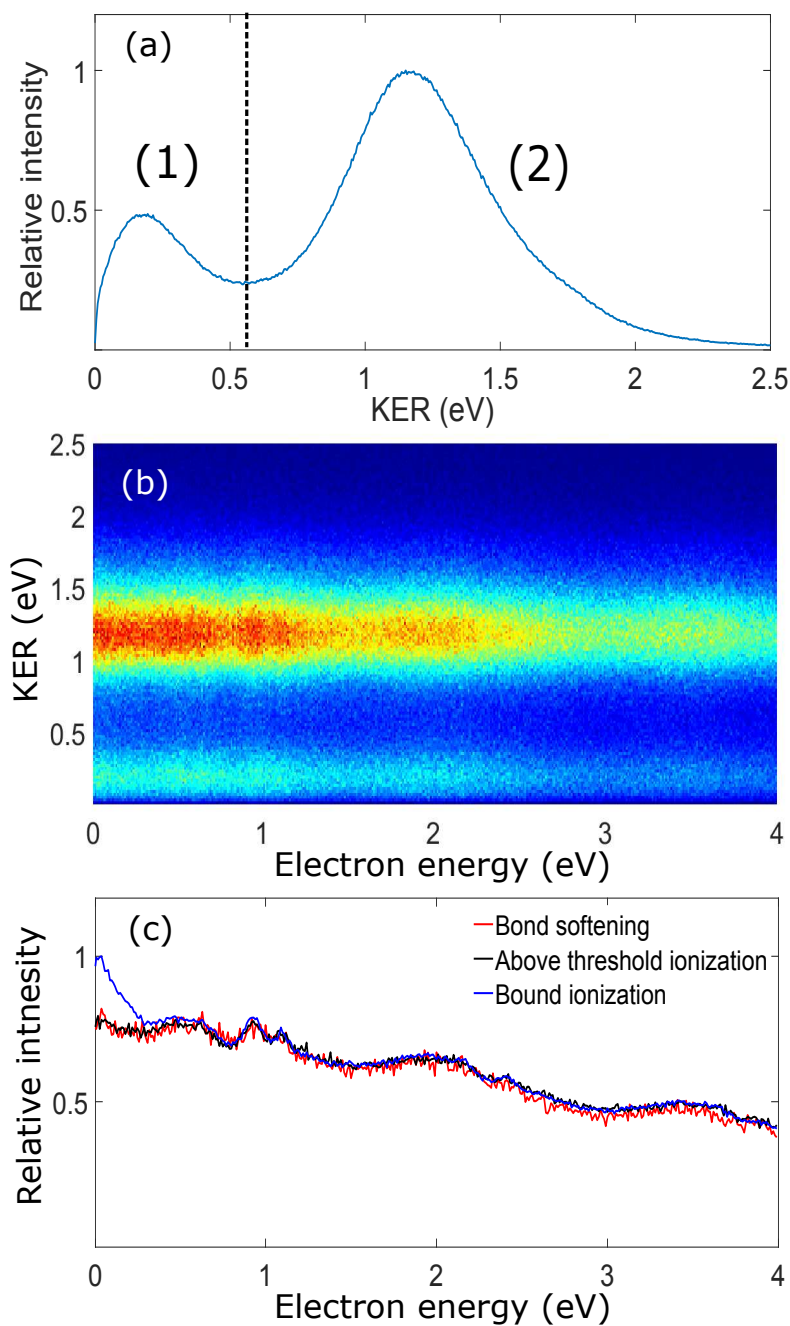
Figure 6.5: (a) The kinetic energy release (KER) distribution and (b) electron energy spectrum as a function of the KER for dissociative ionization of H2. (c) Electron energy spectra for bond softening (red curve), above threshold ionization (black curve) and bound ionization (blue curve).
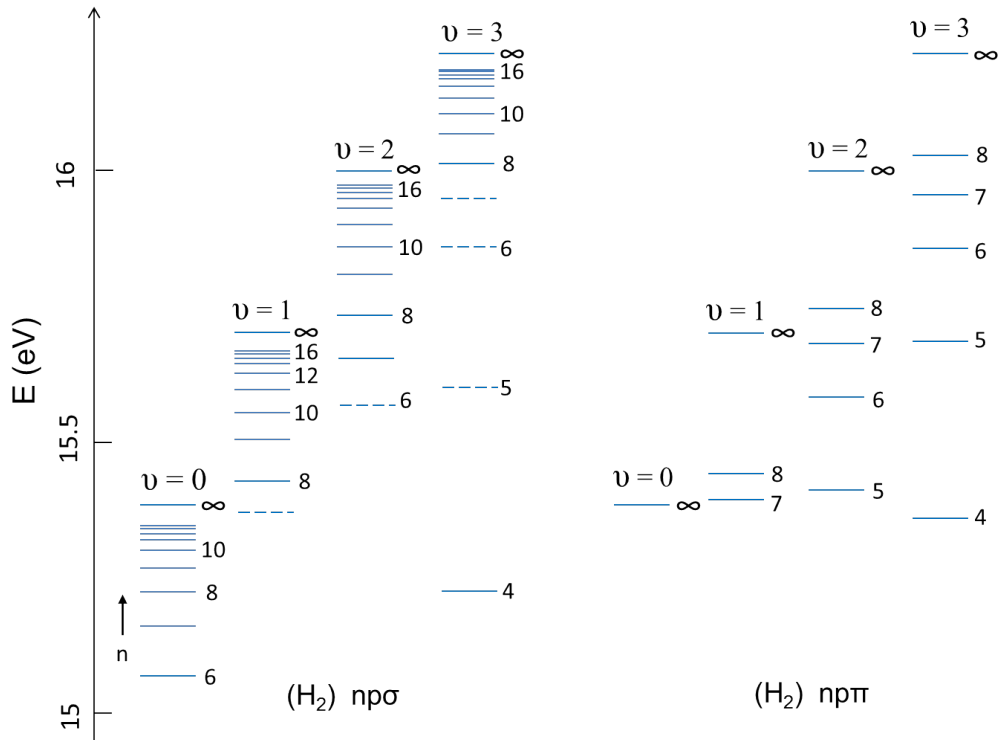
Figure 6.6: Schematic drawing of energy levels of the $np\sigma$ and $np\pi$ Rydberg (autoionizing) states. These states with vibrational quantum number $v = 0$ converge to the ground state ($v = 0$) of the H_2^+ molecular ion. The states with vibrational quantum number $v \neq 0$ converge to the vibrationally excited state of the H_2^+ molecular ion with the same quantum number v. Figure adapted from [CB69].

with the same vibrational quantum number v, as shown in Fig. 6.6. If $v = 0$, the Rydberg states converge to the ground state of the H_2^+ molecular ion.

As these vibrationally excited Rydberg states with large principle quantum number n (n > 8) lie above the energy level of the ionization potential of H_2, an autoionization process may occur by conversion of vibrational energy into electronic energy [CB69]. This process is referred to as vibrational autoionization, which is attributed by Dibeler *et al.* to breakdown of the Born-Oppenheimer approximation [DRK65]. Theoretical treatment of the autoionization was implemented by Berry [Ber66] for the first time and then developed and corrected by Bardsley [Bar67]. According to their calculation, this vibrational autoionization process is slower than the autoionization of atoms but faster than the decay of fluorescence. Afterwards, by using multichannel quantum defect theory (MQDT) [Fan70], further theoretical methods are performed to determine e.g. the energies or the widths of these Rydberg states [GMJS$^+$11, SJM14].

Lifetime of these autoionizing states can be estimated by the inverse of their resonance linewidth $\hbar/\Gamma$, where Γ is the energy width of the resonance. Table 6.1 shows the observed energy E(obs), energy width Γ(obs) of parts of absorption transitions [P(1) transitions] from ground state of H_2 ($X^1\Sigma_g^+, v = 0$) to these autoionizing states $np\sigma$ ($^1\Sigma_u^+, v = 1, 2$). We find the data from high-resolution spectroscopy of H_2 measured by Glass-Maujean *et al.* [GMJS$^+$11] Thus, the lifetime τ of these autoionizing states can be calculated from the

**Table 6.1**: P(1) transitions in ground state absorption of H_2 [GMJS$^+$11]

State	v	E (obs) (cm^{-1})	Γ (obs) (cm^{-1})	τ (ps)
$8p\sigma$	1	124 728.1	4.29 ± 0.64	1.24 ± 0.18
$9p\sigma$	1	125 109.2	3.01 ± 1.39	1.76 ± 0.81
$10p\sigma$	1	125 401.0	2.55 ± 0.66	2.08 ± 0.54
$11p\sigma$	1	125 603.9	0.60 ± 0.69	8.85 ± 10.18
$12p\sigma$	1	125 754.3	0.98 ± 0.65	5.41 ± 3.59
$13p\sigma$	1	125 872.6	0.48 ± 0.94	11.06 ± 21.66
$14p\sigma$	1	125 965.8	0.53 ± 0.66	10.02 ± 12.48
$18p\sigma$	1	126 189.3	0.37 ± 0.64	14.35 ± 24.82
$19p\sigma$	1	126 236.9	0.37 ± 0.27	14.35 ± 10.47
$20p\sigma$	1	126 265.8	0.38 ± 0.35	13.97 ± 12.87
$21p\sigma$	1	126 291.9		
$22p\sigma$	1	126 314.7	0.96 ± 0.71	5.53 ± 4.09
$23p\sigma$	1	126 333.8	0.77 ± 0.73	6.90 ± 6.54
$24p\sigma$	1	126 351.9		
$8p\sigma$	2	126 769.4	13.66 ± 0.92	0.39 ± 0.02
$9p\sigma$	2	127 186.7	7.04 ± 1.48	0.75 ± 0.10
$10p\sigma$	2	127 431.3	1.96 ± 0.66	2.71 ± 0.91
$11p\sigma$	2	127 656.8	5.70 ± 0.79	0.93 ± 0.13
$12p\sigma$	2	127 809.6	3.74 ± 0.77	1.42 ± 0.29
$15p\sigma$	2	128 087.5	0.21 ± 0.66	25.28 ± 92.71
$16p\sigma$	2	128 167.4	1.77 ± 1.09	3.00 ± 1.85
$18p\sigma$	2	128 258.6	0.72 ± 1.04	7.37 ± 11.16
$20p\sigma$	2	128 325.2		
$22p\sigma$	2	128 374.0	0.0 ± 0.9	

observed energy width. As shown in Table 6.1, the calculated lifetime is in the picosecond regime.

6.3.2   Electron-nuclear coupling after strong-field excitation of H_2

Though the above mentioned vibrationally autoionization had been brought to light decades before the strong femtosecond laser was invented, this mechanism has never been reported in the laser-induced strong-field ionization of H_2 molecules. Now we interpret our experimental results on the enhancement of the low-energy electrons for bound ionization channel (see Section 6.2) by using the autoionization mechanism.

Fig. 6.7 shows one of the Rydberg states H_2^* (black curve), together with its first three vibrational states (black dashed lines). The autoionizing states e.g. $v' = 1$ and $v' = 2$ in Fig. 6.7 have energies above the ionization limit of the H_2^+ molecular ion ($v = 0$, shown in red solid line). In the presence of the laser field, instead of populating the bound state (red curve) of the H_2^+ and subsequently being excited to the repulsive state (blue curve) for dissociation, which is described by the two-step model [shown as (1) and (2)] , the molecule can also be excited to the autoionizing states located above the ionization limit [shown as (3)]. The autoionization occurs in which the vibrational energy of the nuclei is transferred
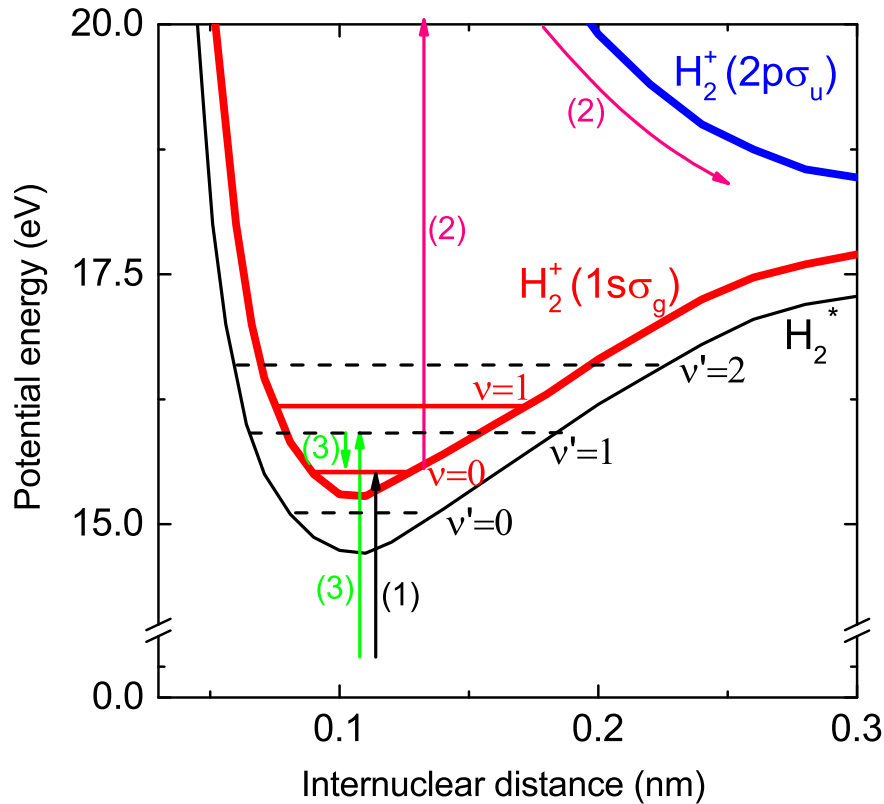
Figure 6.7:   Potential energy curves for one of the Rydberg states H_2^* (black curve), H_2^+ bound state (red curve) and H_2^+ repulsive state (blue curve). (1) and (2) show the main dissociation process by the two-step mechanism: the molecule is ionized by the laser field and then a vibrational wavepacket is excited from the bound $1s\sigma_g$ state to the repulsive $2p\sigma_u$ state. (3) refers to the autoionization process in which low-energy electrons are emitted. All the vibrational states are not drawn to scale. Figure taken from [MCF$^+$17].

to the energy of the free electron and is hence reflected in the electron energy spectrum. From Table 6.1, we know the lifetime of these vibrational states is more than hundreds of femtoseconds, which is much longer than the duration of the laser pulse (25 fs). Thus, the vibrational autoionization of H_2 takes place long after the strong-field excitation of the molecule by the laser pulses. As the dissociative ionization occurs within the time scale of laser pulses [MAS$^+$12], this explains why the autoionization does not occur for the dissociative ionization channel. In addition, the corresponding autoionizing states are located below the dissociation limit in energy. Hence, the enhancement in the low-energy electron yield only appears for the bound ionization, not for the dissociative ionization. For the two dissociative ionization pathways, bond softening (BS) and above threshold dissociation (ATD) occur due to the interaction between H_2^+ and the laser field. The autoionization does no affect the two pathways and thus there is no significant difference in the electron spectra between the two pathways (see Fig. 6.5).

The above mentioned autoionization is in fact an electron-nuclear coupling through autoionizing states after the laser excitation, where the Born-Oppenheimer approximation is
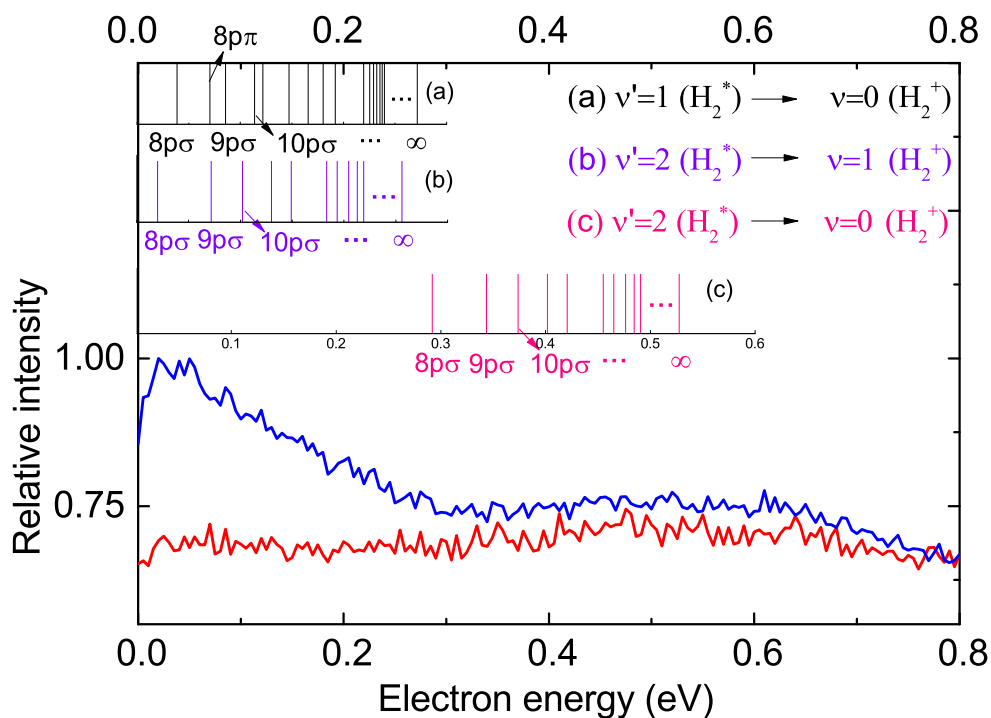
Figure 6.8: Energy-level diagram of the Rydberg states ($v' = 1$ and $v' = 2$) of H_2^* subtracting the first two vibrational levels ($v = 0$ and $v = 1$) of the H_2^+ ground state. For comparison, the photoelectron energy spectra for the bound (blue curve) and dissociative (red curve) ionization are shown in the lower panel. Figure taken from [MCF$^+$17].

not valid any more. Note that the vibrational autoionization is different from the ionization of Rydberg electrons by the field of the spectrometer [DCT$^+$13, WLB$^+$14, DSR$^+$16, LEL$^+$16], though low-energy structure could also be observed in the photoelectron energy spectrum. However, in those cases, the structures are very sharp and in a much lower energy region, normally named very-low-energy structure (VLES) or zero-energy structure (ZES) [WLB$^+$14].

As discussed in Section 6.3.1, numerous theoretical and high-resolution experimental work have been carried out on Rydberg states of H_2 (e.g. [HJ72, Tak70, Ber66, Bar67, SJM14, BM16]) after the vibrational autoionization was first pointed out [DRK65]. By comparing the electron energy spectrum of bound ionization in our experiment with these work, we are able to determine the vibrational states contributing to the autoionization process. Fig. 6.8 (a) shows the energy levels of a series of $np\sigma$ and $np\pi$ Rydberg states ($v' = 1$) of H_2 subtracting the energy of the H_2^+ ground state ($v = 0$). Similarly, Fig. 6.8 (b) presents the energy differences between the $v' = 2$ Rydberg series and the energy of the $v = 1$ state of H_2^+. Fig. 6.8 (c) presents the energy levels originating from the transitions from $v' = 2$ Rydberg states to the $v = 0$ state of H_2^+. For comparison with our experimental results, the photoelectron energy spectra (PES) from bound and dissociative ionizations are plotted together in Fig. 6.8, shown in blue and red respectively. Though not all transitions are shown in this figure, these energy levels exactly overlap with the

enhanced-ionization region (0 - 0.6 eV) in the PES. According to the propensity rule in vibrational autoioinization [Ber66, JP10, GMJS$^+$11], the most dominant vibrational relaxations proceed from one vibrational state to another one that differs by one vibrational quantum number:

$$\Delta v = v' - v = 1 \tag{6.4}$$

From Fig. 6.8, it can also be seen that photoelectrons from the $\Delta v = 2$ transitions are distributed in a higher range (> 0.3 eV) of the spectrum and these transitions contribute much less than the $\Delta v = 1$ transitions for the bound ionization, which agrees well with the propensity rule.

6.4 Investigation with two-color laser pulses

As discussed in Chapter 3 and Chapter 5, the phase-controllable two-color laser pulses allow to shape the electric field on attosecond time scales and to precisely control the asymmetric electron emission direction or the fragments emission in the dissociation of diatomic molecules [RHD$^+$09, GHS$^+$14]. For instance, Ray *et al.* resolved the BS, ATD and rescattering processes by investigating the ion-energy dependent asymmetry obtained by tuning the relative phase between the 800 nm and 400 nm laser pulses. However, the electron-energy dependent asymmetry is rarely studied because the extraction of electrons from different ionization channels requires the high-resolution ion-electron coincidence technique.

In order to further investigate the difference between bound and dissociative ionization channels, we apply the two-color method which has been employed in the measurement of Ar and N_2 (see Section 5.2) for H_2. As introduced in the case of Ar and N_2, changing relative time delay between the two-color fields makes the total electric field asymmetric and this asymmetry is imprinted in the electron energy and the direction of emission. Recalling the mechanism of the above mentioned vibrational autoionization which occurs long after the laser pulse, we expect the electrons from this process to be unaffected by the asymmetric laser field.

The electron-energy dependent asymmetry parameter is defined as the one in Section 5.2.1:

$$A(E_e, \phi) = \frac{N_+(E_e, \phi) - N_-(E_e, \phi)}{N_+(E_e, \phi) + N_-(E_e, \phi)}, \tag{6.5}$$

where $N_+(E_e, \phi)$ and $N_-(E_e, \phi)$ denote the number of electrons at the energy E_e emitted with positive and negative longitudinal momentum at the phase ϕ. Fig. 6.9 (a) and (b) show this asymmetry parameter A for bound and dissociative ionization channels. The asymmetry patterns for the two channels are almost identical within our experimental resolution except for the amplitude of the asymmetry in the low energy region. To quantitatively compare the two channels, we fit the asymmetry by the sinusoidal function used in the previous chapter:

$$A(\phi, E_e) = A_0(E_e)\sin(\phi + \phi_0(E_e)) \tag{6.6}$$

with $A_0(E_e)$ the amplitude of the asymmetry and $\phi_0(E_e)$ the offset of this asymmetry. $A_0(E_e)$ as a function of the electron energy (0 - 1.5 eV) is plotted in Fig. 6.9 (c). In
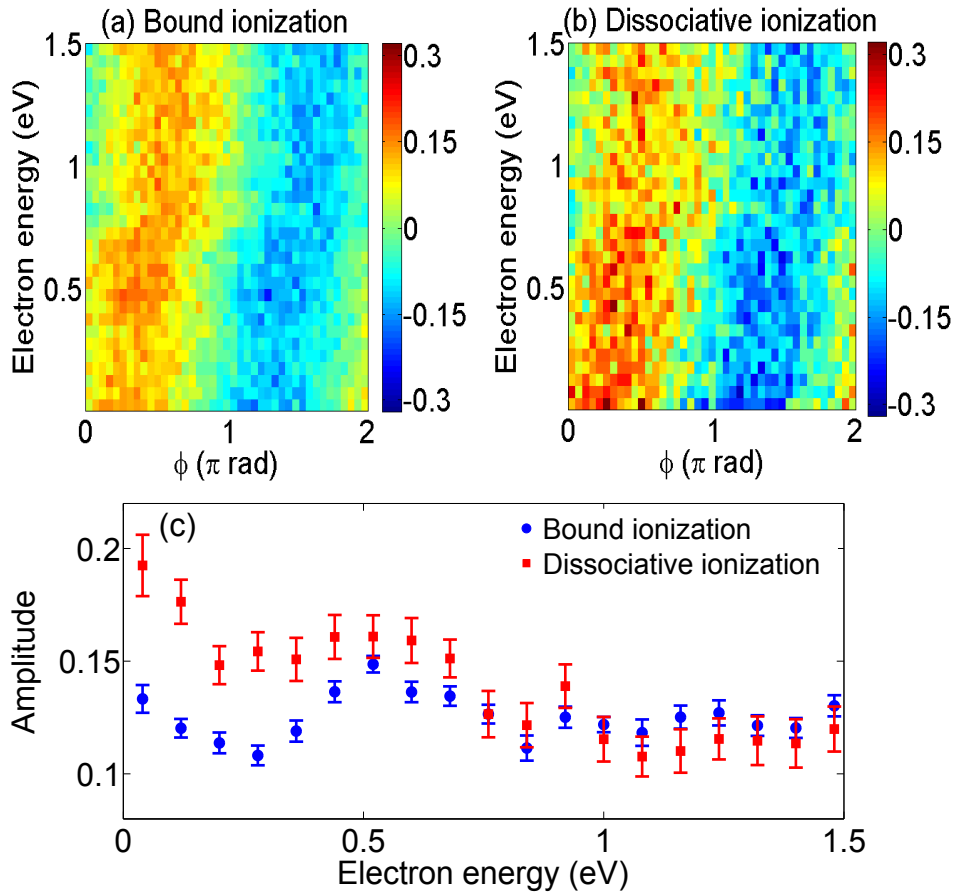
Figure 6.9:   Asymmetry of electrons as a function of the relative phase between the two-color fields and the energy of electrons for (a) bound ionization and (b) dissociative ionization. (c) The amplitude of the electron asymmetry as a function of electron energy for bound ionization (blue dot) and dissociative ionization (red square). Figure taken from [MCF+17].

the low-energy region (0 - 0.6 eV) the electrons from the dissociative ionization have higher asymmetry amplitude than the electrons from the bound ionization while in the high-energy region (> 0.6 eV) the asymmetries of the two electrons are almost the same. These results confirms that the measured low-energy electrons in coincidence with the two channels stem from difference channels. This is consistent with our interpretation (autoionization mechanism) of the experimental results.

The decrease of the amplitude of electron asymmetry for the bound ionization is attributed to the presence of autoionizing states. Note that the low-energy electrons originate from two different mechanisms for the bound ionization channel. The first one is direct ionization by the laser field and the second one is the vibrational autoionization. However, for the dissociative ionization, the low-energy electrons only stem from the direct ionization by the two-color laser field. Therefore, the asymmetry effect on the electron momentum is mostly visible once the electron is freed within the pulse, as expected from strong-field ionization [ALN+15, RKS+16]. Since the emission of the electrons from autoionization process occurs long after the laser pulse is over, the asymmetric emission of electrons is not influenced by the relative phase between the two- color laser pulses and thus shows
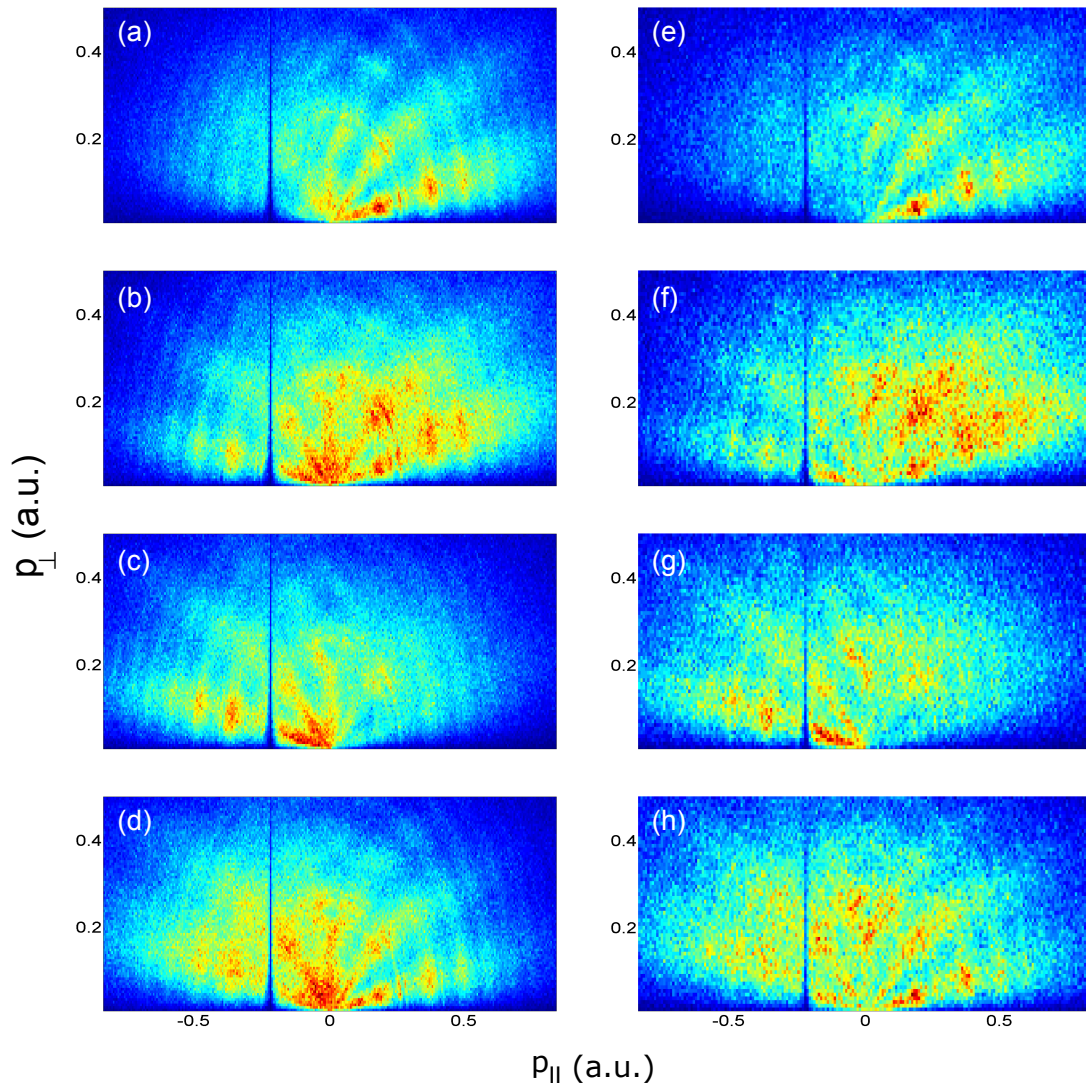
Figure 6.10:   Electron momentum distributions for (a) - (d) bound ionization and (e) - (h) dissociative ionization at different relative phases [(a) and (e) 0.25π, (b) and (f) 0.75π, (c) and (g) 1.25π, (d) and (h) 1.75π] between the two-color laser pulses.

no asymmetry. Therefore, the amplitude of the low-energy electron asymmetry for the bound ionization channel is lower than the dissociative ionization channel.

In order to visualize the ultrafast dynamics of electrons from different pathways, the phase-dependent electron momentum spectra are plotted for bound and dissociative ionization, as shown in Fig. 6.10. This figure displays the electron momentum distributions when the relative phases between the two-color fields are 0.25π [(a) and (e)], 0.75π [(b) and (f)], 1.25π [(c) and (g)], 1.75π [(d) and (h)]. As the relative phase varies from 0 to 2π, most electrons from the bound ionization channel [Fig. 6.10 (a) - (d)] and the dissociative ionization channel [Fig. 6.10 (e) - (h)] are distributed from positive longitudinal momentum to negative longitudinal momentum due to the asymmetry change of the laser field.

In summary, the difference in electron emission between bound and dissociative ioniza-

tion channels is investigated by using the phase-controllable two-color (800 nm + 400 nm) laser pulses. We observed a clear enhancement in low-energy electrons yield for bound ionization compared with the dissociation ionization, proving the widely-used two-step mechanism is not complete. We interpret this result as the population of the high-lying Rydberg states and subsequent vibrational autoionization process. The two-color experiment further reveals the electrons from the two channels have different asymmetry patterns in the laser fields, which firmly supports the autoionization mechanism.

Chapter 7

Towards longer wavelengths: THz experiments

Our experimental results discussed in Chapter 5 and Chapter 6 have proved that the two-color (800 nm + 400 nm) laser pulses can be served as great tools to control ultrafast electronic dynamics in atoms and molecules. By changing the relative time delay between the 800 nm and 400 nm laser pulses, the total pulse shape can be modulated from symmetric to asymmetric with the precision of attoseconds. Asymmetric electron emission can thus be controlled with such two-color laser pulses. However, there are also limitations for the two-color experiments when considering a pump-probe experiment, in which the pump pulse initiates the ionization and the probe pulse with variable time delay is used to investigate the reaction process. Here, the 400 nm laser pulses probe the ultrashort dynamics by changing the asymmetry of electrons. As both laser pulses contribute for the ionization, we cannot distinguish whether the emitted electrons are ionized by the fundamental-frequency photons or by the second-harmonic photons.

To overcome the limitations, we propose to utilize a laser pulse with longer wavelength such that its photon energy is sufficiently low and does not cause ionization. One promising candidate is called terahertz (THz) wave, which is an electromagnetic wave in a frequency interval from 0.1 to 10 THz [HF11]. This chapter mainly deals with the current experimental results on the generation and detection of single-cycle THz pulses and the future follow-on work on an IR-pump-THz-probe experiment.

7.1   THz gap

THz waves sit in the electromagnetic spectrum between the microwaves and the infrared frequencies, as shown in Fig. 7.1. For electromagnetic waves having lower frequencies (e.g. radio waves or microwaves), they can be described by the Maxwell's equations. For higher frequency waves such as visible lights and x-rays, quantum theory plays a key role in describing their properties. Although the THz radiation has been discovered more than 100 years ago [Kim03], the development of THz science and technology is limited compared to the electronics and photonics due to the lack of intense THz emitters and
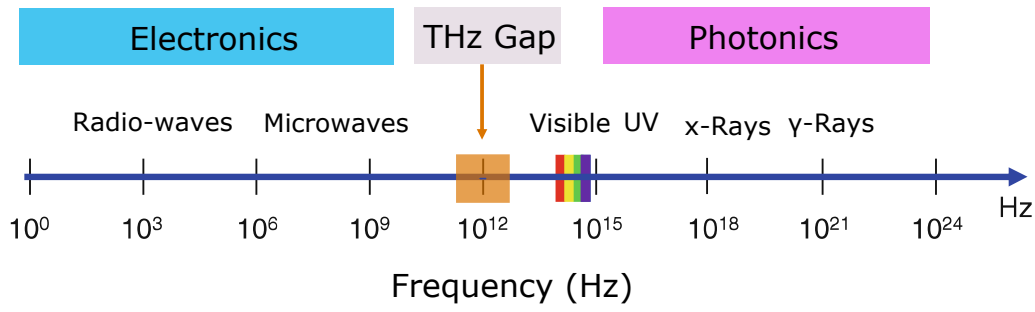
Figure 7.1: The schematic drawing of the electromagnetic spectrum. THz radiation lies in the frequency range of 0.1 - 10 THz. For lower and higher frequency regions the electromagnetic waves can be described by electronics and photonics respectively. Due to lack of suitable emitters and sensors for the past decades, the electromagnetic waves in the THz range have barely been investigated. This frequency range is thus called the THz Gap.

suitable detectors. As a result, there do not exist well developed technologies for the band of frequencies in the THz region of the electromagnetic spectrum and this frequency range is thus referred to as the THz gap.

7.2   Generation and Detection of single-cycle THz pulses

7.2.1   THz generation

A large effort has been made to fill this gap for the past three decades. For example, Auston and Smith in 1983 demonstrated the generation and detection of THz waves can be realized by using a photoconductive switch [AS83], which are nowadays widely used for the THz time-domain spectroscopy (TDS). Strong THz radiation can be generated from various methods such as free electron laser (FEL) [FWG+09], quantum cascade laser [KTB+02] or using nonlinear optics [ZX10]. In particular, the development of high-power femtosecond lasers benefits the generation of coherent and intense single-cycle THz pulses, which will be discussed in this section.

One of the most straightforward methods is directly passing the femtosecond laser pulses through a nonlinear crystal. In our experiment, the laser pulses are generated from the amplified Ti:Sapphire laser system with the central wavelength of 800 nm and a zinc telluride (ZnTe) crystal is chosen for the THz generation. This scheme can be theoretically described by the so-called optical rectification (OR) process [HF11], which is based on difference frequency generation (DFG) between the spectral components of a single laser pulse. From the knowledge of nonlinear optics which has been introduced in Section 2.3, the light-induced nonlinear polarization is given by

$$P_{NL}(\Omega) = \varepsilon_0 \chi^{(2)} \int_0^\infty d\omega E(\omega + \Omega) E^*(\omega) \qquad (7.1)$$

where Ω represents the THz frequency and ω is the pump-laser frequency. As introduced before, ε_0 and $\chi^{(2)}$ denote the permittivity of free space and the second-order nonlinear

susceptibility respectively. In order to maximize the OR efficient, the following phase matching condition

$$\Delta k(\Omega) = k(\Omega) + k(\omega) - k(\omega + \Omega) = 0 \quad (7.2)$$

has to be fulfilled. As the frequency of the THz wave is a few orders of magnitude less than the frequency of optical lasers ($\Omega \ll \omega$), the term $k(\omega + \Omega) - k(\omega)$ can be approximated by

$$k(\omega) - k(\omega + \Omega) \approx \left. \frac{\partial k}{\partial \omega} \right|_{\omega_0} \Omega. \quad (7.3)$$

This way, Equation 7.2 is transformed into

$$\left. \frac{\partial k}{\partial \omega} \right|_{\omega_0} = \frac{k(\Omega)}{\Omega}. \quad (7.4)$$

Recalling the definition of the group velocity (see Equation 3.21) in Chapter 3, the phase matching condition is given by

$$v_g(\omega_0) = v_p(\Omega). \quad (7.5)$$

This equation means the most efficient THz generation requires the group velocity of the pump laser $v_g(\omega_0)$ to be equal to the phase velocity of the emitted THz pulses $v_p(\Omega)$, which is also called velocity matching. In experiment, this velocity matching can be realized by rotating and tilting the ZnTe crystal such that the power of the generated THz radiation is optimized.

Although the THz generation from the ZnTe is straightforward and can be easily realized in experiment, the pump-to-THz energy conversion efficiency is low (10^{-5} [VDT$^+$14]) due to the strong absorption of THz in the ZnTe crystal at the wavelength of 800 nm. In 2002, Hebling *et al.* proposed a tilted-pulse-front pumping (TPFP) method in which the wavefront of an IR laser pulse is tilted by an angle for efficient phase-matched THz generation in a lithium niobate (LiNbO$_3$) crystal [HAKK02]. The principle of the TPFP method is shown in Fig. 7.2. By tilting the pulse front of the pump laser by an angle γ, an intense THz beam can be generated and propagates with a fixed phase with respect to the laser pulse front if the following condition is fulfilled

$$v_g(\omega_0)\cos\gamma = v_p(\Omega). \quad (7.6)$$

The pulse front tilt angle γ equals to the angle between the propagation directions of THz pulses and the laser pulses, which in turn requires the LiNbO$_3$ crystal to be cut in a specific orientation (shown in Fig. 7.2). From Equation 7.6, the tilt angle γ can be calculated with knowing the refractive index of the crystal for the pump laser $n_g(\omega_0)$ and the one for THz wave $n(\Omega)$. For the TPFP with 800 nm laser pulse, the angle is optimal at approximately 63°. Experimentally, the pulse front of the laser is tilted by a grating (e.g. 1800 lines/mm). A half waveplate is placed after the grating to fit the polarization of the laser with the z-axis of the LiNbO$_3$ crystal. Afterwards, the laser beam on the surface of the grating is imaged into the crystal by using a lens or a 4f-lens configuration. With this method, Hirori *et al.* in 2011 reported the generation of single-cycle THz pulses with electric field more than 1 MV/cm [HDBT11]. Furthermore, by cryogenically cooling the
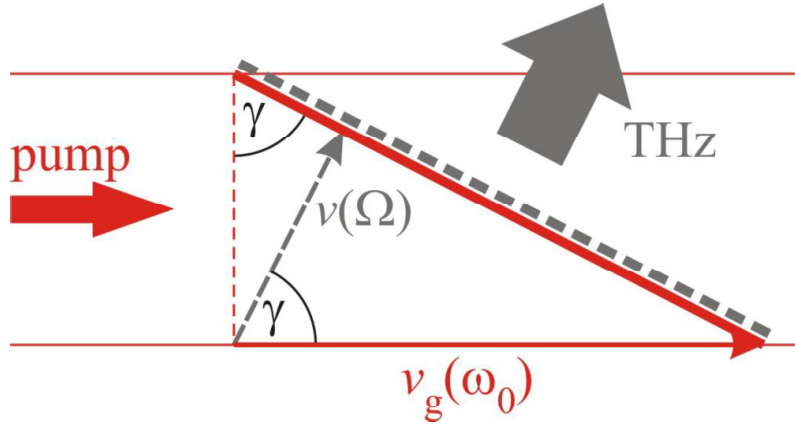
Figure 7.2: The principle of the tilted-pulse-front pumping (TPFP) method. The red arrow indicates the propagation direction of the pump laser and the red solid line denotes the tilted laser pulse front. The gray dashed line represents the THz phase front, perpendicular to which the THz pulses are emitted, as shown in gray arrow. Figure taken from [HF11].

LiNbO$_3$ crystal, Huang *et al.* in 2013 observed the high-energy THz pulses generation with a conversion efficiency above 3.8 % [HGH$^+$13].

High-field (more than 10 MV/cm) THz pulses can also be generated from the OR process in some organic crystals e.g. DSTMS, DAST and OH1 [VJO$^+$15]. However, this method normally requires the wavelength of the pump laser in the range of 1.3 to 1.5 μm, which is beyond the wavelength of the Ti:Sappire laser and have to be obtained with an optical parametric amplifier. Another widely used method for intense THz generation is mixing the two-color (400 nm + 800 nm) femtosecond laser pulses into the air or gases [OYJ$^+$13]. Strong-field and single-cycle THz pulses are emitted from the plasma. Compared with other methods, the THz generated from a two-color laser field has a much broader bandwidth up to tens of THz. As the THz is emitted from the plasma, there is no limit for the damage threshold.

7.2.2 THz detection

Detection of THz pulses can be realized by an electro-optical sampling (EOS) setup. The EOS can be treated as an inverse process of the OR. Fig. 7.3 shows our experimental setup for THz generation and the EOS for THz detection, in which linearly polarized 800 nm laser pulses are split into a pump beam for THz generation and a probe beam for the EOS. ZnTe is used for both THz generation and detection. The crystal used in the EOS is called electro-optical (EO) crystal, whose polarization ellipsoid of the refractive index can be changed by electric field. For a ZnTe crystal, the ellipsoid of the refractive index in the presence of an electric field is given by [ZX10]

$$\frac{x^2 + y^2 + z^2}{n_0^2} + 2\gamma_{41}E_x yz + 2\gamma_{41}E_y zx + 2\gamma_{41}E_z xy = 1, \tag{7.7}$$

where x, y, z are coordinate units of the ellipsoid, E_x, E_y, E_z are the applied electric field along x, y, z axes respectively. n_0 represents the refractive index of the crystal in the ab-
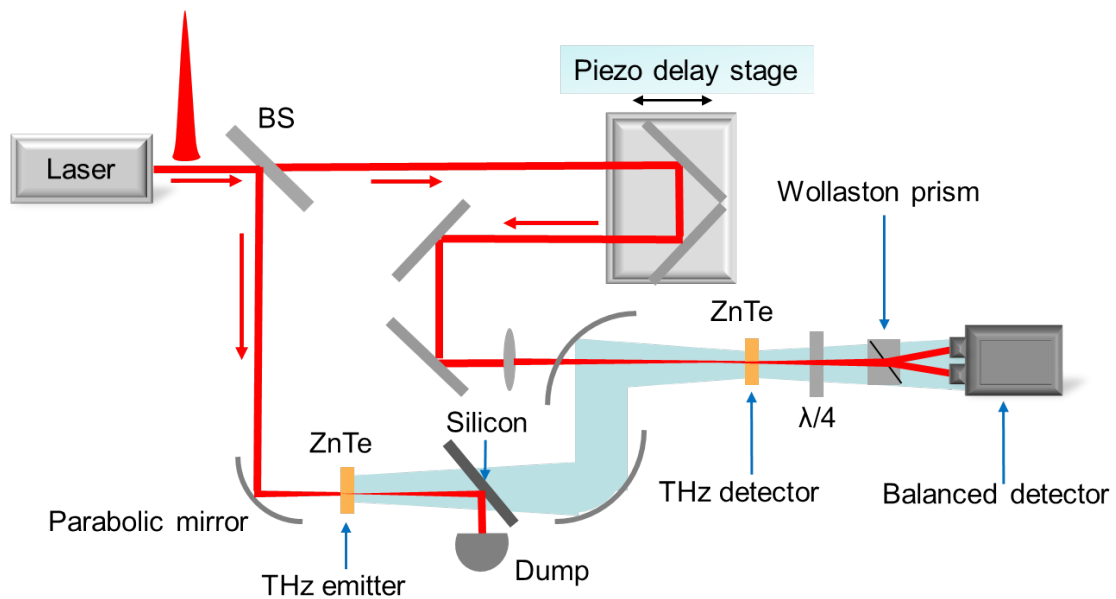
Figure 7.3: Experimental setup for THz generation by using the optical rectification in ZnTe and detection with the eletro-optic sampling (EOS) method.

sence of electric field and γ_{41} is the EO coefficient of the crystal. In experiment, the polarization of the probe beam is normally perpendicular to the optical axis of the EO crystal, as shown in Fig. 7.4. When there is no THz field, we adjust a quarter waveplate such that the polarization of the probe pulses is converted from linear to circular. Two orthogonal polarization components with equal intensities can be further split in space by a Wollaston prism and can be detected by two photodiodes. In the presence of THz field, the generated THz pulses temporally and spatially overlap with the probe laser in the ZnTe crystal, where the THz field changes the birefringence of the crystal. This THz-induced birefringence changes the polarization of the probe beam. After the quarter waveplate, the polarization of the probe pulses is elliptical and the two orthogonal polarization components have different intensities. Therefore, the THz-induced polarization change can be converted to intensity change and can be measured by the balanced detector. By measuring the difference between the two signals as a function of the time-delay between the THz pulse and the probe pulse, the electric field of the THz pulse can be obtained, as shown in Fig. 7.5.

7.3 Future work

More and more intense and broadband THz sources makes the THz gap narrower. However, most researches mainly focused on the technology of THz generation. Investigations on the ultrafast dynamics in atoms and molecules by using THz pulses are limited. One reason is that the generated THz field is too weak such that the THz effect on the electrons emitted from such ultrafast processes are hardly measurable.

In analogy to the attosecond streaking technique [IQY$^+$02], Fruehling *et al.* in 2009
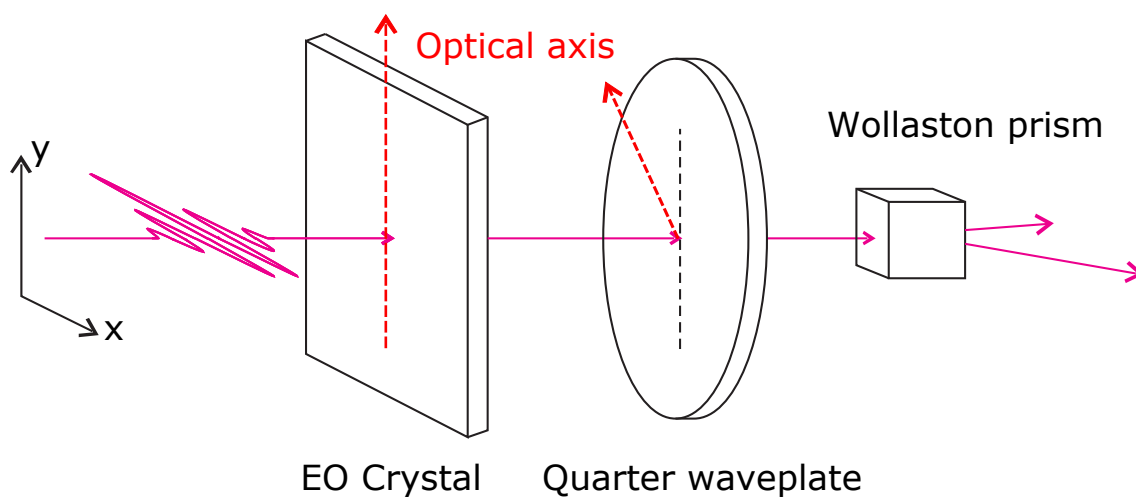
Figure 7.4: Principle of the balanced detection.
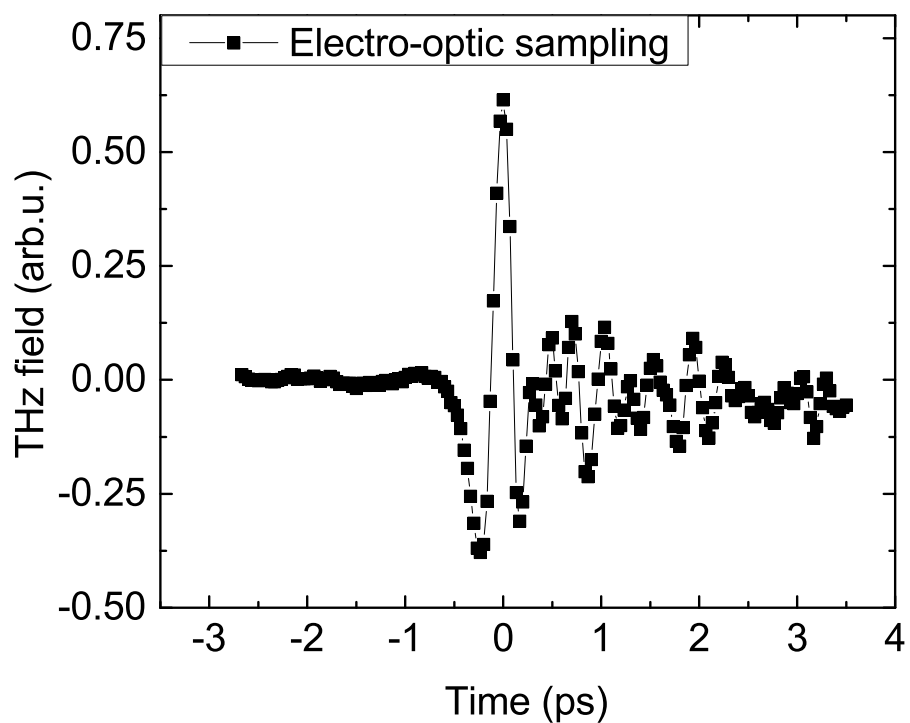
Figure 7.5: Measured eletro-optic sampling (EOS) signal.
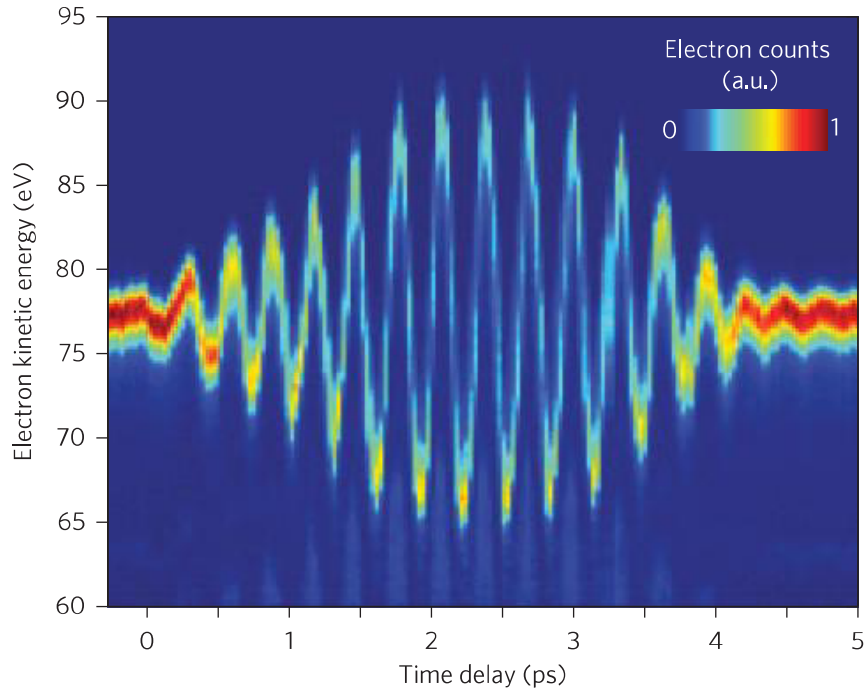
Figure 7.6: Sampled THz vector potential. Kinetic energy spectra of 4p photoelectrons released from krypton atoms by a 13.5 nm soft X-ray pulse in the presence of an intense pulsed THz field. Figure taken from [FWG$^+$09].

demonstrated that THz field generated from the free electron laser (FEL) can be used as a streak-camera to characterize soft X-ray pulses [FWG$^+$09].

In the THz-field driven X-ray streak camera, X-ray pulses are responsible for the photo-ionization in which an electron wavepacket is created. The electrons are accelerated by the electric field of the THz pulse. The momentum change of a photoelectron emitted at time t is given by

$$\Delta p(t) = e \int_t^\infty E_{\text{THz}}(t')dt' = eA_{\text{THz}}(t), \tag{7.8}$$

where A_{THz} is the THz vector potential at the ionization time t. Therefore, the temporal profile of X-ray pulses is mapped onto changes of photoelectron momenta. If the drift velocity of electrons is parallel to the polarization of the THz field, the kinetic energy of photoelectrons is given by [FWG$^+$09]

$$W_{\text{kin}} = W_0 + 2U_p\sin^2(\varphi_i) \pm \sqrt{8W_0U_p}\sin(\varphi_i), \tag{7.9}$$

where W_0 is the kinetic energy without the THz field, φ_i is its phase at the instant of ionization and U_p is the ponderomotive potential of the THz field. Fig. 7.6 shows the kinetic energy spectra of 4p photoelectrons released from krypton atoms by a 13.5 nm soft X-ray pulse in the presence of an intense pulsed THz field. The energy shift versus the time delay between the THz and X-ray pulses denotes the THz vector potential.

Inspired from the THz streaking technique, in the future, we propose to perform a new two-color experiment: IR-pump-THz-probe. In order to achieve a significant THz-effect on the photoelectrons, two aspects should be improved. The first one is to increase the

THz intensity. That is because the momentum shift of the electrons is proportional to the electric field of THz (see Equation 7.8). The other is to improve the momentum resolution of our electron detector. We believe this IR-pump-THz-probe experiment will help us to observe and control more unrevealed ultrafast electron dynamics which cannot be accessed by traditional methods in the atomic or molecular strong-field ionization processes.

Chapter 8

Conclusion

The general theme throughout this thesis is measuring and understanding the ultrafast electronic dynamics of atoms and molecules with a phase-controllable two-color laser field and the ion-electron coincidence detection technique. On one hand, varying the relative phase between the parallel-polarized two-color laser fields changes the field shape on a time scale of attoseconds, which allows the precise control of the electronic wave packet released from the ultrafast laser-induced ionization processes. On the other hand, the coincidence measurement of the Reaction Microscope allows to distinguish the electrons emitted from different species or different ionization channels.

As all the measurements presented in this thesis rely on ultrashort laser pulses, we put forward an accessible time-domain pulse compression method based on the coherent superposition of pulse replicas with different time delays in the time domain. Simulation proved that the pulse durations after compression were close to their Fourier limits for both chirped and statistical laser pulses. Experimentally, 25 fs laser pulses at the central wavelength of 800 nm are generated by the Ti:Sapphire laser. A two-color interferometer was used for the generation of the sculpted pulses. By varying the relative time delay between the two laser fields, the total field shape from symmetric to asymmetric can be precisely controlled. These laser pulses are focused inside the Reaction Microscope, where they intersect a supersonic gas jet. By measuring the particle flight times and their positions of detection, the initial momenta of ions and electrons can be reconstructed.

Two main experimental results were obtained with the help of the Reaction Microscope and the sculpted two-color laser fields. In one measurement, we focused on the single ionization of Ar and N_2 gas mixture in intense laser fields. As Ar atoms and N_2 molecules have similar ionization potentials and they experience the same external conditions in the laser fields, this measurement allows us to compare their different internal structures. The energy spectra and the full momenta of photoelectrons as a function of the relative phase were compared for Ar and N_2. We quantified the emission asymmetry by defining an asymmetry parameter and observed a difference in asymmetric electron emission between the two species. These discrepancies can be attributed to the Freeman resonances, which involve different excited states of atoms and molecules.

In order to investigate the elecronic and internuclear wave packets released from different ionization channels in a single molecule, we choose the most fundamental molecule

– H_2 as our gas target. Channel-selective electron emission from laser-induced photo-ionization of H_2 molecules was investigated. In analogy to the Ar-N_2 experiment, the electron momenta and energy spectra in coincidence with different ionization channels were compared. According to the Born-Oppenheimer-based two-step model, the electrons emitted from the bound ionization channel should be identical with the electrons released from the dissociative ionization channel. However, we observe an enhancement of the photoelectron yield in the low-energy region for the bound ionization channel. By comparison with theory and high-resolution spectra from the literature, we interpret this enhancement as the population and subsequent decay of vibrationally excited autoionizing states (high-lying Rydberg states) of H_2. Further investigations with the two-color laser pulses supported this vibrational autoionization mechanism. In the future, this mechanism can be used to explore the detailed distribution and interplay of vibrational and electronic excitation after strong-field interaction.

The two-color experiment can be regarded as a pump-probe experiment, in which the pump pulse initiates the ionization and the probe pulse with variable time delay is used to investigate the reaction process. The 400 nm laser pulses probe the ultrashort dynamics by changing the asymmetry of electrons. However, one limitation of the two-color fields is that both laser pulses contribute to ionization. To overcome the limitation, we propose to use a laser pulse with longer wavelength – a THz pulse. The field strength of THz radiation is sufficiently low to not cause field ionization. Therefore, the THz pulse can be used as an ideal tool in a pump-probe experiment for streaking electrons created in strong-field ionization. Such a streaking experiment requires intense THz fields. Experimentally, we generated a single-cycle THz pulse by using the optical rectification process in a ZnTe crystal. The method and measurement results of electro-optic sampling for THz detection were presented.

To summarize, the presented results pave the way towards understanding and controlling the electronic wave-packet dynamics in atoms and simple molecules. In the future, we propose an IR-pump-THz-probe experiment, which will help us to observe and control more unrevealed ultrafast electron dynamics in atomic or molecular strong-field ionization processes which cannot be accessed by traditional experimental methods.

Atomic units

It is convenient to use atomic units (a.u.) instead of the International System of Units (SI) in the theoretical description of atomic and molecular physics. The atomic units are based on the scales of the electron in the hydrogen atom. For instance, the length in atomic units is defined by the Bohr radius a_0.

In atomic units the elementary charge e, the electron mass m_e, the reduced Planck constant $\hbar$ and the Coulomb constant of the electric force $1/(4\pi\varepsilon_0)$ are all unity by definition: $e = m_e = \hbar = 1/(4\pi\varepsilon_0) = 1$.

The fine-structure constant α is given by

$$\alpha = \frac{e^2}{(4\pi\varepsilon_0)\hbar c} \approx \frac{1}{137}. \tag{1}$$

This gives the value of speed of light c in atomic units $c \approx 137$. These basic physical quantities and their conversion from atomic units into SI units are listed in Table 1.

Table 1: The basic physical quantities and their conversion from atomic units into SI units.

Atomic unit of	SI value
Mass	$9.10938291 \times 10^{-31}$ kg
Charge	$1.602176565 \times 10^{-19}$ C
Length	$5.2917721092 \times 10^{-11}$ m
Energy	27.21138505 eV
	$4.3597443 \times 10^{-18}$ J
Time	$2.418884326502 \times 10^{-17}$ s
Electric field strength	5.14220652×10^{9} V/cm
Intensity	$3.50944521 \times 10^{16}$ W/cm^2

Bibliography

[AAA+16]   B. P. Abbott, R. Abbott, T. D. Abbott, M. R. Abernathy, F. Acernese, K. Ackley, C. Adams, T. Adams, P. Addesso, R. X. Adhikari, V. B. Adya, C. Affeldt, M. Agathos, K. Agatsuma, N. Aggarwal, O. D. Aguiar, L. Aiello, A. Ain, P. Ajith, B. Allen, A. Allocca, P. A. Altin, S. B. Anderson, W. G. Anderson, K. Arai, M. A. Arain, M. C. Araya, C. C. Arceneaux, J. S. Areeda, N. Arnaud, K. G. Arun, S. Ascenzi, G. Ashton, M. Ast, S. M. Aston, P. Astone, P. Aufmuth, C. Aulbert, S. Babak, P. Bacon, M. K. M. Bader, P. T. Baker, F. Baldaccini, G. Ballardin, S. W. Ballmer, J. C. Barayoga, S. E. Barclay, B. C. Barish, D. Barker, F. Barone, B. Barr, L. Barsotti, M. Barsuglia, D. Barta, J. Bartlett, M. A. Barton, I. Bartos, R. Bassiri, A. Basti, J. C. Batch, C. Baune, V. Bavigadda, M. Bazzan, B. Behnke, M. Bejger, C. Belczynski, A. S. Bell, C. J. Bell, B. K. Berger, J. Bergman, G. Bergmann, C. P. L. Berry, D. Bersanetti, A. Bertolini, J. Betzwieser, S. Bhagwat, R. Bhandare, I. A. Bilenko, G. Billingsley, J. Birch, R. Birney, O. Birnholtz, S. Biscans, A. Bisht, M. Bitossi, C. Biwer, M. A. Bizouard, J. K. Blackburn, C. D. Blair, D. G. Blair, R. M. Blair, S. Bloemen, O. Bock, T. P. Bodiya, M. Boer, G. Bogaert, C. Bogan, A. Bohe, P. Bojtos, C. Bond, F. Bondu, R. Bonnand, B. A. Boom, R. Bork, V. Boschi, S. Bose, Y. Bouffanais, A. Bozzi, C. Bradaschia, P. R. Brady, V. B. Braginsky, M. Branchesi, J. E. Brau, T. Briant, A. Brillet, M. Brinkmann, V. Brisson, P. Brockill, A. F. Brooks, D. A. Brown, D. D. Brown, N. M. Brown, C. C. Buchanan, A. Buikema, T. Bulik, H. J. Bulten, A. Buonanno, D. Buskulic, C. Buy, R. L. Byer, M. Cabero, L. Cadonati, G. Cagnoli, C. Cahillane, J. Calderón Bustillo, T. Callister, E. Calloni, J. B. Camp, K. C. Cannon, J. Cao, C. D. Capano, E. Capocasa, F. Carbognani, S. Caride, J. Casanueva Diaz, C. Casentini, S. Caudill, M. Cavaglià, F. Cavalier, R. Cavalieri, G. Cella, C. B. Cepeda, L. Cerboni Baiardi, G. Cerretani, E. Cesarini, R. Chakraborty, T. Chalermsongsak, S. J. Chamberlin, M. Chan, S. Chao, P. Charlton, E. Chassande-Mottin, H. Y. Chen, Y. Chen, C. Cheng, A. Chincarini, A. Chiummo, H. S. Cho, M. Cho, J. H. Chow, N. Christensen, Q. Chu, S. Chua, S. Chung, G. Ciani, F. Clara, J. A. Clark, F. Cleva, E. Coccia, P.-F. Cohadon, A. Colla, C. G. Collette, L. Cominsky, M. Constancio, A. Conte, L. Conti, D. Cook, T. R. Corbitt, N. Cornish, A. Corsi, S. Cortese, C. A. Costa, M. W. Coughlin, S. B. Coughlin, J.-P. Coulon, S. T. Countryman, P. Couvares, E. E. Cowan, D. M. Coward, M. J. Cowart, D. C. Coyne, R. Coyne, K. Craig, J. D. E. Creighton, T. D. Creighton, J. Cripe, S. G. Crowder, A. M. Cruise, A. Cumming, L. Cunningham, E. Cuoco, T. Dal Canton, S. L. Danilishin, S. D'Antonio, K. Danzmann, N. S. Darman, C. F. Da Silva Costa, V. Dattilo, I. Dave, H. P. Daveloza, M. Davier, G. S. Davies, E. J. Daw, R. Day, S. De, D. DeBra, G. Debreczeni, J. Degallaix, M. De Laurentis, S. Deléglise, W. Del Pozzo, T. Denker, T. Dent, H. Dereli, V. Dergachev, R. T. DeRosa, R. De Rosa, R. DeSalvo, S. Dhurandhar, M. C. Díaz, L. Di Fiore, M. Di Giovanni, A. Di Lieto, S. Di Pace, I. Di Palma, A. Di Virgilio, G. Dojcinoski, V. Dolique, F. Donovan, K. L. Dooley, S. Doravari, R. Douglas, T. P. Downes, M. Drago, R. W. P. Drever, J. C. Driggers, Z. Du, M. Ducrot, S. E. Dwyer, T. B. Edo, M. C. Edwards, A. Effler, H.-B. Eggenstein, P. Ehrens, J. Eichholz, S. S. Eikenberry, W. Engels, R. C. Essick, T. Etzel, M. Evans, T. M. Evans, R. Everett, M. Factourovich, V. Fafone, H. Fair, S. Fairhurst, X. Fan, Q. Fang, S. Farinon, B. Farr, W. M. Farr, M. Favata, M. Fays,

H. Fehrmann, M. M. Fejer, D. Feldbaum, I. Ferrante, E. C. Ferreira, F. Ferrini,
F. Fidecaro, L. S. Finn, I. Fiori, D. Fiorucci, R. P. Fisher, R. Flaminio, M. Fletcher,
H. Fong, J.-D. Fournier, S. Franco, S. Frasca, F. Frasconi, M. Frede, Z. Frei, A. Freise,
R. Frey, V. Frey, T. T. Fricke, P. Fritschel, V. V. Frolov, P. Fulda, M. Fyffe, H. A. G.
Gabbard, J. R. Gair, L. Gammaitoni, S. G. Gaonkar, F. Garufi, A. Gatto, G. Gaur,
N. Gehrels, G. Gemme, B. Gendre, E. Genin, A. Gennai, J. George, L. Gergely,
V. Germain, Abhirup Ghosh, Archisman Ghosh, S. Ghosh, J. A. Giaime, K. D. Giardina,
A. Giazotto, K. Gill, A. Glaefke, J. R. Gleason, E. Goetz, R. Goetz, L. Gondan,
G. González, J. M. Gonzalez Castro, A. Gopakumar, N. A. Gordon, M. L. Gorodetsky,
S. E. Gossan, M. Gosselin, R. Gouaty, C. Graef, P. B. Graff, M. Granata, A. Grant,
S. Gras, C. Gray, G. Greco, A. C. Green, R. J. S. Greenhalgh, P. Groot, H. Grote,
S. Grunewald, G. M. Guidi, X. Guo, A. Gupta, M. K. Gupta, K. E. Gushwa, E. K.
Gustafson, R. Gustafson, J. J. Hacker, B. R. Hall, E. D. Hall, G. Hammond, M. Haney,
M. M. Hanke, J. Hanks, C. Hanna, M. D. Hannam, J. Hanson, T. Hardwick, J. Harms,
G. M. Harry, I. W. Harry, M. J. Hart, M. T. Hartman, C.-J. Haster, K. Haughian,
J. Healy, J. Heefner, A. Heidmann, M. C. Heintze, G. Heinzel, H. Heitmann, P. Hello,
G. Hemming, M. Hendry, I. S. Heng, J. Hennig, A. W. Heptonstall, M. Heurs, .
Observation of gravitational waves from a binary black hole merger.
Phys. Rev. Lett., 116:061102, 2016.

[ADK86]   M. V. Ammosov, N. B. Delone, and V. P. Krainov.
             Tunnel ionization of complex atoms and of atomic ions in an alternating
             electromagnetic field.
             Soviet Physics JETP, 64(6):1191–1194, 1986.

[AFM+79]   P. Agostini, F. Fabre, G. Mainfray, G. Petite, and N. K. Rahman.
             Free-free transitions following six-photon ionization of xenon atoms.
             Phys. Rev. Lett., 42:1127–1130, 1979.

[AIPB12]   D. G. Arbó, K. L. Ishikawa, E. Persson, and J. Burgdörfer.
             Doubly differential diffraction at a time grating in above-threshold ionization:
             Intracycle and intercycle interferences.
             Nucl. Instrum. Meth. Res. B, 279:24 – 30, 2012.

[AIS+10]   D. G. Arbó, K. L. Ishikawa, K. Schiessl, E. Persson, and J. Burgdörfer.
             Intracycle and intercycle interferences in above-threshold ionization: The time grating.
             Phys. Rev. A, 81:021403, 2010.

[ALN+15]   D. G. Arbó, C. Lemell, S. Nagele, N. Camus, L. Fechner, A. Krupp, T. Pfeifer, S. D.
             López, R. Moshammer, and J. Burgdörfer.
             Ionization of argon by two-color laser pulses with coherent phase control.
             Phys. Rev. A, 92:023402, 2015.

[ANT+14]   Diego G. Arbó, Stefan Nagele, Xiao-Min Tong, Xinhua Xie, Markus Kitzler, and
             Joachim Burgdörfer.
             Interference of electron wave packets in atomic ionization by subcycle sculpted laser
             pulses.
             Phys. Rev. A, 89:043414, 2014.

[APJ+09]   M. J. Abel, T. Pfeifer, A. Jullien, P. M. Nagel, M. J. Bell, D. M. Neumark, and S. R.
             Leone.
             Carrier-envelope phase-dependent quantum interferences in multiphoton ionization.
             J. Phys. B, 42(7):075601, 2009.

[APPM01]   M. R. Armstrong, P. Plachta, E. A. Ponomarev, and R. J. D. Miller.
             Versatile 7-fs optical parametric pulse generation and compression by use of adaptive
             optics.
             Opt. Lett., 26(15):1152–1154, 2001.

[AS83]   D. H. Auston and P. R. Smith.
             Generation and detection of millimeter waves by picosecond photoconductivity.

Applied Physics Letters, 43(7):631–633, 1983.

[AS91]   S. W. Allendorf and A. Szöke.
              High-intensity multiphoton ionization of H_2.
              Phys. Rev. A, 44:518–534, 1991.

[Ban95]   A. D. Bandrauk.
              Molecules in Laser Fields.
              Springer, 1995.

[Bar67]   J.N. Bardsley.
              The ionization of molecules near threshold.
              Chem. Phys. Lett., 1(5):229 – 232, 1967.

[BBdRW$^+$12] C. Bourassin-Bouchet, S. de Rossi, J. Wang, E. Meltchakov, A. Giglia, N. Mahne,
              S. Nannarone, and F. Delmotte.
              Shaping of single-cycle sub-50-attosecond pulses with multilayer mirrors.
              N. J. Phys., 14(2):023040, 2012.

[BBS$^+$97]   T. Baumert, T. Brixner, V. Seyfried, M. Strehle, and G. Gerber.
              Femtosecond pulse shaping by an evolutionary algorithm with feedback.
              Applied Physics B, 65(6):779–782, 1997.

[Ber66]   R. S. Berry.
              Ionization of molecules at low energies.
              J. Chem. Phys., 45(4), 1966.

[BK00]   T. Brabec and F. Krausz.
              Intense few-cycle laser fields: Frontiers of nonlinear optics.
              Rev. Mod. Phys., 72:545–591, 2000.

[BKP$^+$04]   T. Brixner, G. Krampert, T. Pfeifer, R. Selle, G. Gerber, M. Wollenhaupt, O. Graefe,
              C. Horn, D. Liese, and T. Baumert.
              Quantum control by ultrafast polarization shaping.
              Phys. Rev. Lett., 92:208301, 2004.

[BM16]   M. Beyer and F. Merkt.
              Observation and calculation of the quasibound rovibrational levels of the electronic
              ground state of H_2^+.
              Phys. Rev. Lett., 116:093001, 2016.

[BMG$^+$12]   A. E. Boguslavskiy, J. Mikosch, A. Gijsbertsen, M. Spanner, S. Patchkovskii, N. Gador,
              M. J. J. Vrakking, and A. Stolow.
              The multielectron ionization dynamics underlying attosecond strong-field
              spectroscopies.
              Science, 335(6074):1336–1340, 2012.

[BO27]   M. Born and R. Oppenheimer.
              Zur quantentheorie der molekeln.
              Ann. Phys. Berlin, 84:0457–0484, 1927.

[Boy03]   R. W. Boyd.
              Nonlinear Optics.
              Second Edition. Academic Press, 2003.

[Bra08]   T. Brabec.
              Strong Field Laser Physics.
              Springer, 2008.

[BS86]   Paul Brumer and Moshe Shapiro.
              Control of unimolecular reactions using coherent light.
              Chem. Phys. Lett., 126(6):541 – 546, 1986.

[BSV09]   M. Bernier, Y. Sheng, and R. Vallée.
               Ultrabroadband fiber bragg gratings written with a highly chirped phase mask and
               infrared femtosecond pulses.
               Opt. Express, 17(5):3285–3290, 2009.

[BUU+03]   A. Baltuska, Th Udem, M. Uiberacker, M. Hentschel, E. Goulielmakis, Ch Gohle,
               R. Holzwarth, V. S. Yakovlev, A. Scrinzi, T. W. Hansch, and F. Krausz.
               Attosecond control of electronic processes by intense light fields.
               Nature, 421(6923):611–615, 2003.

[BWPW97]   A. Baltuška, Z. Wei, M. S. Pshenichnikov, and D. A. Wiersma.
               Optical pulse compression to 5 fs at a 1-MHz repetition rate.
               Opt. Lett., 22(2):102–104, 1997.

[BZMS90]   P. H. Bucksbaum, A. Zavriyev, H. G. Muller, and D. W. Schumacher.
               Softening of the H_2^+ molecular bond in intense laser fields.
               Phys. Rev. Lett., 64:1883–1886, 1990.

[Cam13]   N. Camus.
               *Non-sequential double ionization of atoms with phase-controlled ultra-short laser
               pulses*.
               PhD Thesis, Universität Heidelberg, 2013.

[CB69]   W. A. Chupka and J. Berkowitz.
               High resolution photoionization study of the H_2 molecule near threshold.
               J. Chem. Phys., 51(10), 1969.

[CBAC86]   S. Chu, J. E. Bjorkholm, A. Ashkin, and A. Cable.
               Experimental observation of optically trapped atoms.
               Phys. Rev. Lett., 57:314–317, 1986.

[CFK+12]   N. Camus, B. Fischer, M. Kremer, V. Sharma, A. Rudenko, B. Bergues, M. Kübel, N. G.
               Johnson, M. F. Kling, T. Pfeifer, J. Ullrich, and R. Moshammer.
               Attosecond correlated dynamics of two electrons passing through a transition state.
               Phys. Rev. Lett., 108:073003, 2012.

[CHB+85]   S. Chu, L. Hollberg, J. E. Bjorkholm, Alex Cable, and A. Ashkin.
               Three-dimensional viscous confinement and cooling of atoms by resonance radiation
               pressure.
               Phys. Rev. Lett., 55:48–51, 1985.

[Chu81]   S. Chu.
               Floquet theory and complex quasivibrational energy formalism for intense field
               molecular photodissociation.
               J. Chem. Phys., 75(5):2215–2221, 1981.

[Con26]   E. Condon.
               A theory of intensity distribution in band systems.
               Phys. Rev., 28:1182–1201, 1926.

[Cor93]   P. B. Corkum.
               Plasma perspective on strong field multiphoton ionization.
               Phys. Rev. Lett., 71:1994–1997, 1993.

[CYE90]   C. Chen, Y. Yin, and D. S. Elliott.
               Interference between optical transitions.
               Phys. Rev. Lett., 64:507–510, 1990.

[DCT+13]   J. Dura, N. Camus, A. Thai, A. Britz, M. Hemmer, M. Baudisch, A. Senftleben, C. D.
               Schröter, J. Ullrich, R. Moshammer, and J. Biegert.
               Ionization with low-frequency fields in the tunneling regime.
               Sci. Rep., 3:2675, 2013.

[dJFZ+04]   V. L. B. de Jesus, B. Feuerstein, K. Zrost, D. Fischer, A. Rudenko, F. Afaneh, C. D. Schröter, R. Moshammer, and J. Ullrich.
Atomic structure dependence of nonsequential double ionization of He, Ne and Ar in strong laser pulses.
J. Phys. B, 37(8):L161, 2004.

[DK98]   N. B. Delone and V. P. Krainov.
Tunneling and barrier-suppression ionization of atoms and ions in a laser radiation field.
Phys. Usp., 41(5):469–485, 1998.

[DMJ+00]   R. Dörner, V. Mergel, O. Jagutzki, L. Spielberger, J. Ullrich, R. Moshammer, and H. Schmidt-Böcking.
Cold target recoil ion momentum spectroscopy: a 'momentum microscope' to view atomic collision dynamics.
Phys. Rep., 330(2-3):95 – 192, 2000.

[DR06]   J. C. Diels and W. Rudolph.
Ultrashort Laser Pulse Phenomena.
Second Edition. Academic Press, 2006.

[DRK65]   V. H. Dibeler, R. M. Reese, and M. Krauss.
Mass-spectrometric study of photoionization. ii. H_2, HD, and D_2.
J. Chem. Phys., 42(6), 1965.

[DSR+16]   E. Diesen, U. Saalmann, M. Richter, M. Kunitski, R. Dörner, and J. M. Rost.
Dynamical characteristics of rydberg electrons released by a weak electric field.
Phys. Rev. Lett., 116:143006, 2016.

[DT63]   E. K. Damon and R. G. Tomlinson.
Observation of ionization of gases by a ruby laser.
Appl. Opt., 2(5):546–547, 1963.

[DYO+05]   P. Dombi, V. S. Yakovlev, K. O'Keeffe, T. Fuji, M. Lezius, and G. Tempea.
Pulse compression with time-domain optimized chirped mirrors.
Opt. Express, 13(26):10888–10894, 2005.

[Ein17]   A. Einstein.
Zur quantentheorie der strahlung.
Physik. Z., 18:121–128, 1917.

[Fan70]   U. Fano.
Quantum defect theory of l uncoupling in H_2 as an example of channel-interaction treatment.
Phys. Rev. A, 2:353–365, 1970.

[FB91]   R. R. Freeman and P. H. Bucksbaum.
Investigations of above-threshold ionization using subpicosecond laser pulses.
J. Phys. B, 24(2):325, 1991.

[FBM+87]   R. R. Freeman, P. H. Bucksbaum, H. Milchberg, S. Darack, D. Schumacher, and M. E. Geusic.
Above-threshold ionization with subpicosecond laser pulses.
Phys. Rev. Lett., 59:1092–1095, 1987.

[FCBS87]   R. L. Fork, C. H. Brito Cruz, P. C. Becker, and C. V. Shank.
Compression of optical pulses to six femtoseconds by using cubic phase compensation.
Opt. Lett., 12(7):483–485, 1987.

[FCK+15]   L. Fechner, N. Camus, A. Krupp, J. Ullrich, T. Pfeifer, and R. Moshammer.
Creation and survival of autoionizing states in strong laser fields.
Phys. Rev. A, 92:051403, 2015.

[Fec14]   L. Fechner.

High resolution experiments on strong-field ionization of atoms and molecules: test of tunneling theory, the role of doubly excited states, and channel-selective electron spectra.
PhD Thesis, Universität Heidelberg, 2014.

[Fis10]   B. Fischer.
Time resolved studies of H_2^+ dissociation with phase-stabilized laser pulses.
PhD Thesis, Universität Heidelberg, 2010.

[FKP+10]   B. Fischer, M. Kremer, T. Pfeifer, B. Feuerstein, V. Sharma, U. Thumm, C. D. Schröter, R. Moshammer, and J. Ullrich.
Steering the electron in H_2^+ by nuclear wave packet dynamics.
Phys. Rev. Lett., 105:223001, 2010.

[Flo83]   G. Floquet.
Sur les équations différentielles linéaires á coefficients périodiques.
Ann. Ec. Norm., 12:47–48, 1883.

[FM72]   J. Field and A. McConchie.
A time domain method for producing pulse compression in a plasma.
IEEE Trans. Antennas and Prop., 20(5):675–676, 1972.

[FPAC82]   F. Fabre, G. Petite, P. Agostini, and M. Clement.
Multiphoton above-threshold ionisation of xenon at 0.53 and 1.06 μm.
J. Phys. B, 15(9):1353, 1982.

[FPP+99]   L. J. Frasinski, J. H. Posthumus, J. Plumridge, K. Codling, P. F. Taday, and A. J. Langley.
Manipulation of bond hardening in H_2^+ by chirping of intense femtosecond laser pulses.
Phys. Rev. Lett., 83:3625–3628, 1999.

[FSC+13]   A. Fischer, A. Sperl, P. Cörlin, M. Schönwald, H. Rietz, A. Palacios, A. González-Castrillo, F. Martín, T. Pfeifer, J. Ullrich, A. Senftleben, and R. Moshammer.
Electron localization involving doubly excited states in broadband extreme ultraviolet ionization of H_2.
Phys. Rev. Lett., 110:213002, 2013.

[FWG+09]   U. Fruhling, M. Wieland, M. Gensch, T. Gebert, B. Schutte, M. Krikunova, R. Kalms, F. Budzyn, O. Grimm, J. Rossbach, E. Plonjes, and M. Drescher.
Single-shot terahertz-field-driven x-ray streak camera.
Nat. Photon., 3(9):523–528, 2009.

[GHS+14]   X. Gong, P. He, Q. Song, Q. Ji, H. Pan, J. Ding, F. He, H. Zeng, and J. Wu.
Two-dimensional directional proton emission in dissociative ionization of H_2.
Phys. Rev. Lett., 113:203001, 2014.

[GLW+10]   E. Goulielmakis, Z. Loh, A. Wirth, R. Santra, N. Rohringer, V. S. Yakovlev, S. Zherebtsov, T. Pfeifer, A. M. Azzeer, M. F. Kling, S. R. Leone, and F. Krausz.
Real-time observation of valence electron motion.
Nature, 466(7307):739–743, 2010.

[GMJS+11]   M. Glass-Maujean, C. Jungen, H. Schmoranzer, I. Haar, A. Knie, P. Reiss, and A. Ehresmann.
The transition probabilities from the ground state to the excited J = 0 $^1\Sigma_u^+$ levels of H_2: Measurements and ab initio quantum defect study.
J. Chem. Phys., 135(14), 2011.

[GSHAM90]   A. Giusti-Suzor, X. He, O. Atabek, and F. H. Mies.
Above-threshold dissociation of H_2^+ in intense laser fields.
Phys. Rev. Lett., 64:515–518, 1990.

[GSM+00]   L. Gallmann, D.H. Sutter, N. Matuschek, G. Steinmeyer, and U. Keller.
           Techniques for the characterization of sub-10-fs optical pulses: a comparison.
           Appl. Phys. B, 70(1):S67–S75, 2000.

[GVT+11]   R. Gumenyuk, I. Vartiainen, H. Tuovinen, S. Kivistö, Y. Chamorovskiy, and O. G.
           Okhotnikov.
           Dispersion compensation technologies for femtosecond fiber system.
           Appl. Opt., 50(6):797–801, 2011.

[HAKK02]   J. Hebling, G. Almási, I. Z. Kozma, and J. Kuhl.
           Velocity matching by pulse front tilting for large-area thz-pulse generation.
           Opt. Express, 10(21):1161–1166, 2002.

[HDBT11]   H. Hirori, A. Doi, F. Blanchard, and K. Tanaka.
           Single-cycle terahertz pulses with amplitudes exceeding 1 MV/cm generated by optical
           rectification in $LiNbO_3$.
           Appl. Phys. Lett., 98(9):091106, 2011.

[HF11]   M. C. Hoffmann and J. A. Fülöp.
           Intense ultrashort terahertz pulses: generation and applications.
           J. Phys. D, 44(8):83001, 2011.

[HGH+13]   S. Huang, E. Granados, W. R. Huang, K. Hong, L. E. Zapata, and F. X. Kärtner.
           High conversion efficiency, high energy terahertz pulses by optical rectification in
           cryogenically cooled lithium niobate.
           Opt. Lett., 38(5):796–798, 2013.

[HIY+09]   K. Hosaka, R. Itakura, K. Yokoyama, K. Yamanouchi, and A. Yokoyama.
           Photoelectron-photoion coincidence momentum imaging for dissociative ionization of
           ethanol in intense laser fields.
           Chem. Phys. Lett., 475(1-3):19 – 23, 2009.

[HJ72]   G. Herzberg and C. Jungen.
           Rydberg series and ionization potential of the H_2 molecule.
           J. Mol. Spectrosc., 41(3):425 – 486, 1972.

[HS15]   I. V. Hertel and C. Schulz.
           Atoms, Molecules and Optical Physics 2.
           Springer, 2015.

[HSS03]   M. Hacker, G. Stobrawa, and R. Sauerbrey.
           Femtosecond-pulse sequence compression by gires–tournois interferometers.
           Opt. Lett., 28(3):209–211, 2003.

[IQY+02]   J. Itatani, F. Quéré, G. L. Yudin, M. Yu. Ivanov, F. Krausz, and P. B. Corkum.
           Attosecond streak camera.
           Phys. Rev. Lett., 88:173903, 2002.

[IW98]   C. Iaconis and I. A. Walmsley.
           Spectral phase interferometry for direct electric-field reconstruction of ultrashort optical
           pulses.
           Opt. Lett., 23(10):792–794, 1998.

[JKP12]   C. J. Joachain, N. J. Kylstra, and R. M. Potvliege.
           Atoms in Intense Laser Fields.
           Cambridge University Press, 2012.

[JP10]   C. Jungen and S. T. Pratt.
           Low-energy dissociative recombination in small polyatomic molecules.
           J. Chem. Phys., 133(21), 2010.

[Kel65]   L. V. Keldysh.
           Ionization in the field of a strong electromagnetic wave.
           Sov. Phys. JETP, 20(5):1307–1314, 1965.

[KFF$^+$09]   M. Kremer, B. Fischer, B. Feuerstein, V. L. B. de Jesus, V. Sharma, C. Hofrichter,
                A. Rudenko, U. Thumm, C. D. Schröter, R. Moshammer, and J. Ullrich.
                Electron localization in molecular fragmentation of H_2 by carrier-envelope phase
                stabilized laser pulses.
                Phys. Rev. Lett., 103:213003, 2009.

[KI09]   F. Krausz and M. Ivanov.
                Attosecond physics.
                Rev. Mod. Phys., 81:163–234, 2009.

[Kim03]   M. F. Kimmitt.
                Restrahlen to t-rays – 100 years of terahertz radiation.
                J. Biol. Phys., 29(2):77–85, 2003.

[KSK93]   K. C. Kulander, K. J. Schafer, and J. L. Krause.
                Dynamics of Short-Pulse Excitation, Ionization and Harmonic Conversion.
                Plenum Press, New York, 1993.

[KSV$^+$06]   M. F. Kling, C. Siedschlag, A. J. Verhoef, J. I. Khan, M. Schultze, T. Uphues, Y. Ni,
                M. Uiberacker, M. Drescher, F. Krausz, and M. J. J. Vrakking.
                Control of electron localization in molecular dissociation.
                Science, 312(5771):246–248, 2006.

[KT93]   D. J. Kane and R. Trebino.
                Single-shot measurement of the intensity and phase of an arbitrary ultrashort pulse by
                using frequency-resolved optical gating.
                Opt. Lett., 18(10):823–825, 1993.

[KTB$^+$02]   R. Kohler, A. Tredicucci, F. Beltram, H. E. Beere, E. H. Linfield, A. G. Davies, D. A.
                Ritchie, R. C. Iotti, and F. Rossi.
                Terahertz semiconductor-heterostructure laser.
                Nature, 417(6885):156–159, 2002.

[Lau77]   A. M. F. Lau.
                Radiative-dressed molecules.
                Phys. Rev. A, 16:1535–1542, 1977.

[LEL$^+$16]   S. Larimian, S. Erattupuzha, C. Lemell, S. Yoshida, S. Nagele, R. Maurer, A. Baltuška,
                J. Burgdörfer, M. Kitzler, and X. Xie.
                Coincidence spectroscopy of high-lying rydberg states produced in strong laser fields.
                Phys. Rev. A, 94:033401, 2016.

[LL77]   L. D. Landau and E. M. Lifshitz.
                Quantum Mechanics, Non-relativistic Theory.
                Pergamon Press, 1977.

[LLWY11]   W. Liu, M. Li, C. Wang, and J. Yao.
                Real-time interrogation of a linearly chirped fiber bragg grating sensor based on chirped
                pulse compression with improved resolution and signal-to-noise ratio.
                J. Lightwave Technol., 29(9):1239–1247, 2011.

[Mai60]   T. H. Maiman.
                Stimulated optical radiation in ruby.
                Nature, 187(4736):493–494, 1960.

[MAS$^+$12]   J. McKenna, F. Anis, A. M. Sayler, B. Gaire, N. G. Johnson, E. Parke, K. D. Carnes,
                B. D. Esry, and I. Ben-Itzhak.
                Controlling strong-field fragmentation of H_2^+ by temporal effects with few-cycle laser
                pulses.
                Phys. Rev. A, 85:023405, 2012.

[MCF$^+$17]   Y. Mi, N. Camus, L. Fechner, M. Laux, R. Moshammer, and T. Pfeifer.

Electron-nuclear coupling through autoionizing states after strong-field excitation of H_2 molecules.
Phys. Rev. Lett., 118:183201, 2017.

[Mey14] K. Meyer.
Coherent and statistical phase control and measurements of time-dependent quantum dynamics.
PhD Thesis, Universität Heidelberg, 2014.

[MFH+07] F. Martín, J. Fernández, T. Havermeier, L. Foucar, Th. Weber, K. Kreidi, M. Schöffler, L. Schmidt, T. Jahnke, O. Jagutzki, A. Czasch, E. P. Benis, T. Osipov, A. L. Landers, A. Belkacem, M. H. Prior, H. Schmidt-Böcking, C. L. Cocke, and R. Dörner.
Single photon-induced symmetry breaking of H_2 dissociation.
Science, 315(5812):629–633, 2007.

[Mil88] D. R. Miller.
Free Jet Sources, Atomic and Molecular Beam Methods (Ed. by Giacinto Scoles).
Oxford University Press, 1988.

[MKMP13] Y. Mi, A. Kaldun, K. Meyer, and T. Pfeifer.
Time-domain pulse compression by interfering time-delay operations.
Phys. Rev. A, 88:053824, 2013.

[MOR+12] K. Meyer, C. Ott, P. Raith, A. Kaldun, Y. Jiang, A. Senftleben, M. Kurka, R. Moshammer, J. Ullrich, and T. Pfeifer.
Noisy optical pulses enhance the temporal resolution of pump-probe spectroscopy.
Phys. Rev. Lett., 108:098302, 2012.

[MUU+94] R. Moshammer, J. Ullrich, M. Unverzagt, W. Schmidt, P. Jardin, R. E. Olson, R. Mann, R. Dörner, V. Mergel, U. Buck, and H. Schmidt-Böcking.
Low-energy electrons and their dynamical correlation with recoil ions for single ionization of helium by fast, heavy-ion impact.
Phys. Rev. Lett., 73:3371–3374, 1994.

[OKA+14] C. Ott, A. Kaldun, L. Argenti, P. Raith, K. Meyer, M. Laux, Y. Zhang, A. Blattermann, S. Hagstotz, T. Ding, R. Heck, J. Madronero, F. Martin, and T. Pfeifer.
Reconstruction and control of a time-dependent two-electron wave packet.
Nature, 516(7531):374–378, 2014.
Letter.

[OMB+12] K. Osvay, M. Mero, Á. Börzsönyi, A. P. Kovács, and M. P. Kalashnikov.
Spectral phase shift and residual angular dispersion of an acousto-optic programmable dispersive filter.
Appl. Phys. B, 107(1):125–130, 2012.

[OYJ+13] T. I. Oh, Y. S. You, N. Jhajj, E. W. Rosenthal, H. M. Milchberg, and K. Y. Kim.
Intense terahertz generation in two-color laser filamentation: energy scaling with terawatt laser systems.
N. J. Phys., 15(7):075002, 2013.

[PAF+09] V. Pervak, I. Ahmad, J. Fulop, M. K. Trubetskov, and A. V. Tikhonravov.
Comparison of dispersive mirrors based on the time-domain and conventional approaches, for sub-5-fs pulses.
Opt. Express, 17(4):2207–2217, 2009.

[PAM88] G. Petite, P. Agostini, and H. G. Muller.
Intensity dependence of non-perturbative above-threshold ionisation spectra: experimental study.
J. Phys. B, 21(24):4097, 1988.

[Pav04] D. Pavicic.
Coulomb Explosion and Intense-Field Photodissociation of Ion-Beam H_2^+ and D_2^+.
PhD thesis, 2004.

[PBNW94]   G. G. Paulus, W. Becker, W. Nicklich, and H. Walther.
            Rescattering effects in above-threshold ionization: a classical model.
            J. Phys. B, 27(21):L703, 1994.

[Pfe04]   T. Pfeifer.
            Adaptive control of coherent soft x-rays.
            PhD Thesis, Universität Würzburg, 2004.

[Pfl12]   T. Pflüger.
            Electron impact ionization studies of small rare gas clusters.
            PhD Thesis, Universität Heidelberg, 2012.

[PGW+01]   G. G. Paulus, F. Grasbon, H. Walther, P. Villoresi, M. Nisoli, S. Stagira, E. Priori, and
            S. De Silvestri.
            Absolute-phase phenomena in photoionization with few-cycle laser pulses.
            Nature, 414(6860):182–184, 2001.

[PJD+10]   T. Pfeifer, Y. Jiang, S. Düsterer, R. Moshammer, and J. Ullrich.
            Partial-coherence method to model experimental free-electron laser pulse statistics.
            Opt. Lett., 35(20):3441–3443, 2010.

[PKK97]   M. Protopapas, C. H. Keitel, and P. L. Knight.
            Atomic physics with super-high intensity lasers.
            Rep. Prog. Phys., 60(4):389, 1997.

[PNX+94]   G. G. Paulus, W. Nicklich, H. Xu, P. Lambropoulos, and H. Walther.
            Plateau in above threshold ionization spectra.
            Phys. Rev. Lett., 72:2851–2854, 1994.

[Pop04]   V. S. Popov.
            Tunnel and multiphoton ionization of atoms and ions in a strong laser field (keldysh
            theory).
            Phys. Usp., 47(9):855, 2004.

[Pos04]   J. H. Posthumus.
            The dynamics of small molecules in intense laser fields.
            Rep. Prog. Phys., 67(5):623, 2004.

[PPT+98]   J. H. Posthumus, J. Plumridge, M. K. Thomas, K. Codling, L. J. Frasinski, A. J.
            Langley, and P. F. Taday.
            Dynamic and geometric laser-induced alignment of molecules in intense laser fields.
            J. Phys. B, 31(13):L553, 1998.

[RHD+09]   D. Ray, F. He, S. De, W. Cao, H. Mashiko, P. Ranitovic, K. P. Singh, I. Znakovskaya,
            U. Thumm, G. G. Paulus, M. F. Kling, I. V. Litvinyuk, and C. L. Cocke.
            Ion-energy dependence of asymmetric dissociation of D_2 by a two-color laser field.
            Phys. Rev. Lett., 103:223201, 2009.

[RKS+16]   M. Richter, M. Kunitski, M. Schöffler, T. Jahnke, L. P. H. Schmidt, and R. Dörner.
            Ionization in orthogonal two-color laser fields: Origin and phase dependences of
            trajectory-resolved coulomb effects.
            Phys. Rev. A, 94:033416, 2016.

[Rul05]   C. Rullière, editor.
            Femtosecond Laser Pulses.
            Second Edition. Springer, 2005.

[RZS+04]   A. Rudenko, K. Zrost, C. D. Schröter, V. L. B. de Jesus, B. Feuerstein, R. Moshammer,
            and J. Ullrich.
            Resonant structures in the low-energy electron continuum for single ionization of atoms
            in the tunnelling regime.
            J. Phys. B, 37(24):L407, 2004.

[Sen09]   A. Senftleben.
            Kinematically complete study on electron impact ionisation of aligned hydrogen molecules.
            PhD Thesis, Universität Heidelberg, 2009.

[Ser13]   C. Serrat.
            Broadband spectral-phase control in high-order harmonic generation.
            Phys. Rev. A, 87:013825, 2013.

[Shi65]   J. H. Shirley.
            Solution of the schrödinger equation with a hamiltonian periodic in time.
            Phys. Rev., 138:B979–B987, 1965.

[SHS$^+$03] E. Seres, R. Herzog, J. Seres, D. Kaplan, and C. Spielmann.
            Generation of intense 8 fs laser pulses.
            Opt. Express, 11(3):240–247, 2003.

[SJM14]   D. Sprecher, C. Jungen, and F. Merkt.
            Determination of the binding energies of the np rydberg states of H_2, HD, and D_2 from high-resolution spectroscopic data by multichannel quantum-defect theory.
            J. Chem. Phys., 140(10), 2014.

[SKPT$^+$10] G. Sansone, F. Kelkensberg, J. F. Perez-Torres, F. Morales, M. F. Kling, W. Siu, O. Ghafur, P. Johnsson, M. Swoboda, E. Benedetti, F. Ferrari, F. Lepine, J. L. Sanz-Vicario, S. Zherebtsov, I. Znakovskaya, A. L'Huillier, M. Yu Ivanov, M. Nisoli, F. Martin, and M. J. J. Vrakking.
            Electron localization following attosecond molecular photoionization.
            Nature, 465(7299):763–766, 2010.

[SM85]   D. Strickland and G. Mourou.
            Compression of amplified chirped optical pulses.
            Opt. Commun., 56(3):219–221, 1985.

[ST58]   A. L. Schawlow and C. H. Townes.
            Infrared and optical masers.
            Phys. Rev., 112:1940–1949, 1958.

[ST07]   B. E. A. Saleh and M. C. Teich.
            Fundamentals of Photonics.
            Second Edition. Wiley, 2007.

[Tak70]   S. Takezawa.
            Absorption spectrum of H_2 in the vacuum-uv region. ii. Rydberg series converging to the first six vibrational levels of the H_2^+ ground state.
            J. Chem. Phys., 52(11), 1970.

[TK93]   R. Trebino and D. J. Kane.
            Using phase retrieval to measure the intensity and phase of ultrashort pulses: frequency-resolved optical gating.
            J. Opt. Soc. Am. A, 10(5):1101–1111, 1993.

[TZL02]   X. M. Tong, Z. X. Zhao, and C. D. Lin.
            Theory of molecular tunneling ionization.
            Phys. Rev. A, 66:033402, 2002.

[UFSC$^+$04] X. Urbain, B. Fabre, E. M. Staicu-Casagrande, N. de Ruette, V. M. Andrianarijaona, J. Jureta, J. H. Posthumus, A. Saenz, E. Baldit, and C. Cornaggia.
            Intense-laser-field ionization of molecular hydrogen in the tunneling regime and its effect on the vibrational excitation of H_2^+.
            Phys. Rev. Lett., 92:163004, 2004.

[UMD$^+$03] J. Ullrich, R. Moshammer, A. Dorn, R. Dörner, L. P. H. Schmidt, and H. Schmidt-Böcking.

Recoil-ion and electron momentum spectroscopy: reaction-microscopes.
Rep. Prog. Phys., 66(9):1463, 2003.

[VDT$^+$14] S. Vidal, J. Degert, M. Tondusson, E. Freysz, and J. Oberlé.
Optimized terahertz generation via optical rectification in znte crystals.
J. Opt. Soc. Am. B, 31(1):149–153, 2014.

[VJO$^+$15] C. Vicario, M. Jazbinsek, A. V. Ovchinnikov, O. V. Chefonov, S. I. Ashitkov, M. B. Agranat, and C. P. Hauri.
High efficiency thz generation in dstms, dast and oh1 pumped by cr:forsterite laser.
Opt. Express, 23(4):4573–4580, 2015.

[VLC$^+$00] F. Verluise, V. Laude, Z. Cheng, Ch. Spielmann, and P. Tournois.
Amplitude and phase control of ultrashort pulses by use of an acousto-optic programmable dispersive filter: pulse compression and shaping.
Opt. Lett., 25(8):575–577, 2000.

[WLB$^+$14] B. Wolter, C. Lemell, M. Baudisch, M. G. Pullen, X. M. Tong, M. Hemmer, A. Senftleben, C. D. Schröter, J. Ullrich, R. Moshammer, J. Biegert, and J. Burgdörfer.
Formation of very-low-energy states crossing the ionization threshold of argon atoms in strong mid-infrared fields.
Phys. Rev. A, 90:063424, 2014.

[XDDR$^+$12] X. Xie, K. Doblhoff-Dier, S. Roither, M. S. Schöffler, D. Kartashov, H. Xu, T. Rathje, G. G. Paulus, A. Baltuška, S. Gräfe, and M. Kitzler.
Attosecond-recollision-controlled selective fragmentation of polyatomic molecules.
Phys. Rev. Lett., 109:243001, 2012.

[XRK$^+$12] X. Xie, S. Roither, D. Kartashov, E. Persson, D. G. Arbó, L. Zhang, S. Gräfe, M. S. Schöffler, J. Burgdörfer, A. Baltuška, and M. Kitzler.
Attosecond probe of valence-electron wave packets by subcycle sculpted laser fields.
Phys. Rev. Lett., 108:193004, 2012.

[YC92] G. Yao and S. Chu.
Laser-induced molecular stabilization and trapping and chemical bond hardening in intense laser fields.
Chem. Phys. Lett., 197(4):413 – 418, 1992.

[YMS97] D. Yelin, D. Meshulach, and Y. Silberberg.
Adaptive femtosecond pulse compression.
Opt. Lett., 22(23):1793–1795, 1997.

[YZO$^+$03] K. Yamane, Z. Zhang, K. Oka, R. Morita, M. Yamashita, and A. Suguro.
Optical pulse compression to 3.4fs in the monocycle region by feedback phase compensation.
Opt. Lett., 28(22):2258–2260, 2003.

[Zar98] R. N. Zare.
Laser control of chemical reactions.
Science, 279(5358):1875–1879, 1998.

[ZBMS90] A. Zavriyev, P. H. Bucksbaum, H. G. Muller, and D. W. Schumacher.
Ionization and dissociation of H_2 in intense laser fields at 1.064 μm, 532 nm, and 355 nm.
Phys. Rev. A, 42:5500–5513, 1990.

[Zew88] A. H. Zewail.
Laser femtochemistry.
Science, 242(4886):1645–1653, 1988.

[Zew00] A. H. Zewail.
Femtochemistry: Atomic-scale dynamics of the chemical bond.
J. Phys. Chem. A, 104(24):5660–5694, 2000.

[ZLL$^+$16]   W. Zhang, Z. Li, P. Lu, X. Gong, Q. Song, Q. Ji, K. Lin, J. Ma, F.g He, H. Zeng, and J. Wu.
Photon energy deposition in strong-field single ionization of multielectron molecules.
Phys. Rev. Lett., 117:103002, 2016.

[ZX10]   X. C. Zhang and J. Xu.
Introduction to THz Wave Photonics.
Springer, 2010.

Acknowledgements